INVESTIGATIONS ON Z-PINCH DEVICES FOR PULSED RADIOGRAPHY AND MATERIAL CHARACTERIZATION

By

SANJAY CHANDRA ANDOLA

PHYS01201404014

Bhabha Atomic Research Centre,
Mumbai -400085,
India

A thesis submitted to the
Board of Studies in Physical Sciences

In partial fulfillment of requirements
for the Degree of

DOCTOR OF PHILOSOPHY
of
HOMI BHABHA NATIONAL INSTITUTE

July 2021

Homi Bhabha National Institute

Recommendation of the Viva Voce Committee

As members of the viva voce committee, we certify that we have read the dissertation prepared by Shri Sanjay Chandra Andola entitled **"Investigations on Z-pinch plasma devices for pulsed radiography and material characterization"** and recommend that it may be accepted as fulfilled the thesis requirement for the award of Degree of Doctor of Philosophy.

Sr No	Composition	Name	Signature with date
1.	**Chairman**	Prof. S. Krishnagopal	12/7/21
2.	**Convener** (Guide)	Prof. K. D. Joshi	12/7/21
3.	**External Examiner**	Prof. D. S. Patil	DSPatil
4.	**Member**	Prof. J. A. Chakera	12/7/21
5.	**Member**	Prof. S. Ghorui	12/7/21
6.	**Member**	Prof. A. Roy	12/7/21

Final approval and acceptance of this thesis is contingent upon the candidate's submission of final copies of the thesis to HBNI.

I hereby certify that I have read this thesis prepared under my direction and recommend that it may be accepted as fulfilling the thesis requirement.

Date 12-7-21
Place: Mumbai

Dr. K.D. Joshi
(Guide)

STATEMENT BY AUTHOR

This dissertation has been submitted in partial fulfillment of requirements for an advanced degree at Homi Bhabha National Institute (HBNI) and is deposited in the library to be made available to borrowers under rules of the HBNI.

Brief quotations from this dissertation are allowable without special permission, provided that accurate acknowledgement of source is made. Requests for permission for extended quotation from or reproduction of this manuscript in whole or in part may be granted by the Competent Authority of HBNI when in his or her judgment the proposed use of the material is in the interests of scholarship. In all other instances, however, permission must be obtained from the author.

Andola

Sanjay Chandra Andola

DECLARATION

I, hereby declare that the investigation presented in the thesis has been carried out by me. The work is original and has not been submitted earlier as a whole or in part for a degree / diploma at this or any other Institution / University.

Andola
Sanjay Chandra Andola

List of publications arising from the thesis

Journals

1. **S.C. Andola**, J. Batra, A.C. Jaiswar, A.K. Saxena and T.C. Kaushik, “Investigations on slow current driven X-pinch as soft x-ray source for radiographic applications”, High Energy Density Physics, 2020, 35: p. 100732.

2. **S.C. Andola**, A.M. Rawool, and T.C. Kaushik, “Detector sensitivity and calibration for yield measurements in fusion neutron sources”, Nuclear Instruments and Methods in Physics Research Section A: Accelerators, Spectrometers, Detectors and Associated Equipment, 2019, 944: p. 162580.

3. **S.C. Andola**, R. Niranjan, R. Srivastava, D. Vidyasagar, A. P. Singh, Y.V.S. Lakshmi, A. M. Rawool, I. K. Singh, T. C. Kaushik and K. D. Joshi, “Active Single-Shot Interrogation of Natural Uranium in Industrial Radioactive Waste using Plasma Focus Device”, Nuclear Instruments and Methods in Physics Research Section A, Accelerators, Spectrometers, Detectors and Associated Equipment,2021,1004: p. 165362.

4. **S.C. Andola**, A.C. Jaiswar, T.C. Kaushik and K.D. Joshi “Study of Microsecond X-pinches of Refractory and Non-Refractory Metals” High Energy Density Physics, **in review.**

Conferences

1. **S.C. Andola**, R. Niranjan, R. Srivastava, A. M. Rawool, I. K. Singh, D. S. Setty, S. Sairam, A. Singh, D. Vidya Sagar, K. D. Joshi and T. C. Kaushik, “Feasibility study of active Non-destructive assay of Natural Uranium in Nuclear waste." 15th Int. Conf. on Modern Trends of Activation Analysis, (MTAA-19), Trombay, Nov 17-22 (2019**)** **(Best Poster Award).**

2. **S.C. Andola,** J. Batra, A.C Jaiswar and T.C Kaushik, “Development of X-pinch system with slow rising current source", proc. of 33rd Nat. Symp. on Plasma Sci. and Tech. (PLASMA-2018), Delhi, India, p. 82, December 2018.

3. **S.C. Andola**, A. Kumar, R. Niranjan, R. Shrivastav, A. M. Rawool. D. B. Paranjape, N. Rawat, R. K. Rout, M. K. Saxena, B. S. Tomar and T. C. Kaushik, “Non-Destructive Assay of Fissile Material in Lab Waste using Plasma Focus Device”, Int. Conf. on

Characterization & Quality Control of Nucl. Fuel. (CQCNF-2018), Hyderabad, p.135, December 2018.

4. R. Niranjan, R. Srivastava, **S.C. Andola,** R.K. Rout and T.C. Kaushik, "Development and Characterization of a 25 kJ plasma focus device for various applications", proc. of 33rd Nat. Symp. on Plasma Sci. & Tech. (PLASMA-2018), Delhi, p. 35, December 2018, [2018]
5. **S.C. Andola**, R. Niranjan, R. Srivastava, R.K. Rout and T.C. Kaushik, “Study of x-ray Imaging Parameters of Plasma Focus Device using Image Plates”, 30th Nat. Symp. on Plasma Sci. & Tech., Kolkata, India, 1-4 Dec. 2015, IP-242, 154, [2015]
6. T.C. Kaushik, R.K. Rout, **S.C. Andola**, R. Niranjan and S.C. Gupta., “Indigenous pulsed x-ray and neutron sources for non-destructive material characterization”, 25th National Seminar & International Exhibition on Non-destructive Evaluation, Hyderabad, India, Nov. 26-18, 2015, 235-I, 162., [2015]
7. R. Niranjan, R.K. Rout, R. Srivastava, **S.C. Andola**, T.C. Kaushik and S.C. Gupta., “Development and application of various portable plasma focus devices as pulsed fusion plasma source”. 22nd IAEA Technical Meeting (TM) on Research Using Small Fusion Devices, Prague, Czech Republic; Oct 12-14, 2015, [2015]

Sanjay Chandra Andola

DEDICATED TO MY PARENTS

ACKNOWLEDGEMENTS

During this thesis, I have got the support of many individuals that kept me heading in the right direction. It is a pleasure to convey my sincere gratitude to all of them.

First, I would like to express my gratitude and respect to my adviser Dr. K. D. Joshi for the inspiration, invaluable guidance, and constant encouragement. His wide knowledge and a keen interest in contemporary and critical scientific problems have enabled me to dig through this work.

I owe sincere gratitude to Dr. T.C. Kaushik, for introducing me to the pulsed plasma, neutron physics, and activation studies and guiding me through the initial segment of this thesis.

I also like to thank Dr. A. K. Saxena for the continuous guidance throughout this work in addition to the suggestion and encouragement provided on the personal and professional level.

Many thank also go out to the doctoral committee members, Dr. S. Krishnagopal, Dr. J. A. Chakera, Dr. S. Ghorui, and Dr. A. Roy for their scientific comments and valuable suggestions. Thanks, are also due to former committee members Dr. R. K. Rout, Dr. N. K. Gupta and Dr. A. Sinha for providing their valuable suggestions in the work specially in HED physics and radiography.

I enjoyed working with many collaborators namely Mr. A. Kumar, Mr. D. B. Paranjape, Mr. M. K. Saxena, and Dr. D. Vidyasagar; involved in various projects. I benefited greatly from the conversations with Dr. B. S. Tomar for his extensive insights into the activation studies.

Many thanks go out to my colleagues Dr. Amit Rav, Dr. Ram Niranjan, Mrs. J. Batra, and Mr. R. Srivastava for the valuable suggestion and discussions during various stages of the work.

I am indebted to the support provided by Mr. A. M. Rawool, Mr. A. C. Jaiswar, Mr. I. K. Singh, Mr. P. Mahajan, Mr. D. G Chaudhary, R. G. Warang, and Mrs. S. Singnurkar, without their

technical help, it was next to impossible to carry out the experimental work. I would also like to pay my tribute to our beloved colleague Mr. A. V. Patil, whom we have lost due to covid-19.

Lastly, I take this chance to thank my mother and siblings for their continuous support and encouragement throughout the life. Words are insufficient to share my gratitude to my wife, Renu, for the rock-solid support and the relentless motivation in rain and shine.

Sanjay Andola

CONTENTS

CHAPTER 3:EXPERIMENTAL SYSTEMS AND MEASUREMENT METHODOLOGIES 47

SUMMARY

This thesis presents the development and characterization of two schemes of Z-pinches for applications pertaining to radiography and material analysis. In the first scheme, an X-pinch is developed on a slow current driver having rate of rise of a current (dI/dt) of ~0.1kA/ns with a peak current of 110 kA. An experimental study has been carried out to investigate the current required to pinch the plasma in ‘X’ configuration for linear mass density ranging from 22 μg/cm to 134 μg/cm. It was found out that the required pinch current increases linearly with an increase in the linear mass density of the X-pinch. A similar relationship has been found between the pinch current and the dI/dt. A comprehensive analysis of X-pinches made of two groups of metal wires i.e. refractory (W and Mo) and non-refractory (Cu and Al) has been performed for dI/dt ranging from 0.04 kA/ns to 0.1kA/ns. The analysis included the study of the x-ray parameters such as the yield, source size, timing, and jitter with their dependence on load properties (wire material and diameter). In most of the cases, the x-rays are in the soft energy regime i.e. <5keV, whereas, in few cases such as 2× 15 μm Cu with polyamide coating and 2× 13 μm W, a small yield of x-rays in hard regime i.e. >6keV has also been observed. The smallest source size is observed to be<13 μm. A few μm thick polyamides coating on Cu wire is observed to enhance the yield and energy of x-rays significantly. Further, using the X-pinch-based x-ray, the point projection radiography of polyamide coated Cu wires of diameter 43μm and 60μm, exploded at the current rate of 10kA -20kA per 1μshas been performed. The radiographs suggest that at a higher current rate of ~0.02kA/ns, the wire core expands uniformly. However, at lower current rates the expansion becomes non-uniform throughout the length. In the case of the thicker wire at a slower current rate, the explosion starts at a few discreet points leading to the formation of unduloid which could be due to the deposited energy being too low to explode the whole wire.

In the second Z-pinch scheme, plasma focus (PF) devices have been characterized for use in the study of the internal structure of materials by radiography and neutron activation techniques. The neutrons from PF devices need to be thermalized as the interaction cross-section of neutrons with materials is high for the thermal range. For this purpose, the Monte Carlo simulations have been performed to optimize the thickness of the moderators. The optimum thickness required for moderating the DD neutron is estimated to be 80 mm and 100 mm, respectively, for polyethylene and perspex. For the applications related to radiography, the energy of x-rays, the x-ray and neutron content, source size, and the spatial resolution of the image have been estimated. In the radiographic image, the contribution of thermal neutrons is determined to be 4.2±2% with significant contribution from x-rays of low energy. Further, it has been seen that the x-ray intensity decreases with increasing energy. In the x-ray spectrum of the PF device, the contribution of high energy (>100 keV) x-rays is observed to be very small (<2%). The source size of the x-rays is <1 mm and the spatial resolution from the radiograph is estimated to be 147±10μm. Using the PF device, the x-ray and neutron radiographs of the different samples such as BNC's, moving fans, hydride blisters in zircalloy samples, and the tungsten turbojet blade was obtained.

The PF devices have been used first time for the assay of natural uranium in industrial radioactive waste. Employing the D-D operated PF device with neutron yield ~ 2.1×10^8 per shot, the detection limit of the active interrogation system is estimated to be 170g of natural uranium in ~40 kg of waste. Further simulations suggest that these limits will go down further to 3.3g of natural uranium when the same PF device with the D-T mixture is used. A detection limit of 40 mg of ^{235}U in the 5 liters in compressible laboratory waste contaminated with enriched uranium has been achieved.

LIST OF FIGURES

LIST OF TABLES

CHAPTER 1

INTRODUCTION

The Z-pinch devices have been widely used for the generation of high-energy-density plasma to study the matter in extreme conditions. The high-density plasma under such extreme conditions produces intense radiations ranging from infrared to hard x-rays, electron, and ion beams, etc. Upon using suitable material such as deuterated fibres, these devices can also produce a high yield of neutrons. The Z-pinches are the most efficient and powerful sources of laboratory radiation today. Though a lot of efforts have been devoted towards Z-pinch research since the decade of 1950, still various observed phenomena in the pinches are not understood fully, thereby leaving scope for further research. The present thesis aims to investigate some configurations of Z-pinches towards applications in radiography and characterization of materials. The present chapter of the thesis provides a basic introduction to different kinds of pinch plasma devices and configurations existing worldwide and various research activities in the field of Z-pinches already been published in the literature. This is followed by the aim and scope of the present thesis. Finally, in the end, the chapter-wise layout of the thesis is presented.

1.1 Z-pinch and principle of plasma generation

The Z-pinch [1] is a scheme to confine a plasma column by the radial magnetic force of high current driven in axial (z) direction generated by pulsed power systems. The analytical study of the plasma pinches began in 1934 by W. H. Bennett[2] that reports the well-known criteria of thermal and magnetic pressure equilibrium[3] for self-focusing beam of charged particles. The current required to attain this equilibrium for Z-pinch plasmas is described in section 2.1 of Chapter 2.

The exploding wires are one of the earliest configurations of the Z-pinches that have been studied as a source of soft x-rays radiations[4, 5]. When a fast current of a few kA in a microsecond and sub-microsecond time scale is applied to a thin wire, the wire vaporizes due to fast energy deposition and produces a low resistance plasma column, which in turn compressed to its axis by Lorentz (J×B) force. Here J defines the current density flowing through the plasma channel and B is the self-generated magnetic field. This rapid compression leads to heating (10-100 eV) of plasma and results in the emission of black body radiation.

In the decade of 1950, the extreme temperature generated in the exploding wire plasma had attracted the attention of scientists towards its application in controlled thermonuclear fusion[6, 7]. The discharge in deuterium gas[8] in a high current of microsecond time duration was experimentally investigated to achieve the fusion conditions of temperature and densities with reasonable confinement time as suggested by different analytical models[9, 10]. However, disruption of the plasma column by fast magneto-hydrodynamic instabilities made it difficult to achieve the condition suitable for fusion which led to discouragement in the fusion scientist community towards research work on the generation of thermonuclear fusion using microsecond scale Z-pinches. Subsequently, various studies conducted during the 1970s, reported that these instabilities can be mitigated using fast (ns scale) current drivers [11-13], thereby giving a ray of hope and renewed the interest of the scientific community in Z-pinches. These drivers could deliver megavolt pulses and mega ampere currents in few hundreds of ns. The high initial impedance (~1-2 Ω) of the single wire has limited its application for such studies due to inefficient coupling of driver energy to the load. The more effective way to achieve a higher density plasma and to generate high-intensity x-rays by converting the kinetic energy (KE) of the imploding plasma column is by the use of low impedance loads (0.1-0.25Ω) such as wire arrays[14], foil liner[15], gas puff[16], or low-density cylindrical foam[17]. Using these nanosecond drivers, greater stability and better uniformity in the pinch plasmas have been achieved in various Z-pinch configurations. To date, ~2 MJ of x-ray radiation with electron temperature as high as few keV have been achieved using Z-pinches[14, 18] with a wall-plug efficiency of 15%.

1.2 Various Z-pinch configurations

To investigate suitable drivers for fusion and other applications, various Z-pinch configurations have evolved and been studied. Based on physics involved in working, these are classified[19] as dynamic Z-pinches (wire array and gas puff) and equilibrium pinches (exploding wires, fiber pinch, gas embedded Z-pinches, and capillary discharge). The other form of grouping can be based on the load composition (gas, wire, or fiber-based). A brief introduction of some of the configurations starting from the simplest to the more complex form is provided below:

1.2.1 Capillary discharge

The simplest configuration of the Z-pinches is the capillary discharge, in which a high voltage is applied across a gas column enclosed in a dielectric capillary of 1-3 cm long and a few mm diameters (Fig.1.1a). A surface discharge across the wall produces nearly local thermodynamic equilibrium plasma. The capillary discharge Z pinch has shown its utility as an efficient driver for x-ray lasers[20]. In comparison to its equivalent laser pumped scheme, the capillary discharge has the advantage of large gain volume, long duration, and high efficiency. Ne-like Argon (46.9 nm) soft x-ray laser has been demonstrated in 1994 using a capillary Z-pinch scheme in which, the plasma column has been compressed by the application of a fast current of 39kA that resulted in the generation of the soft x-ray laser pulse of 0.8 ns[21].

1.2.2 Gas embedded Z-pinch

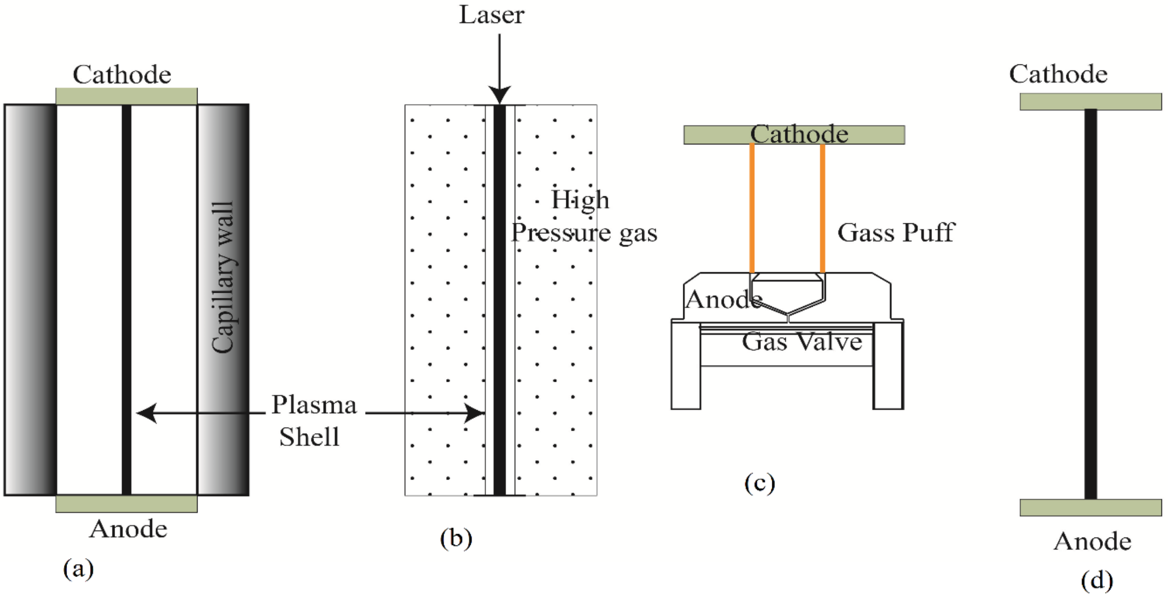

Fig. 1.1 Different Z-pinch configurations (a) Capillary Discharge (b) Gas embedded Z-pinch (c) Gas puff(d) Exploding wire plasma.

To study the stability of the plasma of capillary discharges, the gas-embedded Z-pinches[22] were introduced (Fig. 1.1b). These are produced when an external gas pressure (near atmospheric) is applied in addition to magnetic pressure to a filamentary discharge. The plasma is created along the length by application of focused laser pulse followed by the current across the plasma column. The high current causes the plasma to expand radially due to the acceleration of surrounding neutral gas that cools the plasma column which results in the development of the kink instabilities (m=1) in the column. Although the rapid growth of instability in this configuration has limited its use for fusion, it can be used for the study of pinch dynamics and stability.

1.2.3 Gas puffs

To replicate the vacuum spark gaps for pinch loads and explore the possibilities of generating high-temperature pinch plasma at a relatively lower current, gas puff Z-pinches[23] were introduced. The gas puffing is done through an aperture drilled in one of the electrodes using a fast valve and nozzle in-between the electrodes. The schematic is shown in Fig. 1.1c. Upon application of fast current, the gas breakdown leads to the creation of the plasma. Further, the interaction of the current and its self-magnetic field leads to pinching which in turn results in a hot dense state that emits the x-rays up to very high energy. The device can also be used as a source of high neutrons[24] when operated with deuterium gas. It has an advantage over the wire-based loads (wire array) as due to its initial axisymmetric density distribution comparatively symmetric plasma is generated. The device can be operated for multiple shots without breaking the vacuum which engenders it for a higher number of shots per day.

1.2.4 Exploding wires

Exploding wires (Fig.1.1d) have long been studied for exploring the possibility of employing these as a compact device for light and x-rays sources apart from their use as a basic element in the wire array Z-pinches. A fast current pulse driven through a thin metal wire can produce high-density Z-pinch plasma[25]. These wires can be made of non-metallic (carbon, polyethylene, deuterated polyethylene, and cryogenic (frozen) deuterium) fibers or metals such as aluminum or tungsten. From the perspective to attain the fusion conditions, the stability of the plasma column generated by the explosion of deuterated polyethylene has been observed up to ~100 ns with high neutron yield in a current generator of few hundreds of kA[26-29]. Due to impedance mismatch to the high current drivers, these configurations were replaced with an array of thin wires.

1.2.5 Wire array

The disadvantages related to (i) exploding wires[4] to high initial impedance, (ii) gas puff[23] due to difficulty in measuring the initial density distribution and (iii) thin metal liner[30] due to difficulty in fabrication have been overcome by employing the array of thin metallic wires as shown in schematic Fig.1.2a. For example in the Sandia Z machine[31], an array of a large number (up to 300) of thin wires of aluminum and tungsten have been used as a load to produce nearly 2 MJ of x-ray energy [14, 32]. Further, the wire array Z-pinch studies carried out in the Z machine also report that the decrease in the inter-wire gap (<1.5 mm) resulted in a substantial improvement in peak x-ray power and reduction in the x-ray pulse width. At a large inter-wire gap, the increasing current recompresses the wires independently resulting in the implosion of a series of unstable wires. This axial non-uniformity can alternatively be mitigated by using a thin shell liner, however, to keep the optimized mass per unit length similar to wire arrays, a very thin shell thickness is required, which is difficult to fabricate. The wire array Z-pinches are very vulnerable to the Rayleigh Taylor (RT) instabilities, which can be partially mitigated using double or nested arrays[32].

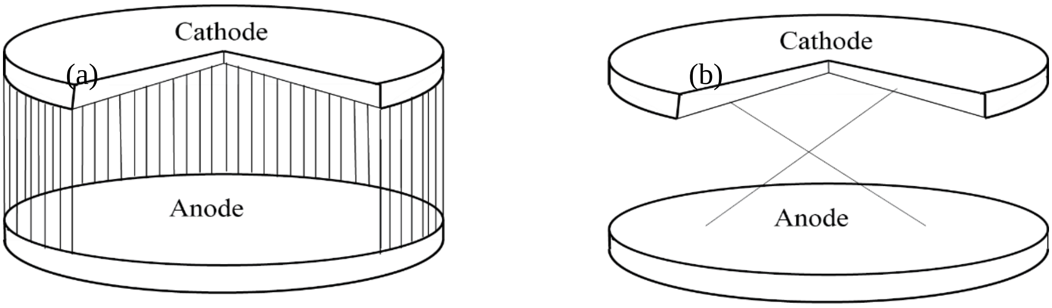

Fig. 1.2 Schematic of (a) Wire array and (b) X-pinch.

1.2.6 X-pinch

X-pinches [33] are also a variant of Z-pinch, in which two or more wires are mounted in between the electrodes in ‘X’ configurations as shown in Fig. 1.2b. The individual wire caries half (or 1/n) of the total current supplied by the driver and merges at the cross point. It provides better impedance matching than a single wire. The center point leads to a localized high-density hot plasma region and emits the x-ray. The evolution of X-pinch consists of a sequence of processes, including heating of wire, partial evaporation of wire surfaces and formation of plasma, the outflow of plasma (jet structure) at the crossing point due to the axial shear, and formation of a small ‘Z’ column at the center. This 'Z' column, then compresses due to J×B force, which leads to the formation of high-temperature plasma (hot spots) and emits soft x-rays. After x-ray emission, the neck of the plasma column breaks and forms a mini-diode and generates the electron and ion beams. These beams upon interaction with the created electrodes of the mini diode emit higher energy (hard) x-rays.

Due to the localized x-ray source, it can be utilized as a point source for radiography[34, 35] of the plasma. The X-pinches emit very strong radiation ranging from VUV to high-energy x-rays of different spot sizes depending on the emitting area and the processes involved. X-rays of energy (E)< 1keV are emitted from the wire core near the center region of 1 mm whereas hotspots (HS) are the regions emitting x-rays of 1kev < E< 10 keV from the thermal plasma of keV temperature. The higher energy (up to 50 keV) x-ray emission is observed from the anode side. In addition to x-rays, X-pinches generate neutrons (~10^8 n/shot) when used with deuterated polyethylene fibres[36, 37]. Although no comprehensive analysis was conducted on neutron emission processes in X-pinches, the cause of the neutron emission is believed to be due to ion beam interaction.

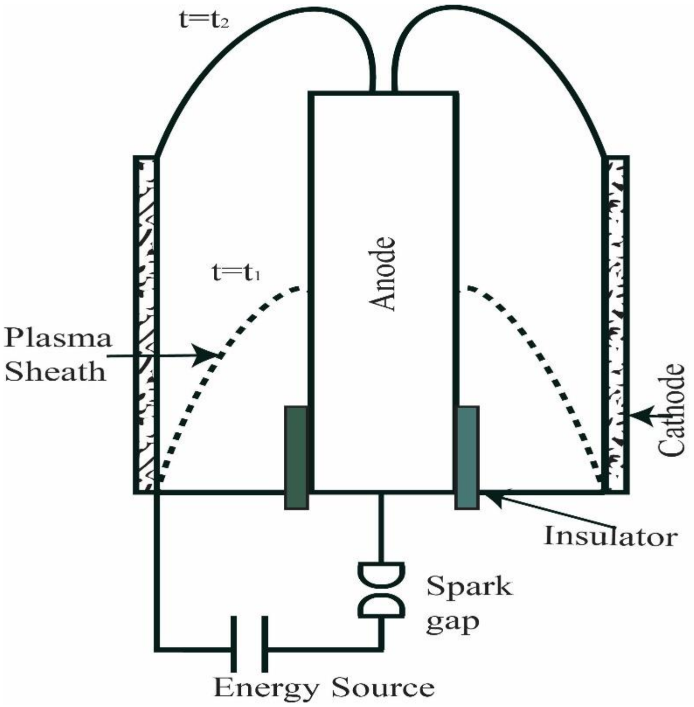

Fig. 1.3 Schematic of a Mather type dense plasma focus.

1.2.7 Dense plasma focus

The plasma focus (PF) device[38] is a variant of the equilibrium Z-pinch. The device consists of two concentric electrodes separated by an insulator, which are placed in a chamber filled with an operating gas. Two geometries, Mather [38] and Fillppov types[39] of the PF have been proposed. The aspect ratio (length divided by diameter) of the electrode is > 1 typically ranging from 5-10 in the former scheme and < 1 in the latter scheme (typically 0.2). A schematic of the Mather type device is shown in Fig. 1.3. Here on the application of pulsed power, the breakdown near the surface of the insulator forms a plasma sheath, which travels towards the end of the electrode due to Lorentz force and collapses (focuses) at the top of the anode. The disruption of plasma focus at the top forms the electron and ion beams that emit intense x-rays upon interaction with neutrals. When deuterium is used as a filling gas, fusion neutrons are generated. For the efficient pinching of the plasma, the pinch should occur at the maximum driver current, which can be achieved by suitably designing the dimensions of the electrodes. The duration of radiation pulses is of the order of ns. The temperature and the density of the plasma achieved at the pinch are of the order of 200eV-1keV and ~10^{24} m^{-3} respectively[40].

1.3 Applications of Z-pinches

The Z-pinches are an intense source of pulsed radiation that can be utilized in numerous physics applications. These applications can be grouped into four major categories namely (i) radiation source (ii) inertial confinement fusion (iii) study of material properties under extreme conditions and (iv) generation of a high magnetic field. The Z-pinch research was mainly influenced by the idea of sustained laboratory fusion. In comparison to magnetic confinement fusion (MCF) [41], there is no magnetic coil involved to limit the magnetic field in the Z-pinches. The densities and temperature in the Z pinches are almost 10^7 times higher than the tokamaks[42] that limits the confinement time (of a few ns). As the confinement time is less than ion transit times along the length, the Z-pinch plasma becomes less prone to impurities unless it interacts with the walls. The vulnerability of Z-pinches towards sausage (m=0) and kink instabilities (m=1) and energy loss to the electrodes[1, 43] are the main limiting parameters. To reduce the energy loss at the electrode and harnessing reasonable power from Z-pinch-based systems, the power station should operate in pulsed mode[44].

Furthermore, research work towards the contemporary applications of the Z-pinches is described as follows:

1.3.1 Z-pinch as a radiation source

Traditionally the Z-pinches have been used for the generation of intense radiation in the energy range from microwave to x-rays[43]. The high temperature generated in the Z-pinches leads to excitation of L or K shells of the plasma and emits high energy characteristic x-ray in addition to the soft x-ray continuum.

In addition to wires and wire arrays, plasma focus[38, 40] and gas puffs have also been used as sources of a wide range of radiations [45]. To utilize these devices for radiation applications high x-ray yield is desirable. Various approaches, such as argon injection into an anode through a small hole in a PF [46] and two-stage heating such as shock heating accompanied by thermal conduction using Ar plasma compression[47] have been employed to enhance the x-ray yield.

The X-pinches have been mostly utilized as a localized x-ray source of energy ranges 1-10 keV. The source size of ~1 µm and pulse width of a few ns makes it an ideal device to be used as a backlighting source to diagnose various other pulse plasma applications. Several current generators[48] with a rate of rise of current from 0.2 kA/ns -100kA/ns have been used worldwide for X-pinch research for point projection radiography. For ease of access, conical X-pinches[49, 50] (hybrid X-pinch) consisting of a wire of a few mm length with the equivalent mass of X-pinch have also been explored for similar purposes.

1.3.1.1 Black body radiation

The fast Z-pinches of high z materials have been utilized as the source of thermal radiation from few tens to hundreds of eV to drive a fusion capsule. Wire arrays and cylindrical liners in different configurations have been utilized for this purpose. The radiation temperature has been achieved in the range of 120-140eV using a wire array Z-pinch at Z-facility of Sandia lab[51, 52]. The details of the black body radiation from Z-pinches used for inertial confinement fusion are provided later in this chapter (section 1.3.4.)

1.3.1.2 Neutron source

The Z-pinch devices such as plasma focus, gas puff, and the wire array are used as a source of pulsed neutrons when operated with deuterium, deuterium-tritium gas, or deuterated fiber. Due to its simplistic design and easy to use (being a gas-based system), plasma focus and gas puffs are widely used devices amongst them. The anisotropy in the neutron emission suggests the fusion is mostly caused by ion beam-plasma collision rather than thermonuclear[53]. In PF device using DT gas, a neutron yield of 10^{12} n/shot with FWHM of ~60ns has been obtained with 2 MA of the current[54]. In this experiment, the neutron emission is found to be dominated by beam-target fusion of super-thermal ions, and the contribution of thermonuclear fusion is estimated to be ~1%.

The X-pinches of deuterated fibers used in the S-300 current generator are reported to emit neutrons of 10^{10} n/pulse[37]. The anisotropy and the temperature of the hotspot observed in the experiments suggest that the neutrons are emitted as a result of the fusion of deuterium ion beams while colliding with the electrode.

1.3.2 High magnetic field generation

The self-high magnetic field of a Z-pinch device has been utilized as a magnetic lens to deflect the ion beam in the accelerator[55]. At CERN large number of shots have been performed to prove the capability of a Z-pinch of 29 cm long ionized gas of 4 cm in diameter on a current of 400kA. It generated a peak magnetic field of 4T[55]. The purpose of these experiments is to utilize the azimuthal magnetic field of Z-pinch discharge to focus (plasma lens) high-energy antiprotons at CERN. To date, these active plasma lenses have been used to focus the beams of electrons[56], protons, antiprotons, muons, kaons[57], and other heavy ions[58].

1.3.3 Study of material properties under extreme conditions

The rapid release of energy into material leads to the generation of shock waves. The radiation from the Z-pinches can instantaneously heat the material and generating the shock waves of pressure ~1Mbar. Due to the large area of irradiation and comparatively high radiation output, Z-pinches have been used to study the hydrodynamics of samples of a large area. The electrically exploding wires (EEW) in different media have been conventionally used for the generation of shock waves. Simulations have suggested that a spherical wire array of 20 mm diameter made of 0.12 mm wire can produce a shock pressure of 6TPa for a current of 300 kA with a rise time of 1.1 μs [59]. In addition to these, possibilities have been explored for the use of EEW for ignition of a target in ICF[60], driving phase transitions in the warm dense matter[61], and enhancing the recovery of oil in oil wells. The amplitude of the shock wave in exploding wires depends upon the vaporized mass. So the shock waves have poor reproducibility due to partial vaporization of the exploding wire however, it has been observed that even a very low (6%) vaporization rate is sufficient to generate a strong shock.

To study the behavior of the material in the radiation environment that would be existing in the laser-driven schemes of the National Ignition Facility (NIF), Z-pinches have been utilized[60]. These pinches have been studies for the magnitude, spectrum, and duration of the shock in the ablator of the fusion capsule irradiated with the radiation of the hohlraum. Branitskii et al., 1996 have studied shock propagation and the equation of state of metals at 3 Mbar of pressure[62]. The experiments have provided the data for testing of radiation hydrodynamic codes for radiation flow, equation of state, opacity, and shock velocity over the whole range of radiations related to fusion.

1.3.4 The controlled thermonuclear Fusion

The Z-pinch could be a promising driver for the compact fusion device due to its simple geometry, compactness, and absence of external magnetic coils. In a driver for efficient fusion, the released radiation or thermal energy should be higher than the electrical energy supplied for magnetic compression (breakeven condition)[63]. Among all the laboratory fusion reactions, deuterium and tritium have the highest cross-section

$$ {}_{1}^{2}H + {}_{1}^{3}H \rightarrow {}_{2}^{4}He + {}_{0}^{1}n + 17.06\ MeV \qquad (1.1)$$

The fusion reactions in the plasma pinch are of two types; beam target fusion and thermonuclear fusion. In the former one, the fusion is achieved by collisions of the energetic ion beam to the neutral ions of the plasma, however, in the later, the fusion is achieved by heating the various species of the plasma (all the species are in thermodynamic equilibrium). These species in the heated plasma should achieve more than a critical density (n) for a confinement time (τ). This criterion was formulated by J D Lawson[63] and for the D-T fusion, it is given by:

$$n\tau > 10^{14}\ \mathrm{s/cm^3} \qquad (1.2)$$

The energy released in the fusion of D-T plasma in volume V is given by

$$E_{fusion} = \tau E_{D-T} \int n_D\, n_T < \sigma v >_{D-T} dV \qquad (1.3)$$

Here n_D and n_T are the number densities of the deuterium and tritium, $<\sigma v>_{DT}$ is the temperature dependant reaction rate for D-T fusion and E_{D-T} is the released energy in the fusion. There are two promising concepts for achieving laboratory fusion satisfying the Lawson criteria i.e. the first one is (MCF) in which comparatively low-density plasma is confined for a long time ($\tau \geq 0.1$s) and the second one is inertial confinement fusion (ICF), high-density plasma is confined for the short time duration (ns).

Lindl et. al.[64] have derived the requirement to reach ignition in laser-driven ICF schemes to harness high yield. They proposed that the integrated flux of radiation at the surface of the capsule must be symmetrical within 1-2 percent, the x-ray energy absorbed must be >1MJ, as well as the radiation temperature must be as high as 225eV. The high (>15%) conversion efficiency for stored electrical energy to x-rays allows the Z-pinches to be used as a driver for ICF. There are two approaches for delivering the energy into the capsule, the first one is based on the adiabatic heating of the DT capsule or central hot-spot ignition, which is called the direct drive, and the second is based on imploding the DT capsule using black body radiation emitted by a hohlraum cavity.

In the direct-drive scheme, the ICF is achieved using magnetic pressure as a result of the implosion of cylindrical liners driven by a fast current. The radial convergence of the scheme is further improved to achieve higher fusion yield by preheating (100-500 eV) and magnetizing (>10T) the fuels[65].

In the indirect drive approach, the fusion capsule is irradiated indirectly by the black body radiation or the pressure pulse from the wire array or cylindrical shell liner of high-density high z material[66]. A schematic of a dynamic hohlraum is given in Fig.1.4. This approach is more inclined towards the symmetry of the implosion rather than the overall efficiency as this is a two-step process, i.e., conversion of KE of Z-pinch to radiation and then radiation to KE of the capsule. The wall-plug efficiency of the Z-pinches is ~15 % and out of the total energy absorbed by the capsule less than 10% gets converted into kinetic energy of the implosion, indicating that only a small fraction of x-ray energy is converted into kinetic energy of the imploding fuel[14, 32].

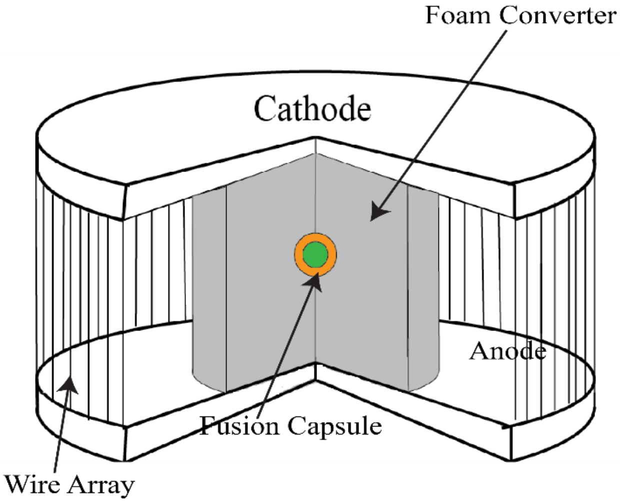

Fig. 1.4 Schematic of dynamic Hohlraum.

1.4 Current status of Z-pinch research

Historically, Z-pinch devices were developed to provide a promising driver for inertial confinement fusion using powerful pulse power drivers such as Cobra [67], Z machine[68], Shiva Star[69], etc. Wire array Z-pinches [32] and cylindrical liner have been used to produce high x-ray yield with high power. In the SHIVA Star facility Degnan et. al.[69] have produced 240kJ of soft x-rays in 130 ns FWHM using an aluminized plastic cylindrical liner. Zakharov et. al.[70] experimented on Angara-5 generator and accelerated a gaseous liner onto its inner shell and obtained an x-ray power of 9 TW with FWHM of 90ns.

Furthermore, several attempts have been made to study the fusion conditions in low-energy pulse power systems employing gas puffs, plasma focus devices, and exploding wires, etc. In the recent work of Klir et. al[53], a gas puff has been studied in 3 MA of current for estimation of ion energies and reported the neutron yield of 2×10^{12} n/shot. They have used a neutron-producing sample (deuterated polyethylene) placed onto the axis to enhance the neutron yield. The neutron production efficiency in this experiment is found to be ~10^{8}neutrons per joule of the stored Z-pinch energy. Low energy (100mJ) PF device[71] has been recently developed to explore the fusion at improbable conditions according to scaling laws.

Furthermore, apart from the study of high-temperature high-density fusion grade plasma, the use of z pinches has also been investigated for other non-conventional applications such as a study of material through pulsed radiography and particle-induced material characterization. Further, the X-pinches, due to small spot size are the ideal devices for the point projection radiography-based characterization of the fast-evolving plasma such as from exploding wires.

The X-pinch plasma has been studied extensively for its spectroscopic and radiographic applications in pulse power generators producing current pulse ranging from 50kA to 6 MA[48, 72]. The rate of rise of current (dI/dt) of the drivers used in these X-pinch experiments is ranging from 0.25 kA/ns to 100 kA/ns. Based on available experimental pieces of evidence till 2006 it has been empirically postulated[73] that dI/dt of more than 1 kA/ns is required for X-pinch to produce a narrow, bright and low time-jitter x-ray source.

The drivers that provide dI/dt greater than 1kA/ns are mainly the Marx banks discharged through water-filled pulse forming lines and thus relatively bulky and expensive. As an alternative to overcome size constraints and cost, attempts have been made to generate X-pinch plasma with relatively low dI/dt (<1kA/ns) using capacitor banks[74-76] and other techniques[77].

Among the slow systems reported in the literature, Christou et. al.[76] have studied the X-pinch dynamics using aluminum (Al), constantan, tungsten (W), and molybdenum (Mo) wires in capacitive discharge with 320 kA peak current and 1.2 μs rise time. Appartaim et al.[74] have demonstrated cross point dynamics of X-pinch on a capacitor bank with a peak current of 300 kA and 1 μs rise time. Recently, A 120 kA-500 ns current source[78] has been used to study the plasma dynamics in copper (Cu), Al, and W wire X-pinch, where the authors have obtained an x-ray source of size 70 μm with energies above 7 keV. The plasma dynamics study reported so far using the lowest rate of current rise (0.06kA/ns, 25kA) in two and four-wire tungsten X-pinch plasma configurations at different stages is by G. Collins et. al.[79] where the authors reported the generation of soft x-rays of energy in the 1-2keV range. Nevertheless, characterization of x-ray source in an X-pinch for radiographic purposes is reported at ~0.24 kA/ns or higher[74]. The X-pinch systems operated with slow currents (< 1 kA/ns) result in lowering of hard x-ray contribution, shot to shot variation in yield, and large jitter in x-ray pulse as compared to relatively faster systems, which leaves scope to develop and characterize the X-pinches at the still lower current rate.

Moreover, other Z-pinches such as PF devices and gas puffs have been used for radiography and particle-induced material characterization due to ease of operation. According to a recent report, a gas puff[80] has been utilized as an x-ray source for radiography of live tissues. Due to the high flux of high-energy x-rays, the PF device has been extensively investigated for applications in industrial radiography [81]. Apart from this, the high neutron flux of PF device has been utilized for the study of half-lives of elements[82], substance detection, and assay of nuclear material[83, 84]. The production of isotopes useful in nuclear medicine[85] has also been proposed using ion irradiation from the PF device.

Determination of content of nuclear material is an important issue for safe disposal of waste generated in facilities of the front end as well as the back end of the fuel cycle[86]. The non-destructive assay techniques used for the assay of fissile material are cost-effective, less time-consuming, and ensure less exposure to the operators. In the fuel fabrication facilities where uranium is handled, the presence of uranium in small quantities with low spontaneous emission[87] makes active assay techniques [88] advantageous over passive ones. Although the gamma-ray spectroscopy is useful for both identification and quantification, however in a large waste sample it becomes time-consuming and prone to erroneous results due to self-attenuation[89] and high gamma background. In the case of large waste samples containing a higher quantity of fissile material with low spontaneous neutron emission (specifically uranium contamination) and where well coincidence counters[90] or gamma spectroscopy cannot be used, the active assay techniques have an advantage over passive ones. Nonetheless depending upon the physical structure (dimension, density, and matrix) of the samples, the active and passive assays can be considered complementary to each other. The active assay techniques include active coincidence counters (ACC)[91], delayed emission-based techniques[83, 92] and differential die away (DDA) [93] among others. The ACC counts coincident prompt neutrons and the DDA technique utilizes the slowing down portion (epithermal) of prompt neutrons from induced fission. The detection of prompt emission poses a technical challenge and is somewhat not much required for uranium-containing samples due to the low background (self-emission being relatively smaller); however, detection of delayed emission from the fissile material is practical and more accurate for such applications. Several attempts have been made worldwide for the detection of a fissile component using detection of delayed emissions (neutrons or gammas) to characterize uranium in small samples[83, 84, 94], fuel pellets[94] and radioactive waste [92, 95].

To our knowledge, the application of PF device for the characterization of nuclear material in the large sample matrices has not been explored, the same has been addressed in the present research and constitutes a part of the thesis.

1.5 Motivation and scope of the thesis

As described above, the short-lived (tens of ns) Z-pinch plasma implosions provide many possibilities to study the physics involved in a variety of applications.

From the perspective of Z-pinch (wire array) as a driver for fusion, the uniform initiation is extremely crucial for the efficient conversion of electrical energy to magnetic and then to radiation. To understand the complex physics involved in the implosions, an understanding of single wire explosions and their subsequent merger is necessary. These two configurations are similar in initial phases; however, at later stages global magnetic field generated by the flow of current in the created plasma column of wire array plays a considerable role. The spacing of the wires in Z-pinches is so adjusted that at later stages of the current pulse the global magnetic field should dominate over the field of individual wires to avoid the compression in the individual wire.

Various studies have been performed since the decades starting from 1950, to understand the processes of wire explosion in the current of 1 kA to several hundreds of kA[4, 96]. Being a basic element of wire array, the single wire carries a fraction of the current of the driver, which can be studied at a smaller laboratory scale. The diagnostics include the estimation of energy deposition by current and voltage measurement, spatial profile measurement using imaging techniques, and plasma parameters by spectrometric measurement. To study the density profile, shock in the material, and various other volumetric phenomena the pulsed x-ray radiography is one of the suitable techniques. For backlighting, the fast-evolving plasma of such high density; the probing x-rays should have energy in the softer region, a pulse width of the order of a few ns with a source size of few μm. X-pinch being a localized source of small size and pulse width can extend its utility for such applications.

The simplicity, compactness, and requirement of small current which can be achieved using small capacitive systems, are the important figure of the merits of X-pinch sources for applications related to backlighting. However, the complexity in the dynamics of the X-pinches is immense, and the analytical solutions of various parameters are practically non-existent to date. Although the dynamics of the X-pinches have been studied by 2D or 3D modeling [97, 98], the data on various experimental systems are needed that can elucidate the physical processes and help to validate the results obtained from numerical modeling. Therefore, a comprehensive study of various parameters of the X-pinches using compact and low-cost drivers is needed.

Ryutov *et al.*[1] have established that in a shell of plasma, the product of the initial mass density and square of the initial radius (r_0) is constant for a current driver of fixed current and rise time (τ). It suggests that the heavier mass density imploding shell should have smaller initial radii. Moreover, the KE of an ion (so is the electron temperature) scales as the $(r_0/\tau)^2$, hence for loads of higher mass, the electron temperature becomes insufficient to excite the K or the L transitions. In the lighter shells, the KE of ions is comparatively higher and results in a higher yield of hard x-rays. This radiation yield increases up to an optimal shell density then starts decreasing, which can be explained as the low-density plasma is optically thin and the radiation power per unit volume scales as the square of the density. Therefore, for low-density plasma, the expansion dominates and results in lowering electron temperature before the thermal energy of the ions converts into radiation. These two possible mechanisms determine the optimal mass density of the imploding plasma shell in Z-pinches. As the central neck of the X-pinch forms a small Z-pinch, thus, for the efficient radiation output from the X-pinch device, the mass density of the plasma needs to be optimized for a given current generator.

Furthermore, the timing, number of bursts, yield, and source size of an x-ray pulse are the important parameters in the synchronous (ns) application of X-pinch (XP) in point projection radiography of high energy density (HED) plasma. In fast current-driven X-pinches, the jitter in x-ray bursts is found to be comparatively smaller (few ns) than those operated on slow current drivers (20-100 ns). Similarly, a vast difference has been observed in other properties of the generated x-rays. A lot of work[72] has been reported on the characterization of X-pinch on fast current drivers having a peak current of 300kA to 5MA for the dependence of x-ray properties on the shape of the current pulse and wire material. In contrary to fast drivers, very few reports are available on the current and rise time dependence of x-ray yield and timing/ jitter from the slow current drivers based X-pinch.

In addition to the driver parameters, the material parameters also play an important role in the explosion characteristics of wires in X-pinches, which subsequently decide the x-ray properties. The three groups of metals as defined by Romanova *et al.*[99] show different behavior upon electrical explosions due to the differences in their thermo-physical properties and expansion velocities. The expansion velocity, resistivity, and the atomic number ‘Z’ of the wire material influence the emitted x-ray properties. Also, the current requirement for a pinch in ‘X’ configuration and its effect on x-rays is still not studied to date. Moreover, the effect of insulating coating on the energy deposition and plasma formation in exploding wires has been reported earlier but the effect of the coating on the x-ray characteristics of an X-pinch is still unexplored.

In view of the brief review provided earlier, the dense plasma focus (PF) can be considered as a unique device that can be used for non-conventional applications. The use of gas to produce plasma makes this device simple in operation. It can also be modified for repetitive operations in lower energy devices. The thermonuclear fusion conditions in hotspots and ion-beam collision (beam target) fusion can be easily accomplished even in microsecond timescale current-driven plasma focus devices. Being a pulsed source of neutrons and x-rays, the PF device can extend its utility for the study of thick objects utilizing radiography. There are limited reports that propose the utilization of pulsed radiation for the study of the material. A systematic study on the application of the device as a pulsed radiation source to study short-lived radioisotopes is much required. The material identification through neutron activation such as fissile material quantification can also be explored using the PF device.

Being a single-shot device, plasma focus has an advantage over other conventional sources in that it has zero source background after few milliseconds, which is useful for a lower minimum detection limit. Further, as activity of the source neutron lasts up to a few ms in the sample which makes this device useful for the detection of neutron-induced activity of comparably shorter half-life.

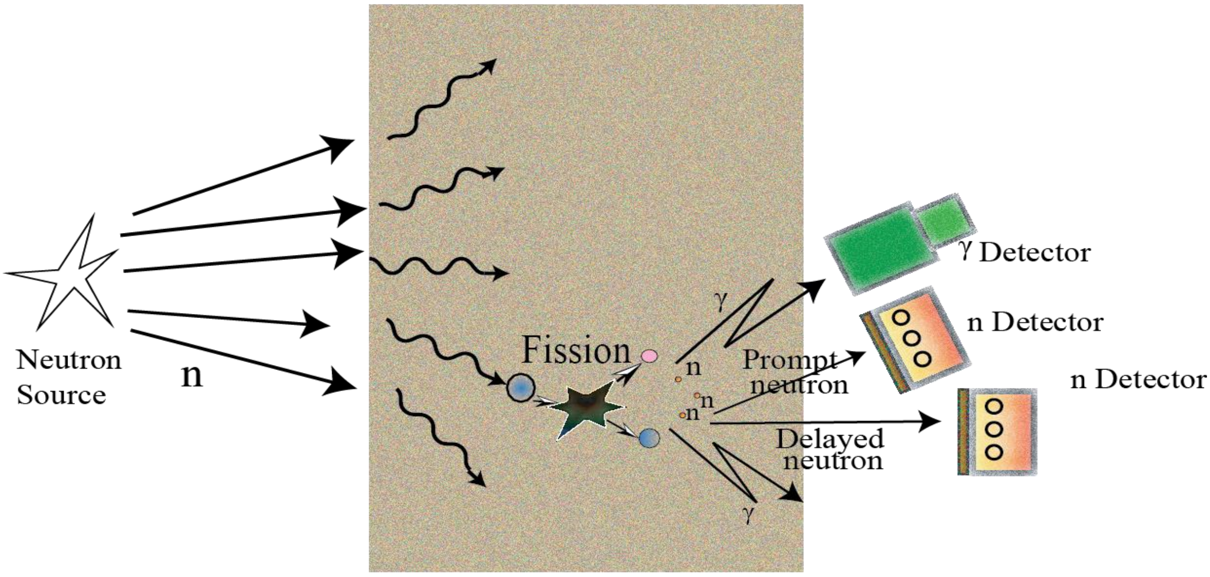

Fig. 1.5 The schematic of active neutron interrogation techniques.

Moreover, as reported in the literature (described in section 1.4) the fissile material quantity has been estimated from few milligrams in small samples to several kilograms in pellets and high mass samples in which the fissile component of uranium varies from 0.7% (natural) to < 20% (low enriched uranium). So far only a few reports[92] are available on the active assay of natural uranium in the nuclear waste generated in fuel fabrication facilities. In view of the limited study available on this aspect, we have performed the feasibility experiments for assay of uranium in waste generated in the fuel fabrication facility using a plasma focus device. Being a neutron-in neutron-out-based technique, this scheme provides higher penetration into the sample matrix; hence could be beneficial in the assay of large waste samples. The methodology of the technique[88] is based on irradiation of fissile material containing samples by neutrons and the detection of delayed neutrons from induced fission of ^{235}U. For a given enrichment and composition of the sample matrix, the induced fission neutron or gamma flux is proportional to the mass of fissile material present in the sample. The objective of the demonstration is to evaluate the deployment perspective of the system for active assay of natural uranium in the civil and metallic waste produced in the fuel fabrication or other such handling facilities. Different sample matrix could give a source of uncertainty due to self-shielding of interrogating neutrons and self-absorption of the delayed neutrons.

In the present thesis, we present experimental systems, techniques, results, and discussions to address the above-mentioned various unexplored/rarely reported issues pertaining to pulse plasma research and applications. The significant developments, as well as important research outcomes of the present work, are summarized below:

1. Development of a compact and portable X-pinch system of comparable x-ray parameters on a very slow and compact current driver for point projection radiography of the pulsed plasma. Despite the disadvantages of relatively larger spot size, this development provides new experimental results to study the dynamics of the pulsed plasma that can be compared with that of the fast X-pinches. The small-scale experiments can be easily modified

according to an application, which makes this device versatile. The important features of this device and studies performed are as follows:

(i) Developed a compact X-pinch system on the current driver of rise time < 0.1kA/ns.

(ii) Achieved the x-ray yield up to 0.57 J in two-wire X-pinches.

(iii) Investigated the current requirement for plasma to pinch for a driver having dI/dt from 0.04kA/ns to 0.12kA/ns for non-refractory (Cu and Al) and refractory (W and Mo) metals.

(iv) Studied the effect of material properties on x-ray parameters such as energy, number of spots, and their size and timing. It is observed that the energy of the x-ray is decided by the material of the load and the timing of the x-ray burst is governed by the wire diameter.

(v) Studied the effect of dielectric coating on soft x-ray yield.

(vi) Investigated the effect of material properties on electron temperature of the hotspot generated in X-pinches.

2. For the application of X-pinches to study the dynamics of exploding wire plasma, the resolution and timing are the crucial parameters, which strongly depend upon spot size and the jitter of the x-rays, respectively. To get the clear radiograph at different instances of the processes, various parameters need to be optimized. To pursue these objectives following efforts have been made:

(i) Radiography of exploding wires at post burst stages on the current rate of 0.01kA/ns-0.02kA/ns has been carried out.

(ii) Estimation of expansion velocity of wire core and study of unduloids formed at lower current rate has been performed.

3. Investigations on radiography of thicker objects have been carried out using another Z-pinch system, *i.e.* PF device. These applications require neutrons and high-energy x-rays with high intensity. In this part of the work, the following studies have been performed employing the available PF devices:

(i) Established a methodology for calibrating a fusion neutron source using the continuous radio-isotopic and fission source.

(ii) Studied various parameters for x-ray and neutron radiography using an image plate (IP).

4. The PF device is a copious source of neutrons in addition to x-rays; being of pulsed nature, the PF device was employed for quantification of nuclear material in various sample matrices using active assay methodology. The study:

(i) Established a methodology for quantification of enriched uranium in laboratory waste.

(ii) Demonstrated the feasibility for the quantification of natural uranium in construction and demolition waste (CDW) of the fuel fabrication facilities using active assay by delayed neutron counting methods.

1.6 The layout of the thesis

The objective of this thesis is to explore the applications of two configurations of Z-pinches namely X-pinch and plasma focus devices in pulsed radiography and material characterization. As mentioned in this chapter, the X-pinches and PF devices are some of the most versatile laboratory sources of x-rays and neutrons due to their simplicity in operation, low cost, and transportability. Although, due to single-shot operation and inherent variations in radiation yield, Z-pinch devices are susceptible to initial constraints; these devices can be designed based on various analytical formulations provided in the literature.

In **Chapter 2,** we have described the basic theoretical background for both configurations of Z-pinches illustrating different processes that evolve leading into emission of radiation, which includes Bennett equilibrium, radiative collapse, and instabilities produced in the process.

Chapter 3 brings forward the experimental systems, various diagnostics, and methodologies used in the present work.

Chapter 4 presents the experimental results on the development, characterization, and application of the X-pinch system.

Chapter 5 presents the experimental results on the characterization of plasma focus devices for x-ray and neutron radiography and parametric optimization of moderators for neutron yield measurement.

Chapter 6 contains the results on the assay of fissile material in different sample matrices employing a plasma focus device. A study on optimization of sample and detector geometries for efficient irradiation and detection of delayed neutrons using Monte Carlo simulations is also presented in this chapter.

Finally, in **Chapter 7** the review of the present work and summary on qualitative and quantitative results obtained in both wire and gas-based plasma systems are presented. The scope for future research is also described in the chapter.

CHAPTER 2

THEORETICAL FRAMEWORK

This chapter presents the basic theoretical framework for Z-pinches (X-pinches and plasma focus devices) studied in this work. Various physical processes such as pinch formation, radiative collapse, and the radiation emission observed in the Z-pinches are explained in view of analytical formulations provided in the literature.

2.1 The Bennett equilibrium

The formation of a Z-pinches whether equilibrium or dynamic can be approximated as a column of a plasma channel, which is confined and compressed by the induced magnetic force (J × B) of a fast current (Fig. 2.1).

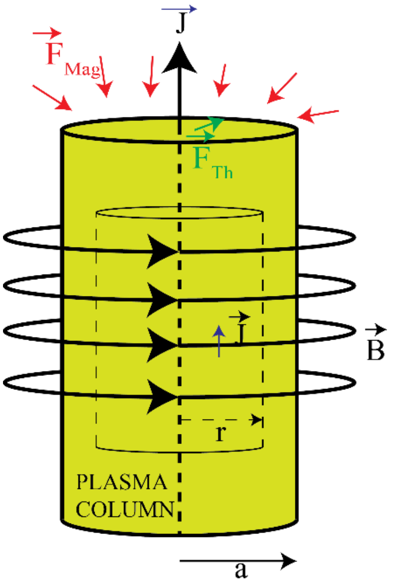

Fig. 2.1 The schematic of the plasma column with current applied in axial direction (vertical axis)

The pressure due to magnetic force in a plasma column of radius ‘r’ is given by

$$P_{mag} = \frac{B^2}{2\mu_0} = \frac{\mu_0 I^2}{8\pi^2 r^2} \qquad (2.1)$$

Where B is the magnetic field, μ_0 is the permeability of the space and I is the current driven through the plasma column. This magnetic pressure is opposed by the kinetic pressure due to joule heating and it is given by

$$P_{kin} = n_e k T_e + n_i k T_i \qquad (2.2)$$

Here n_e and n_i are the electron and ion densities of the plasma having independent temperature T_e and T_i, and k is the Boltzmann constant. To compress the plasma, the magnetic pressure should overcome the thermal pressure. The equilibrium condition between these two pressures known as the Bennett equilibrium is first formulated by W. H Bennett[2] for the streams of charges. It can be obtained by combining the two equations (Eq. 2.1 and 2.2) and solving for 'I'. For the singly charged ions and $n_e = n_i = n$ condition, the current is given by:

$$I^2 = \frac{8\pi^2 r^2}{\mu_0} nk(T_e + T_i) = I_B^{\;2} \qquad (2.3)$$

Here I_B is the equilibrium current where magnetic pressure overcomes the thermal pressure. In terms of linear particle density 'N' (multiplication of average volume particle density n by the area of the plasma column πr^2) the Eq. 2.3 reduces as:

$$I_B^{\;2} = \frac{8\pi}{\mu_0} Nk(T_e + T_i) \qquad (2.4)$$

This Eq. can be written in the more general form by assuming the same transverse temperature for ion and electrons of the plasma ($T_e = T_i = T$),

$$I_B^2 = \frac{8\pi}{\mu_0} N_e (1 + \frac{1}{\bar{Z}}) kT \qquad (2.5)$$

Here $\bar{Z}$ is the average ionic charge of the plasma. The Bennett current given by Eq. 2.4 and 2.5 is an important parameter for plasma to pinch since the current more than I_B allows the plasma to compress radially.

In the case of X-pinches where ‘n’ number of wires touch at the center points and I/n current is driven through individual wire if the total current in the load is ‘I’. For I_B as the Bennett current of the cross point, it can be calculated from Eq. 2.5 for individual wire as

$$I_{Bi}{}^2 = 8\pi \frac{N_e}{N}\left(1 + \frac{1}{\bar{\bar{Z}}}\right) kT = I_B{}^2/n$$

$$\text{Leading to } I_{Bi} = I_{Bi}/\sqrt{n} \qquad (2.6)$$

It suggests that as the total current I at the cross point approaches I_B, in the individual wires it would be I_B/n. As $I_B/\sqrt{n} > I_B/n$, for $n \geq 2$, the cross point will always be compressed due to magnetic pressure before the individual wire reached Bennett’s equilibrium. This explains the formation of a localized source of x-rays at the center of an X-pinch.

2.2 Optimization of masses in pinch plasmas

Following the work of Ryutov et. al[1], in this section, we consider the plasma column (Fig. 2.1)as an annular shell (similar to the center portion of X-pinches, single wire or wire arrays) having a uniform temperature and density. The equation of motion in presence of the magnetic pressure can be written as

$$\frac{m}{2\pi r}\ddot{r} = -\frac{B(t)^2}{2\mu} = \frac{\mu I(t)^2}{8\pi^2 r^2} \qquad (2.7)$$

Here B(t) is the magnetic field at the surface, while I(t) is the pinch current driven through the shell. If we write the shell radius in terms of the initial radius (*a*), current in terms of maximum current (I_{max}), and the time in units of rise time (τ) as:

$$\tilde{r} = \frac{r}{a}, \tilde{t} = \frac{t}{\tau}, \tilde{I} = \frac{I}{I_{max}} \qquad (2.8)$$

Then Eq. 2.7 can be written as:

$$\tilde{r}\ddot{\tilde{r}} = -\frac{\mu I_{max}{}^{2}\tau^{2}}{4\pi m a^{2}}\tilde{I}^{2} = \Pi\tilde{I}^{2} \tag{2.9}$$

Here Π is a dimensionless scaling parameter, which depends upon various parameters of the load (such as length, material, and the diameter) and the current driver (rise time and peak current) as given in Eq. 2.9. It suggests the two plasma shells driven by similar currents implode similarly and collapse at the same time if Π is the same for the two.

Moreover, for operating and optimizing the X-pinch devices on a given current generator to produce a small short-lived hotspot, the wire material and diameter can be calculated considering the scaling parameter Π to be constant for different implosions. Initial estimates of the size of the wires required for X-pinch operation can be obtained from the scaling laws of mass implosion. As increasing the radius is the only way to change the mass density of the X-pinch, so the mass should scale linearly with implosion time and the current. For efficient conversion of electrical energy to the implosion and then to radiation, one should choose an optimum mass density of the material so that the plasma column should implode at the maximum current. It infers that the value of the scaling parameter should be optimized for a given current shape.

As described by Mesyats et al.[33], in the X-pinch having a mean radius 'a' at a cross point and at the time of x-ray burst the denominator of the scaling parameter Π (Eq. 2.9) is the radial pinch compression, which can be written as:

$$\Pi = \left(\frac{v_{A}t}{a}\right)^{2} \tag{2.10}$$

where $v_A = B/\sqrt{4\pi\rho}$ is the plasma Alfven velocity that characterizes the compression, B is the magnetic field and ρ is the material density at the time of pinch. Considering the linear mass $M = 4\pi\rho a^2$, and eliminating 'a', the Eq. 2.10 can be written as:

$$\frac{I^2{}_{max}t^2\rho}{M^2} \approx Const. \qquad (2.11)$$

Eq. 2.11 clearly states that for a given current pulse the optimum mass density of the X-pinch load varies linearly with the maximum current. It can also provide an insight for choosing the suitable parameters of the load.

2.3 Radiative collapse

In addition to the pressure balance (Bennett equilibrium) in the pinch plasmas, there exists an equilibrium between input and output energies. The plasma stagnates to its axis due to Bennett conditions, then thermalizes and emits radiation. The radiation is the energy of the system leaving from it, hence provides the cooling effect to the pinch plasma. The higher radiation loss compared to the input energy supplied into the system utilizing Joule heating, results in the radial contraction, which is known as radiative collapse. It will eventually stop due to the increase in the plasma opacity and the Joule heating which leads to an increase in current and particle density. The equilibrium current at which radiative collapse occurs is known as Pease-Braginskii [100, 101] current 'I_{PB}'. The rate of Ohmic heating per unit length is given by

$$P_\Omega = 2\pi \int_0^a r\left(\frac{j^2}{\sigma}\right) dr, \qquad (2.12)$$

Here j is the current density and σ is the conductivity of the plasma, which can be taken as constant current density and Spitzer conductivity as [102]

$$j(r) = j_0 = I/\pi r^2 \text{ and, } \sigma = \sigma_0 T^{3/2}/\check{Z} ln\Lambda, \qquad (2.13)$$

Here σ_0 is the constant which is equal to 1.03×10^{-4} (in MKS units), Ž is the effective charge and lnΛ is the Coulomb logarithm, which is in the range of 7 to 20[103]. Considering the radiation emitted from the plasma as Bremsstrahlung, the radiated power per unit length is:

$$P_b = 2\pi S \int_0^a Z{n_e}^2 T^{3/2} r dr \qquad (2.14)$$

Here S is a constant of value 1.69×10^{-4}(in MKS units). For an optically thin plasma, the power balance is given by

$$P_\Omega = P_b \qquad (2.15)$$

Which provides the equilibrium current i.e. Pease-Braginskii current (I_{PB}). For a fully ionized plasma the Eq. 2.15 provides:

$$I_{PB} = 0.433(\ln\Lambda)^{1/2} \qquad (2.16)$$

In the X-pinches, the current is in the range of the I_{PB}, where the thermal pressure is neutralized by the magnetic pressure, which compresses the plasma at the neck of the pinch.

2.4 Analytical estimation of x-ray power and pinch radius

The Z-pinch plasma dynamics is mostly affected by m=0 (Sausage) and m=1 (Kink) type of instabilities among others. These are shown in Fig. 2.2. The m=0 instabilities [43] developed in the plasma column (Fig. 2.2a) of the neck region of the X-pinches (Fig. 2.2b) are responsible for the formation of micro-pinches that leads to the generation of intense x-rays from a small region (hot spots). These instabilities are developed as a result of a small perturbation in the plasma column that disrupts the pressure equilibrium. In the low Z materials, the pinch resistance is too low for Ohmic heating to be dominant over the magnetic pressure. In such a case the heating in the plasma channel is due to the development of m=1 instabilities. In the higher Z materials, the plasma resistance is significant for heating the plasma.

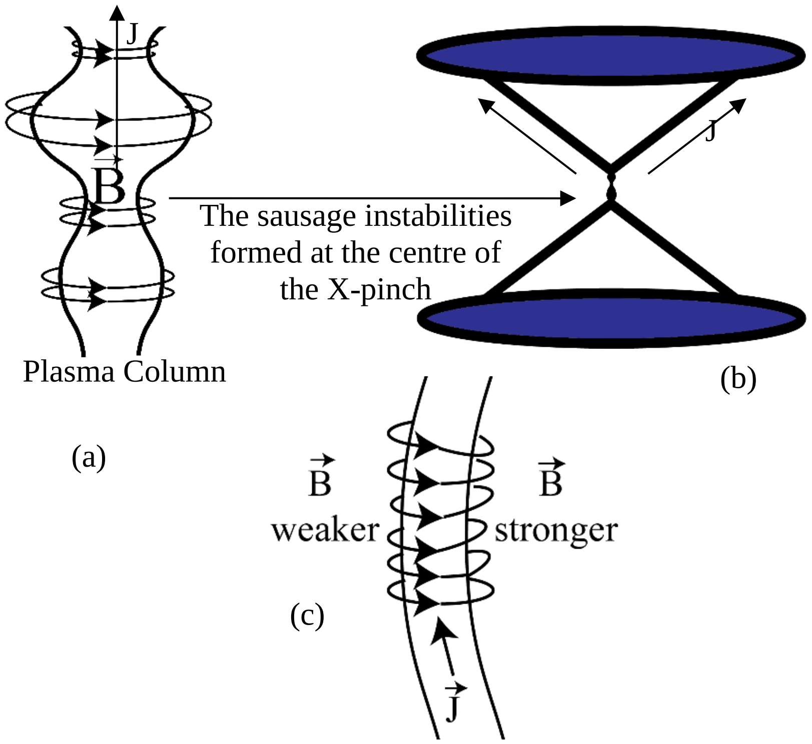

Fig. 2.2 The instabilities formed in the plasma column (a) m=0 (Sausage) instabilities formed in the neck of the X-pinch (b) x-pinch showing the m=0 instabilities (c) the m=1 (Kink) instabilities

Moreover, the m=0 instabilities developed in the plasma column of the high-density Z-pinch undergo a radiative collapse. The radiative cooling prevents the thermal pressure to build up which allows the plasma column to compress due to the magnetic field until the plasma becomes optically thick. It then behaves like a black body that sets the upper limit to compression.

The condition for this equilibrium is the combined effect of pressure and power balance, i.e. Eq. 2.3 and Eq. 2.15. The pressure balance condition for the ionic charge $\check{Z}>>1$ is given as:

$$\mu_0 I^2 = 8\pi \check{Z} N k T_e \tag{2.17}$$

The power balance condition for a blackbody source of radiation temperature T_R is given by

$$\sigma {T_R}^4 2\pi r = n j^2 \pi r^2, \tag{2.18}$$

Here the current density is given by $I/\pi r^2$

Solving Eq. 2.17 to 2.18 by assuming the plasma resistivity as Spitzer resistivity (Eq. 2.13), a constant ratio between radiation and electron temperature ($\beta = T_R/T_e$) and approximating $\check{Z} = fT_e^{1/2}$, the radius of the hotspot obtained is in the form:

$$r = 2.13 \times 10^{-18} I^{-14/9} \beta^{-4/3} f^{13/9} N^{10/9} ln\Lambda^{1/3} \text{ (m)} \qquad (2.19)$$

The power emitted in the form of radiation is obtained by placing the value of *r* to the left term of Eq. 2.18 and rearranging.

$$P = 6.7 \times 10^{22} I^{\frac{34}{9}} \beta^{8/3} f^{-11/9} N^{-14/9} ln\Lambda^{1/3} \text{(W/m)} \qquad (2.20)$$

Eq. 2.19 suggests that as the line density decreases up to a critical value, the plasma radius in the neck starts to diminish (r→0). Below this point, the electron drift velocity ($=J/n_e e$) exceeds the critical velocity, which is of the order of ion sound speed ($= \sqrt{[\frac{\check{Z}T_e+T_i}{m_i}]}$) and the micro-instabilities[98] start to grow up. The critical line density can be estimated using Bennett relation (with temperature eV's) and combining the drift velocity to the ion sound speed c_s.

$$8\pi N_i e\left(\tilde{Z} T_e + T_i\right) = \mu_0 I^2, \qquad (2.21)$$

Here, $I = \check{Z} N_i e c_s$ and $c_s = \sqrt{e\left(T_i + \tilde{Z} T_e\right)/m_i}$ (2.22)

$$N_c = \frac{16\pi m_i}{\mu_0 e^2} = 1.3 \times \frac{10^{18} A}{\tilde{Z}^2} \qquad (2.23)$$

Thus in the neck region in a Z-pinch, when the N_i drops below N_c, the plasma resistivity increase far more than the Spitzer value, and the plasma is heated by the Ohmic heating and results in the explosion of micro-pinch. Assuming Ž~Z=A/2, the Eq. 2.23 results into critical mass density per unit length of ~8 kg/m.

The critical mass density provides an estimate for the minimum radius that can be obtained in the pinch process. The minimum radius (Eq. 2.19) scales as:

$$r_{min} \sim I^{-14/9} Z^{-10/9} \tag{2.24}$$

These results provide an insight into the minimum radius and maximum x-ray power that can be achieved in X-pinches. This also infers that the radiative collapse in the pinch plasmas can be utilized to produce the high-density state of the material[1, 43].

CHAPTER 3

EXPERIMENTAL SYSTEMS AND MEASUREMENT METHODOLOGIES

In this chapter, we describe the experimental systems and diagnostics developed and employed for the study reported in the present thesis. A brief discussion on the basic principles of various diagnostics is also provided. The details are discussed in two major sections (i) diagnostics used in the development and characterization of an X-pinch system followed by methodology for point projection radiography (ii) optimization studies of the plasma focus device for applications pertaining to radiography and material characterization. The former section focuses on the development of an X-pinch system on a slow current driver, methodologies used for its characterization in terms of x-ray yield, source size and a number of x-ray bursts, and point projection radiography of exploding wire using X-pinches as a point source. The later section includes the studies carried out for characterization of PF device for neutron and x-ray radiography, optimization of a detection system for yield measurement, and neutron radiography. The technique for an application towards characterization of nuclear material in industrial waste using plasma focus device has also been discussed in this section.

3.1 Setup and diagnostics used for development and characterization of X-pinch

3.1.1 Experimental set-up

The X-pinches have been developed on a slow current generator (<0.1 kA/ns) that utilizes a 2 μF capacitor. The single capacitor-based system makes it compact and easy to handle. The capacitor of maximum charging voltage of 60 kV is connected to the X-pinch load through a triggered spark gap as shown in Fig. 3.1 and the electrical parameters of the current driver are listed in Table 3.1. The details of the measurement of these parameters are provided in the subsequent subsections of this chapter.

As the x-rays emitted from the X-pinches are in a softer energy region, the load assembly is housed inside a vacuum chamber which can be maintained at vacuum levels up to5×10^{-5} mbar during experiments. Various electrical, optical, and x-ray diagnostics to the load are connected through vacuum ports as shown in Fig. 3.1c.

Table 3.1 The parameters of the current driver employed for X-pinch studies

Parameters	**Value**
Capacitance	2 μF
Inductance	202 nH
Operating voltage	40 kV
Maximum Peak Current	115 kA
Time Period	4.2 μs

Two or four-wire X-pinches made of different metals have been mounted in between the electrodes in the vertical direction as shown in Fig. 3.1b. The inter-electrode gap for all the experiments was kept ~13 mm. In the two-wire X-pinches, the angle between crossed wires was kept 80^0 as the low vertical angle of an X-pinch behaves like single wires and no hot spot can be observed at higher achievable angles ($>90^0$) as reported by S. Pikuz*et al.*[72]. To mount the X-pinch loads, the wires were placed in parallel and then the upper electrode was rotated by 185^0 maintaining an inter wire angle of 80^0. The details of the X-pinch loads are listed in Table 3.2.

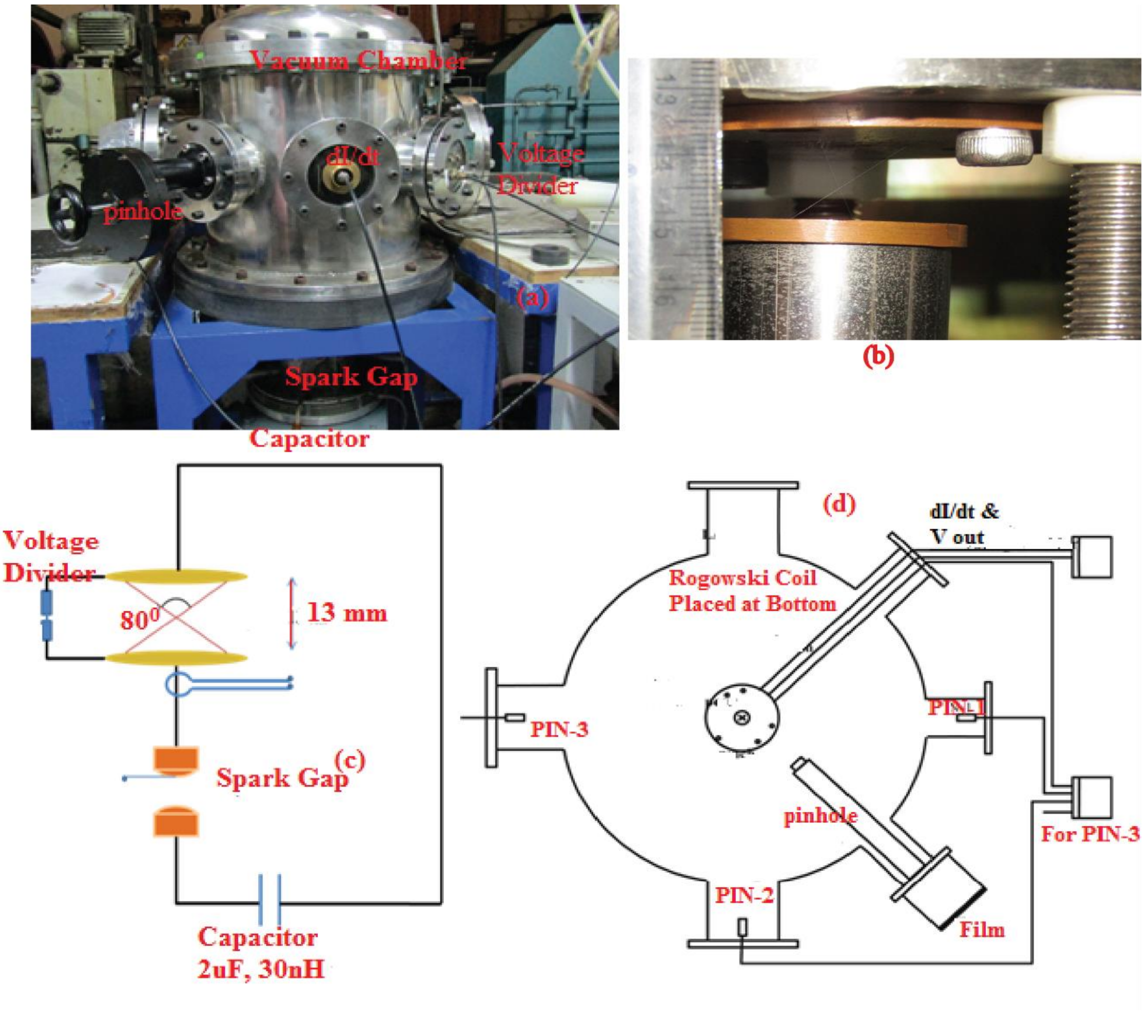

Fig. 3.1(a) Photograph of experimental system (b) The X-pinch wire mounted in-between electrode (c) The Schematic of the X-pinch depicting various diagnostics (d) Diagnostics used for current, voltage and x-ray measurements.

Table 3.2 The X-pinch load description

Parameter	**Value**
No of Wires	2 or 4
wires	7.5 μm W, 13 μm W, 13 μm Mo, 15μm Cu (15 μm Cu coated with 2.5 μm polyamide) and 25 μm Al
Vertical Angle	40^0

In this work, we have studied the X-pinches made of refractory metals (W or Mo) or non-refractory metals (Cu or Al). The linear mass density of the X-pinch is given by

$$m* = \frac{nm}{cos\,\varphi}, \qquad (3.1)$$

Here n is a number of wires, m is linear mass per unit length of the wire and Φ is the inclination angle of the wire from the vertical axis. The linear mass density of the X-pinch was varied from 22 µg/cm to134 µg/cm by using wires of different materials as listed in Table 3.3.

Table 3.3 Linear mass density of various X-pinch configurations

Metal type	XP configuration	Linear mass density (µg/cm)
Refractory metals	2 × 7.5 µm W	22.3
	2 × 13 µm Mo	35.6
	4 × 7.5 µm W	44.5
	2 × 13 µm W	66.9
	4 × 13 µm Mo	71.2
	2 × 25 µm Mo	131.7
	4 × 13 µm W	133.8
Non-refractory metals	2 × 25 µm Al	34.6
	2 × 15 µm Cu	36.0
	2 ×15 µm Cu coated with 2.5µm polyamide	45.4

The diagnostics used for the X-pinch system based experiments include in-situ calibrated Rogowski coil placed at the bottom of the centre electrode (Fig. 3.1c) for current measurement and the resistive voltage divider placed across the load. The PIN diodes have been used for the measurement of yield and the temporal history of the x-rays. A pinhole camera with single or multiple pinholes has been used for study of spatial profile of the x-ray source. In addition to pinholes, slit wire camera and radiography method were also employed for the source size measurement. The x-rays images through pinholes and point projection radiography of the exploding wires were recorded on x-ray films. The details of these diagnostics are discussed in subsequent sub-sections.

3.1.2 Current measurement using Rogowski coil

The Rogowski coil works on Faraday's law of magnetic induction and it consists of a toroidal winding encircling the current conductor. As the current is flown through the conductor, the magnetic flux linked to the loop changes according to the variation in the current; this induces a voltage (*u(t)*) across the coil, which is given by:

$$u(t) = \frac{d\varphi}{dt} = \frac{d}{dt}\int \vec{B}.\vec{dA} = \frac{A}{N}\mu_0\dot{I} \qquad (3.2)$$

Here A, $\dot{I}$, and N are the cross-sections of the winding, the current derivative, and the number of turns per unit length, respectively. The integration of this induced voltage w.r.t time is directly proportional to the current flowing through the conductor. An RC circuit (shown in Fig.3.2) can be connected across two ends of the Rogowski coil to obtain the current.

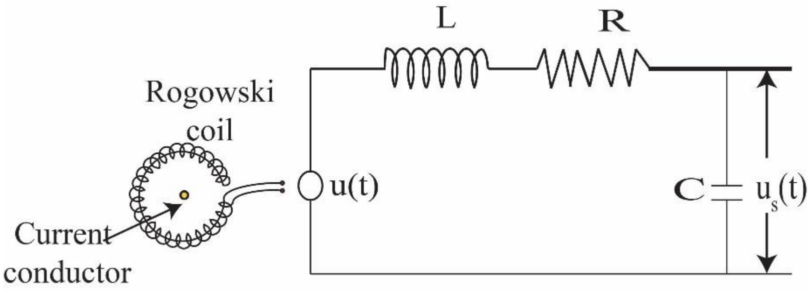

Fig. 3.2 Schematic of the equivalent circuit of Rogowski coil

Solving for the voltage for the circuit shown in Fig.3.2, we get:

$$u(t) = \frac{d\varphi}{dt} = L\frac{dI}{dt} + RI + \frac{1}{C}\int Idt \qquad (3.3)$$

Here R and C are the resistance and capacitance of the integrator circuit and L is the inductance of the coil. If ωL<<R and measurement time t<<RC, with ω being the highest frequency in the Fourier spectrum of current source; the first and third term of Eq. 3.3 can be neglected in comparison to the middle one. The voltage across the capacitor then can be written as[104]:

$$u(t) = \frac{d\varphi}{dt} = RI \tag{3.4}$$

$$u_s = \frac{1}{RC}\int \frac{d\varphi}{dt}dt = \left\{\frac{A\mu_0}{NRC}\right\} I(t) \tag{3.5}$$

As the Rogowski coil is encircling the current conductor, the flux or the derivative of current associated with it does not depend upon the relative position of the current-carrying conductor. Therefore, the relative position of the coil does not affect the calibration factor.

In our experiments, we have placed a 15 cm long Rogowski coil around the center electrode (anode), and one similar coil was also placed for triggering the oscilloscope that records the signals of PIN diodes used for the detection of x-rays (section 3.1.4). The coil comprises 30 numbers of turns. The inductance of this loop is ~220nH and the R and C of the integrator circuit is 820Ω and 100nF, respectively, making the time constant to be 82µs, which is in agreement with the condition t<<RC.

To calibrate the Rogowski coil, the current derivative and its integrated output under short circuit conditions have been obtained by connecting a 6 mm diameter copper rod between the electrodes instead of an X-pinch load. The capacitor is charged up to a certain voltage and discharged into this short-circuited load. The integrated output of the coil has been compared with the theoretically estimated value obtained using a standard circuit equation, which is given by

$$I_{peak} = V_{CH}\sqrt{\frac{kC}{L}} \tag{3.6}$$

Here V_{CH} is the charging voltage, k is the voltage reversal factor, C and L are capacitance of the capacitor bank and inductance of the circuit, respectively. The voltage reversal factor can be obtained by averaging the ratio of the consecutive current peaks. The inductance of the circuit can be estimated using

$$T = 2\pi\sqrt{LC} \tag{3.7}$$

The calibration factor so obtained has been used to estimate the current in the X-pinch experiments. For the presently developed system, the calibration factor is obtained to be 8 kA/V.

3.1.3 Estimation of deposited energy into wire

A resistive voltage divider having a ratio of 1000:1 was placed across the electrodes of the X-pinch and the exploding wire for monitoring the developed voltage during a wire explosion. The observed voltage consists of resistive as well as the inductive term. The resistive part can be estimated by subtracting the inductive term (LdI/dt) i.e.

$$V_r(t) = V(t) - L\frac{dI\,(t)}{dt} \tag{3.8}$$

The inductance L mainly consists of the system inductance (L_s) and the wire inductance (L_w); the L_s can be estimated through the waveforms of short-circuit experiment and L_w can be evaluated using the following relation:

$$L_w(nH) = 2l \ln d/r_w \tag{3.9}$$

Here 'l' is the length (in cm) of wire and 'd' is the distance from the main conductor and 'r_w' is the wire radius. The wire inductance, being very small (~22 nH) in comparison to the system inductance (200 nH), is neglected for voltage calculations. The resistive voltage so obtained (from Eq. 3.8) has been used to estimate the electrical power and the resistance during the wire explosion. The electrical power can be estimated by multiplication of resistive voltage and the current, the time integration of electrical power normalized to the number of atoms provides the energy deposited into the wire. The time integration of the electrical power till the time at which resistance drops to half of its maximum value provides the energy deposited into the exploding wire. At this moment the applied energy is split between the wire core and the corona as the resistance decreases during the breakdown.

3.1.4 X-ray yield measurement using PIN diodes

We have used Si PIN diodes for the measurement of the yield of soft x-rays and their time history. To detect the x-rays, ‘AXUV’ type PIN diodes (AXUV-5) have been used. The reason behind the selection of these diodes is their easy availability. Further, though, sensitivity data for these diodes are not available, the same for the similar type of detector is well known in wide energy range in the softer region. The sensitive area of this detector is 5 mm^2. As the sensitivity of the presently employed AXUV-5 detectors is not available in the literature, we have used spectral sensitivity data of the AXUV-100. The active area of AXUV-100 is 100 mm^2, so the sensitivity of the currently used PIN diode has been approximated considering the area of 5 mm^2 of AXUV-100 instead of 100 mm^2, in a way similar to that considered by Pikuz *et al.*[72]. The sensitivity of the AXUV-5 derived from the data available from Idzorek [105]*et al.*is plotted in Fig. 3.3a. It is seen to be almost flat (0.0135A/W) for x-ray energy ranging from 100eV to 5keV.

The timings (wire explosion, x-ray bursts, etc.) measured and referred to in the experiments are with respect to the current derivative (dI/dt) signal obtained using Rogowski coil, which upon integration provides the current. As the detectors are sensitive to the lower energy radiation up to visible and EUV and the radiations from the X-pinches are flooded with visible and EUV photons, we have placed x-ray filters before PIN diodes. These filters coupled with PIN diodes were mounted on one of the flanges placed at 22 cm from the center of the source. The x-ray filters are made of thin plastic films or metallic foils that enable to absorption of the photons below the cut-off energy. We have used 6 μm, Al, 50 μm Be, 12.5 μm Ti, 240 µm Be and 25 µm Cu foils for the filtering the low energy radiation. The x-rays signals obtained after these filter configuration covers the energy range from 1 keV to 9 keV. The transmission of the filters evaluated from the absorption coefficient mentioned in the CXRO database[106] is plotted in Fig. 3.3b.

The radiation yield recorded by filter equipped PIN diodes have been estimated using the following relation:

$$Y = \frac{1}{S*R}\int_0^\infty V_d(t)dt \qquad (3.10)$$

Here $V_d(t)$ is the output voltage pulse registered in the PIN detector, R is shaping resistance of biasing circuit, S is spectral sensitivity of Si-PIN detector as plotted in Fig. 3.3a. Considering the radiation emission to be isotropic, the energy-filtered x-ray yield (w) of the source can be obtained from the registered yield in PIN diodes as:

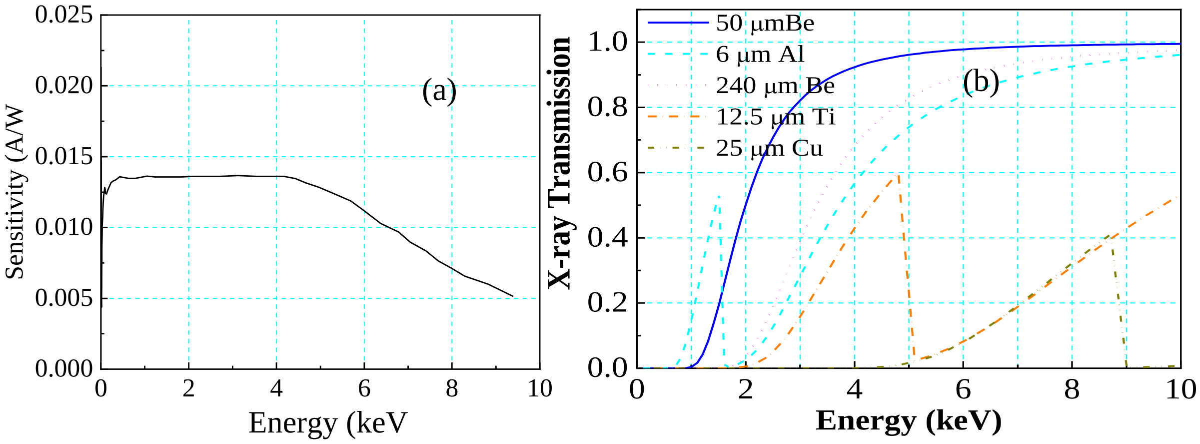

Fig. 3.3(a) The sensitivity of PIN diodes w.r.t x-ray energy (Idzorek et.al.) (b) The x-ray transmission from thin metallic foil filter (from CXRO database) coupled with PIN diodes and the films.

$$w = \frac{16r^2Y}{d^2} \qquad (3.11)$$

Here ‘r’ is the distance of the detector from the source and ‘d’ is the active diameter of the Si-PIN detector. The x-ray yield and jitter in timings for present experiments have been estimated by averaging multiple shots of similar dI/dt.

3.1.5 Measurement of x-ray source size using a pinhole camera

The pinhole camera is one of the most versatile and widely used set-ups for the measurement of source size in optics since ages. In the current experiments, time-integrated pinhole cameras with single pinhole or multi-pinhole have been used to image the x-ray emitting region of the plasma. Each channel of multi-pinholes was filtered with different thin metallic foil filters to get the energy information. The schematic of the multi-pinholes is shown in Fig. 3.4. The pinhole camera is consisting of a pinhole mount, the film holder, and the diagnostic channel. Magnification (m) and the geometrical spatial resolution (Δ_{geo}) of the camera is given by:

$$m = \frac{b}{a} \text{ and } \mathit{\Delta}_{geo} = d(1 + \frac{1}{m}) \qquad (3.12)$$

Here ‘a’ and ‘b’ are the distances of x-ray source to pinhole and pinhole to film, respectively. To reduce the geometrical spatial resolution (blurring), the pinhole should be chosen of smaller diameter as it depends upon the diameter of the pinhole. The intensity of the x-rays through the pinhole is given by

$$I \propto \frac{d^2}{a^2} \qquad (3.13)$$

Eq.3.13 and 3.12 infer that to image a source with better resolution, 'd' and 'a' should be smaller.

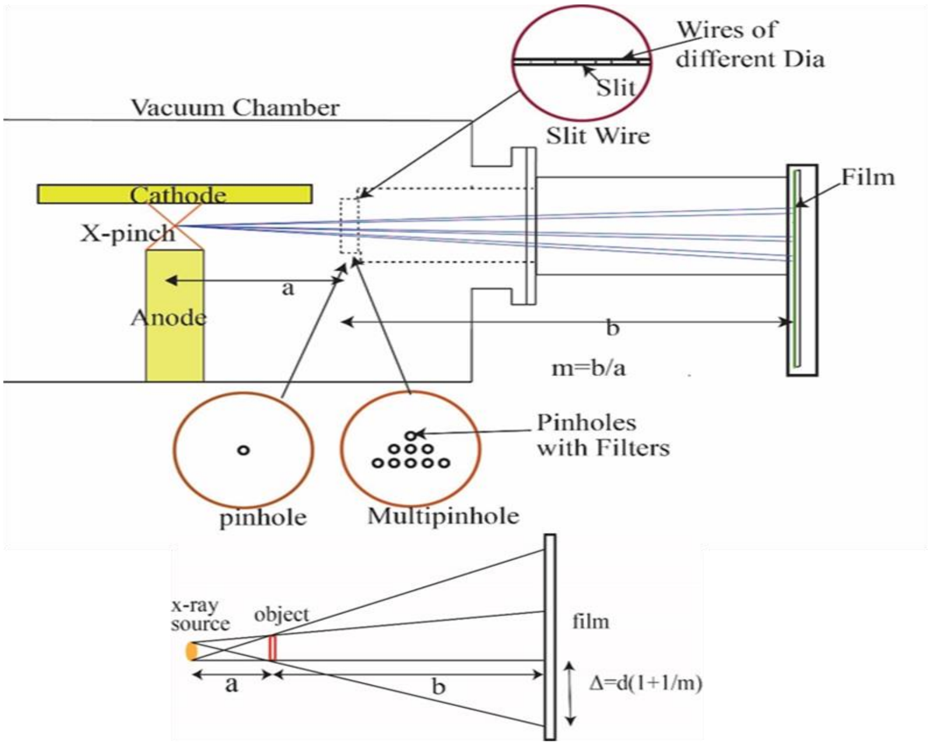

Fig. 3.4 Schematics of diagnostics used for time-integrated source profile of X-pinch with a single pinhole, multi-pinhole and slit wire. The penumbra formed in the radiography of object is also shown.

In addition to geometrical blurring, the smaller pinhole cuts off low-energy radiation due to diffraction. The limiting wavelength (λ) of radiation of the pinhole (or slit or wire) can be estimated from:

$$\Delta_{diff}[\mu m] \sim (a\lambda)^{1/2} \qquad (3.14)$$

Here λ is in Å and 'a' is in cm. The diffraction spread of the image on the film is given by 'Δ'_{diff}=bλ/d. We have used the smallest pinhole of 25μm diameter to image the smaller source formed in the plasma. Using this, in the present set of experiments, the resolution observed to be 30 μm and it can cut off the radiation below ~200 eV. This pinhole was used without any filter, which can provide spatial information on the low energy x-ray emitting region formed in wire plasma. The source size has been approximated by taking the width of the source in line profile where the intensity falls to 10% of the maximum. To estimate the other low energy emitting region of the plasma, smaller pinholes (50 & 100μm) with 25μm Be and 50 μm Be filters have been used. The hard energy wider x-ray sources were imaged using comparatively wider pinholes (200 and 400μm) with thicker (Ti and Cu) filters.

The images of the x-rays were recorded on AGFA D4 film, Kodak Biomax MS film, and Kodak Biomax light films.

3.1.6 X-ray source size measurement using slit wire method

As the pinholes have a limitation due to low intensity in smaller pinholes, we have designed a slit wire camera to determine the parameters of small and bright hotspots produced in the X-pinches. It consists of a narrow slit that produces an image of an x-ray emitting plasma in 1D and a set of very thin wires of varying diameter were mounted across the slit. The set of wires were selected such that the diameter of the wire covers the complete length scale of the emitting sources. The slit is aligned orthogonal to the axis of the X-pinch as shown in Fig. 3.4. The magnification of the image is so adjusted that the images of the wires do not overlap with each other. The hotspots and other plasma structures in an X-pinch will create the image of the slit and wire, which makes it easier to determine the plasma structure in the given energy range selected by the filter. The dimension of the shadow of the wires (or slits) is determined by:

$$S = \frac{(a+b)}{a} d = (1 + m')d \qquad (3.15)$$

The shadow of wire of the smallest diameter visible in the image provides an idea for the dimension of the source. As the source size due to different processes in X-pinches can range from a few μm to ~100 μm, we have fixed the tungsten wires of 120μm, 80μm, 35μm, 25μm, 13μm, and 5μm diameter upon a 100μm slit. It was placed at 200 mm from the X-pinch source, providing an image magnification of 2.15. The radiograph was obtained on an AGFA D4 film placed behind Al (6 μm) filter, which filters the x-ray energy below 1 keV.

3.1.7 X-ray source size measurement using radiography method

Apart from the slit wire method, the radiography method can also be used to overcome the disadvantage of the limited transmitted emittance of the pinhole. In this method, the spot size of the x-ray source can be estimated using the size of the penumbra of the image. The penumbra is formed when the size of the x-ray source is comparable to the size of the object. The width of the penumbra is related to the size of the source by

$$s = a\Delta/b, \tag{3.16}$$

Here 'a' and 'b' are the distances as shown in Fig.3.4d.

Considering the geometric optics, the penumbra width decreases with the source size and tends to zero for a point source, however, due to the wave nature of radiation, the diffraction affects the object image (P) at the film and can be estimated by the ratio of first Fresnel zone R to the object size 'd'.

$$p = \frac{R}{d} = \frac{1}{d}\sqrt{\frac{\lambda ab}{a+b}} \tag{3.17}$$

Here λ is the wavelength. If p<<1, the formed image covers a large number of Fresnel zones, which infers that the diffraction effect is negligible. For p~1, the image covers the first few zones and it overlaps at the boundary.

In this work, the radiography method has been implemented to estimate the source size using a wire mesh made of 35 μm W wires. A wire mesh was placed at 200 mm from the source and the magnification of the image was 2.3. The radiographs of this wire mesh have been obtained for few configurations. Considering the geometric optics, the source size ‘s’ has been estimated from the horizontal line profile of radiograph using the Eq. 3.16.

3.2 Point projection radiographic studies on exploding wires using X-pinch x-ray source

The optical interferometric technique is a suitable method to image the coronal plasma of the exploding wire; however, it can’t image the high-density core due to its high opacity. To investigate the core of an exploding wire, point projection x-ray radiography is a suitable technique. The small micro source produced in the X-pinch (described in the following chapter) with an energy range of 1-6 keV is an ideal source for backlighting the exploding wire plasma at post burst stages.

In the present study, the spatial profile of the exploding wire mounted on one of the return conductors has been obtained. The schematic of the set-up is shown in Fig. 3.5. The distance of the X-pinch source to exploding wire was 5 cm and the distance of wire to film was 35.7 cm giving rise to the magnification of the image as ~8. The radiographs have been obtained on films of different sensitivity and resolution i.e. AGFA D4, Kodak Biomax MS, and Kodak Biomax light films. The films were filtered with 6.5µm thick Al foil to cut off the x-rays of energy less than 1 keV. As the timing of the x-ray pulse in an X-pinch can be varied using wires of different diameters, the spatial profile of the exploding wire plasma at different instances has been imaged. The average velocity of expanding wire core has also been estimated from the obtained radiographic images.

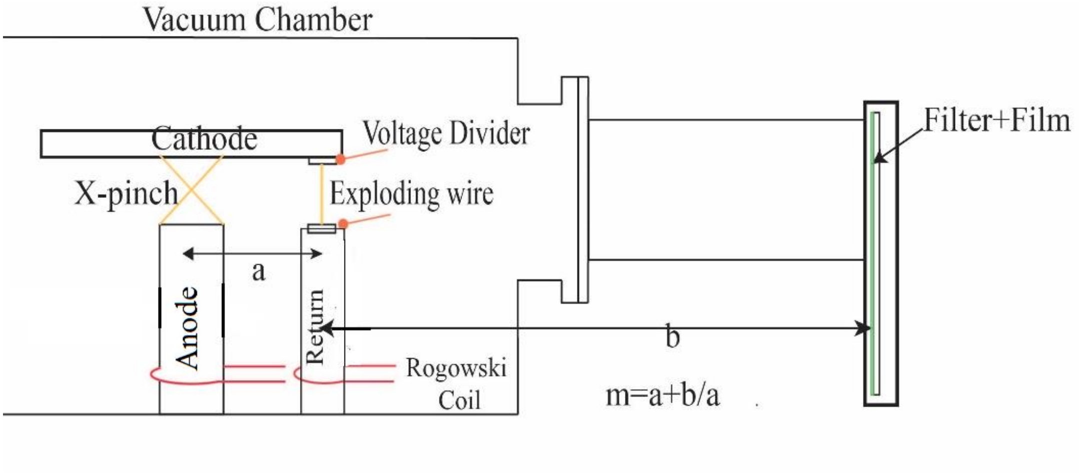

Fig. 3.5 The schematic of exploding wire mounting in return conductor of the X-pinch

3.2.1 Film processing

The films were processed manually according to standard development procedures. To get the digital image of the recorded films, the films were scanned using an image scanner with a resolution of 9600 dots per inch (dpi). The pinhole and radiographic images were processed using the software 'ImageJ'[107], freely available on an open platform. The sizes of different structures formed in the radiography were estimated by scaling the physical length of one or more edges with the image pixels.

3.3 The investigation on radiography and material characterization studies using PF device

This section includes the studies namely the radiography and the fissile material characterization carried out using another Z-pinch configuration i.e. plasma focus devices. We have employed three previously developed PF devices (i) MEPF-12[108], (ii) MEPF-25,and MEPF-17[109]. All the devices are based on Mather-type geometry. The former two are developed on 12 kJ and 25 kJ capacitor bank (CB), respectively, and the PF is mounted on top of the CB through a spark gap. The later one is developed on a 17kJ capacitor bank and the PF is connected to the spark gap of CB through a transmission line. Although the design and development of the PF device is not in the scope of this work, however for the sake of completeness we describe here the MEPF-17 PF device as this has been utilized for conducting some of the research work contained in the thesis.

3.3.1 MEPF-17 PF system

The medium energy plasma focus (MEPF-17) is a coaxial cable transmission line-based device in which the plasma focus head (neutron source) is conveniently located away from the regular activity area and can be oriented in any direction suitable for specific applications. The plasma focus assembly is placed inside the cabin with only the plasma focus head coming out through a window of a diameter of 200 mm. For regular operation, the plasma focus head has been placed horizontally and the samples were placed along an axially forward direction as described in later section (section 3.4.2). MEPF-17 device has been operated with 5 mbar of D_2 gas pressure at operation energy of 17.3 kJ (60 µF, 24 kV). The average neutron yield of $(2.1\pm0.8)\times10^8$ neutrons/ pulse and maximum neutron yield of $(4.6\pm0.5)\times10^8$ neutrons/pulse has been produced in the radial direction with neutron pulse duration (FWHM) of ~50 ns. However, because of the anisotropic emission of neutrons in PF devices, the yield in the axial direction was estimated to be more[109]. In the MEPF-17 device, the average anisotropy factor i.e. ratio of neutron yield in the axial direction to that in the radial direction was calculated to be around 1.33±0.18. This anisotropy can be attributed to the dominance of beam target fusion over thermonuclear fusion in the device.

Furthermore, in the plasma focus experiments, a magnetic pickup coil has been used for current measurements. It works on the same principle as the Rogowski coil and consists of a small wire loop that can be placed near the current-carrying conductor. As the flux (so is the current derivative) associated with the loop is dependent on the relative position and the current-carrying conductor, the signals from the magnetic pickup loop have been used for triggering the associated electronics i.e. counting electronics of detectors.

3.3.2 The neutron yield measurement in plasma focus device

The time-resolved x-ray and neutron emission measurement from the plasma focus device has been carried out using a plastic scintillation detector (PSD) coupled to a photomultiplier tube. The PSD is operated at a voltage of 1800 V. For neutron energy measurement, the PSD was positioned at 3m in the radial direction. The separation time (time of flight) of the x-ray and the neutron pulse has been used to estimate the neutron energy. The signals from these detectors were recorded in a digital storage oscilloscope (1 GHz, 5 GS/s) placed inside an electro-magnetic shielded enclosure (Faraday cage).

For measurement of neutron yield, a calibrated Geiger–Muller (GM) counter-based silver activation detector (SAD) has been used. It was placed at the 1 m distance from the PF device in the radial direction. The SAD has been in-situ calibrated with a Pu-Be neutron source of strength 1×10^5 n/s.

3.3.3 Radiographic studies in PF device

As described in section 1.2.7 of chapter 1, the x-ray emission from the PF device is in the energy range from a few hundred eV to a few hundred keV. These high-energy x-rays can be utilized for the radiography of thick samples using imaging plates as a detector.

The image plates are widely being used now a day in various imaging applications vis. a vis. diffraction studies, radiography, and particle detection. The high spatial resolution, high sensitivity to x-rays, and linear response to radiation dose make them an ideal detector for such applications. An image plate is a two-dimensional phosphor having a composition of BaFBr:Eu^{2+}. The latent image is formed in form of F^+ centres and Eu^{3+} when radiation is incident on the IP, which can be read by irradiating the IP with the laser. The intense light of the laser excites the trapped electrons to recombine with Eu^{3+}, which emits photons of wavelength 400 nm known as the photo-stimulated luminescence (PSL)[110]. The PSL is recorded by photomultiplier tubes and converted into a digital image. To erase the residual image from IP, a strong visible light is used, once erased it can be used ad Infinitum. The sensitivity [110]of the imaging plates is plotted in Fig. 3.6.

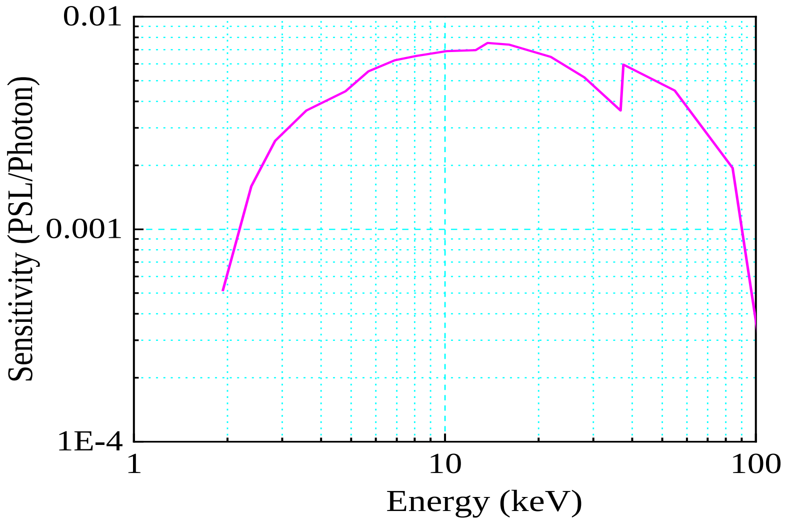

Fig. 3.6 The sensitivity of the image plate (BAS-SR)

In the present work, we have used commercially available Fujifilm BAS-SR and Dürr NDT blue image plates. The image plate has a dimension of 20 ×25 cm^2 (BAS-SR) and 18 ×24 cm^2(Dürr). After the neutron exposure, the IPs were scanned with a suitable scanner with 50μm resolution and the digital image is stored in 14-bit gradation. In the case of saturated PSL, the image plates were scanned multiple times without erasing. Due to successive scanning, the PSL of IP fades exponentially and clear radiographs are obtained. In the case of single-pulse experiments such as in PF devices, this procedure provides an advantage of using an image plate over conventional film radiography.

To carry out neutron radiography, we have used BAS-ND image plates of 20 ×25 cm^2 size. These are consist of $BaFBr:Eu^{2+}$ as a phosphor mixed with gadolinium oxide (Gd_2O_3) dispersed in the polymer matrix. The reaction of Gd with neutrons produces a conversion of electrons of average energy 70keV. These electrons excite phosphors and the latent image of the radiograph is stored. After neutron exposure, the latent information stored on the image plate can be read out as photo stimulated luminescence (PSL) intensities using an imaging plate scanner and analyzed. Since $BaFBr:Eu^{2+}$ is being used in NIP's these are also sensitive to γ-radiations.

3.3.4 Optimization studies of Z-pinch devices for neutron yield measurement

Being a single-shot device and large shot-to-shot variation in the neutron yield, absolute calibration is not possible using the Z-pinch-based pulsed source. To quantify the yield, the detectors are needed to be calibrated beforehand, which is generally carried out using fission/radio-isotopic sources such as ^{252}Cf, Pu-Be, and Am-Be. The neutron yield in high yield fusion devices can be determined using foil activation detectors but for low yield devices, the proportional counter detectors appear to be a better option owing to their significantly higher sensitivity to thermal neutrons. Furthermore, the fraction of thermal neutrons in the spectrum of sources whether fission or fusion, even after moderation is quite small (up to a few percent). Therefore, to maximize the performance of thermal neutron detectors a selection of appropriate moderating material and optimizing their thickness becomes important.

To estimate the thermalization properties of the moderator and develop a methodology of neutron yield estimation from PF devices, Monte Carlo simulations have been carried out employing FLUKA[111], an openly available code for simulating particle transport. This code has been widely used in various physics applications which include detector development, shielding designs, calorimetric, activation of materials, accelerators, cosmic rays, accelerator-driven systems, neutrino physics, and radiotherapy, etc.

We have utilized ^{3}He and BF_3 proportional counters for the detection of neutrons originating from fission or fusion sources. The length of the ^{3}He detector is one meter with a pressure of 3 bars and 1.5 bars of ^{3}He and Kr gases, respectively. The addition of Kr gas provides stopping power to the electron-ion cloud that minimizes the wall effect in proportional counters. The active length and the diameter of the detector were 920 mm and 38 mm respectively. The BF_3 detector is 50 mm in diameter and one-meter-long with an active length of 920 mm. The gas pressure of BF_3 in the detector is 550 torr. The moderator under consideration is placed in front of the detector at a touching position. The absolute efficiency of the detector is calculated for moderator thicknesses varying from 0 to 200 mm in steps of 20 mm.

Furthermore, the ^{3}He and BF_3 detector banks have also been simulated (in addition to single detectors). The ^{3}He detector bank consists of six proportional counters (described above) connected in sum mode and embedded in a grooved perspex moderator. The size of grooved perspex sheet is 5cm (t) × 32 cm (w) × 96 cm (l). The BF_3 detector bank consists of five single proportional counters embedded in a grooved perspex moderator of thickness 70 mm. The size of this grooved perspex sheet is 7cm (t) × 36cm (w) × 100cm (l) for BF_3 detector bank.

The neutron source is encapsulated in an aluminum cylinder having 4 cm diameter and 10 cm height. It is placed at 100 cm from the surface of the detectors with isotropic spatial source distribution being assumed for all the cases. The energy spectrum of the Pu-Be source is taken from the continuous spectrum by digitizing it in 46 energy bins. The ^{252}Cf source energy spectrum is sampled according to Watt spectrum with probability density being taken as[112]

$$P(E) = Ce^{-\frac{E}{a}}Sinh(bE)^{\frac{1}{2}} \qquad (3.17)$$

where C, a, and b are constants that depend upon the type of isotope

$$C= (\frac{\pi ab}{4})^{1/2}e^{\frac{ab}{4}}a \qquad (3.18)$$

The constants a, b for ^{252}Cf isotope are 1.025 and 2.926, respectively[113].

A combinational geometry is designed in FLUKA for the detection setup. The absolute detection efficiency of the detector is calculated using the RESNUCLEi card. This card simulates the residual nuclei produced after the interaction of neutrons in the desired region. A total of 5 cycles of 10^6 histories were run for each configuration. A LOW-Mat card has been used for hydrogen in CH_2 bonds, ^{3}He and ^{10}B and ^{11}B in BF_3, it sets the correspondence between FLUKA materials and low-energy neutron cross-sections. For simulations, the detector was placed at the center of a room of size 6 x 8 x 6 m^3 with a concrete wall thickness of 20 cm. Simulations in the open air (without walls) have also been carried out to check the build-up in the neutron population that contributes to the absolute efficiency of the detector. The density and composition of concrete, polyethylene, and perspex were taken from the standard FLUKA material library.

3.3.5 Experimental validation of simulations

Monte Carlo simulations have been validated against experimental results for some cases using the Pu-Be source. Experimental data were taken with the geometry kept the same as that for the numerical simulation. A Pu-Be source of intensity 1±0.05x10^5neutron/s was placed at 100 cm from the surface of the detector to minimize the effect of source size on detection efficiency. The counting was carried out up to 10 seconds for the detector bank and up to 50 seconds for a single detector and background. The net counts were corrected for background in every case.

3.4 Studies on fissile material characterization using PF device

As described in section 1.5 of chapter 1, the pulsed neutron from the PF device can provide an advantage over other conventional sources for assay of fissile material in waste. In this work, the methodologies developed for the assay of fissile content of uranium in compressible laboratory waste and the industrial waste containing civil debris have also been included. Further, we have characterized the nuclear material in the waste generated in the fuel handling facilities.

3.4.1 Experimental set up for assay of low enriched uranium (LEU) in laboratory waste

A medium energy plasma focus device "MEPF-25" has been used for this application. The maximum neutron yield observed in this device is $(4.5 \pm 0.6) \times 10^8$ n/pulse. A well-type detection system having a cavity that can hold a 5-liter volume surrounded by ten ^{3}He detectors has been developed for delayed neutron counting. The schematic of the sample arrangement and the system geometry is shown in Fig. 3.7.

Based on AIDNEC (described in section 1.5 of chapter 1) methodology, feasibility studies have been carried out for the assay of fissile material in laboratory waste. The methodology was validated and tested for feasibility using a waste packet prepared by placing reference samples in compressible waste containing lab coats, gloves, and absorbent paper. The system performance was tested with enriched (14.8%) uranium oxide (U_3O_8) and metal samples. One waste packet consisting of a few gram of uranium distributed in the compressible material has also been prepared to check the effect of the matrix. The samples, as well as the waste packet, were placed in the cavity of the well detector, which is placed over the PF chamber as shown in Fig. 3.7.

3.4.1.1 Data acquisition

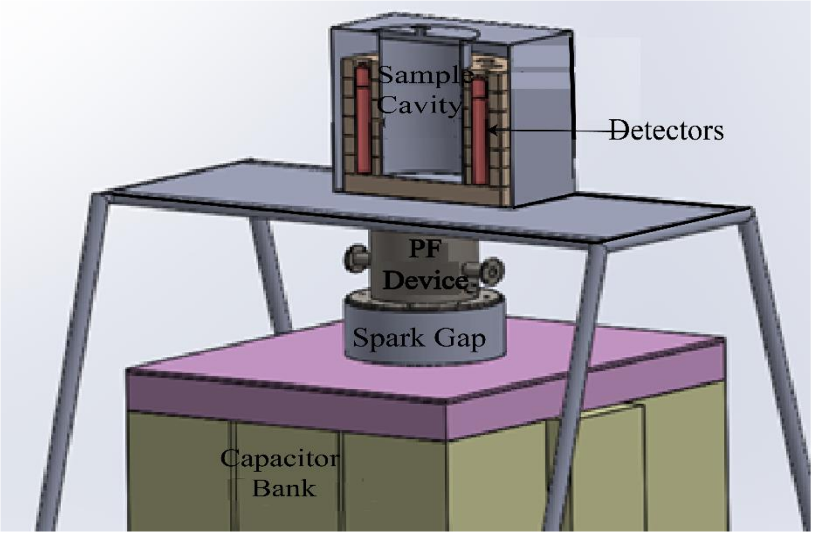

Fig. 3.7 The schematic of the AIDNEC system for the assay of enriched uranium in laboratory waste.

The block diagram of the data acquisition system is shown in Fig. 3.8. The neutron pulse from the ^{3}He detector bank is fed to the spectroscopy amplifier and the amplifier is connected to a multichannel analyser/ multichannel scalar (MCA/MCS). The delayed neutron activity was acquired in multi-channel scaling (MCS) mode with an input size of 2k channels and a dwell time of 50ms. The source neutron activity was monitored with an input size of 2k Channels and a dwell time of 1ms. To avoid the initial source neutron interference, the delayed neutron counts were acquired after a delay of 50ms from the start of the current pulse of PF device. Delayed neutron in all the detector modules (banks) was summed and accumulated for only 10 seconds to enhance the signal to background ratio as described in the subsequent section. These counts were further corrected for background and normalized to the average neutron yield of PF.

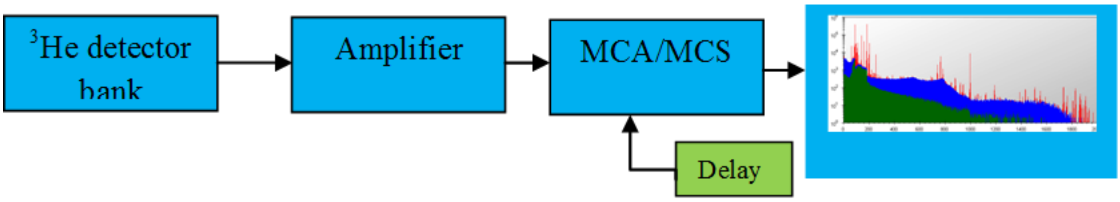

Fig. 3.8 The block diagram of data acquisition system for delayed neutron counting.

3.4.2 Assay of fissile material in industrial waste

The objective of this feasibility test is to evaluate the deployment perspective of the system for active assay of natural uranium in the civil and metallic waste produced in the fuel fabrication facilities. Different sample matrices could give a source of uncertainty due to the self-shielding of interrogating neutrons and self-absorption of the delayed neutrons. In this context, we have performed experiments on three samples in the form of soil and civil debris containing natural uranium using a deuterium gas-operated plasma focus device (2.45 MeV neutron source). The samples were labeled as sample-1 (processed uranyl cake), sample-2 (contaminated soils), and sample-3 (contaminated civil debris) with a net weight of 30 kg, 35 kg, and 40 kg, respectively. We have used thick PVC bags to prevent the spillage of the waste. To consider them as calibration standards for the active assay system, the exact fissile quantity in the samples is required, which has been estimated by other techniques i.e. gamma spectroscopy; the mass of natural uranium in these samples so found is 4147g, 2965g, and 74 g, respectively.

3.4.2.1 Monte Carlo simulations

To maximize the induced fission reaction in the sample and efficiently detect the delayed neutron from these fissions, the moderator placed in front of the detector needs to be optimized for thermalization of source neutrons as well as for delayed neutrons. Monte Carlo simulations have been carried out for the optimization of the moderator for the detector and sample. Simulations have also been carried out to evaluate the future perspective of using a D-T (deuterium-tritium) operated PF device for such applications. The simulation geometry shown in Fig.3.9 consisting of PF neutron source, sample (waste packets), and ^{3}He neutron detectors is the same as that used in the experiments.

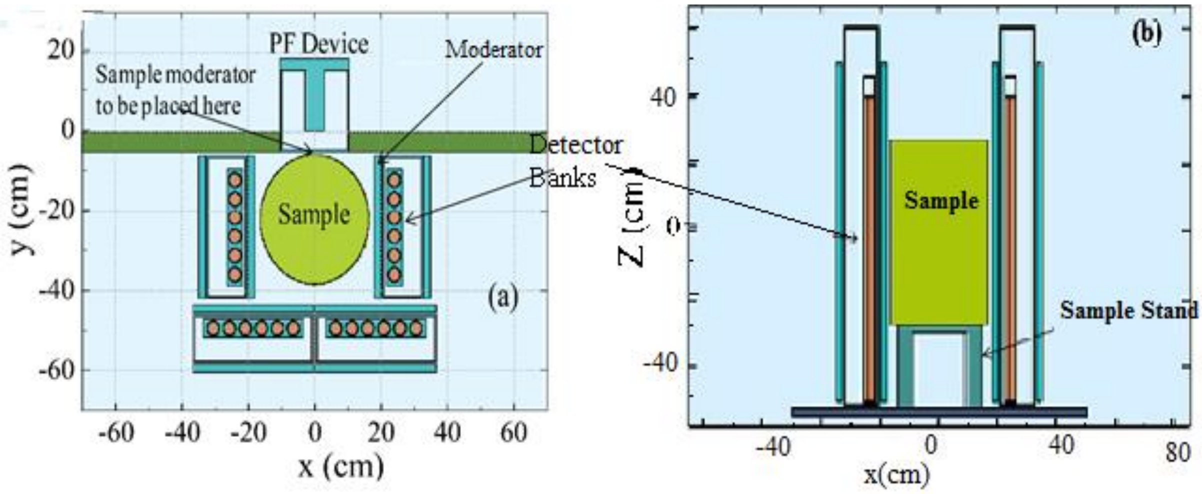

Fig. 3.9 The Sample irradiation and delayed neutron detection geometry used in experiments and in FLUKA simulations (a) x-y plane (b) x-z plane.

To check the requirement of the moderator to thermalize the source neutrons, we have simulated the number of fission reactions in the sample (sample 1) with varying thickness of sample moderator (polyethylene (PE)) without placing any detectors. Once the thickness of the sample moderator (polyethylene) was optimized all the detectors have been placed and the thickness of the detector moderator (perspex) to be placed in front of the detectors is optimized. The neutron fluence in the sample has also been simulated corresponding to the optimized moderator thickness.

We have used USRTRK, USRBIN, and SCORE cards in FLUKA for the determination of neutron fluence, fluence profile, and the number of fission reactions in the sample. The

USRTRK card simulates the track length estimate of the fluence in a given region specified in the input while the USRBIN card estimates the fluence profile in the specified area. The SCORE card estimates the required quantities (specified in the input) such as the number of fission reactions, photons, dose, energy deposition, etc. in different cell volumes. Further, the RESINUCLEIi card has been used to estimate the absolute efficiency of detectors for delayed neutrons. To estimate the delayed neutron counts as a result of induced fission, we have carried out the simulations in two stages; first for the number of induced fission reactions due to irradiation of sample by the pulsed neutron source using SCORE card and thereafter the detection of delayed neutrons from the sample using RESINUCLEi card.

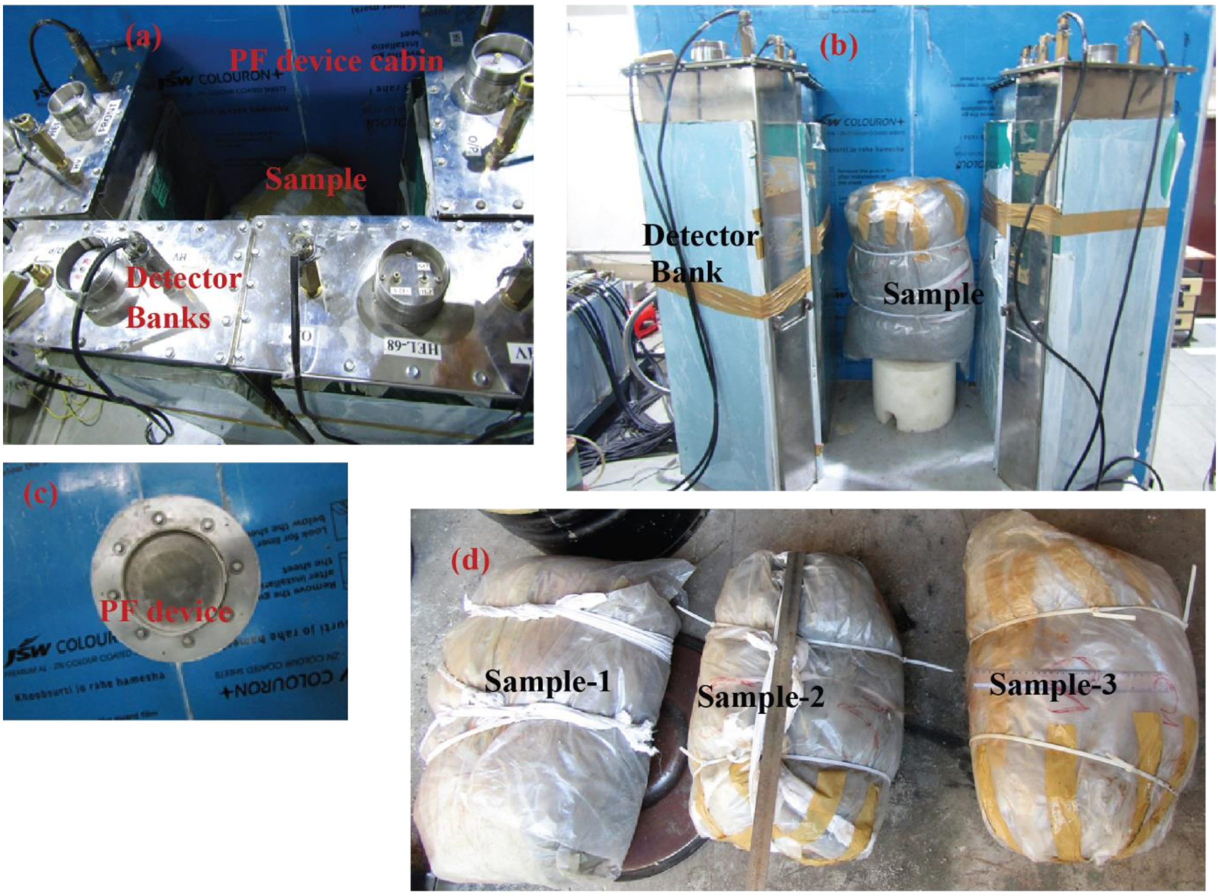

Fig. 3.10 Experimental geometry for sample irradiation and delayed neutron detection (a) top view (b) front view (c) the head of PF device coming out of cabin and (d) the sample pictures.

The delayed neutron energy has been taken from the literature[114] and used in the histogram profile of 27 bins. During the simulation of detector efficiency for delayed neutrons, the whole of the sample has been considered as a neutron source.

As will be described in a later chapter (chapter 5), the effect of the moderator placed in front of the sample in fission reactions has been observed to be very small, so samples were placed directly in front of the neutron source (PF Device). It has also been found that the 20 mm thickness of perspex is optimum for the moderation of delayed neutrons. Hence, for estimation of delayed neutron counts in all the samples the detector banks with 20 mm thick moderators have been used.

In simulations, the shape of the samples was approximated to be cylindrical. The average density of the sample material was estimated from the calculated cylindrical volume and known mass of the respective samples. The estimated average mass density of the three samples was 0.64g/cc, 1.3g/cc, and 0.84 g/cc, respectively. Since the samples were composed of natural uranium mixed with soil and civil debris (a mixture of pieces of concrete bricks and sand), so the sample composition in simulations has been considered concrete mixed with natural uranium. The height of each of the three cylindrical samples was taken to be 55 cm while the diameter is taken as 16.4 cm, 12.5 cm, and 16.7 cm, respectively.

3.4.2.2 Experimental setup for active assay of natural Uranium

The geometry of the experimental setup for active interrogation is similar to that shown in Fig. 3.10. The setup consists of a plasma focus (PF) pulsed fusion neutron source and neutron detector banks to detect source neutrons as well as delayed neutrons. The MEPF-17 has been used as a pulsed neutron source. Time integrated and time-resolved measurements of plasma focus neutron emission have been performed using a silver activation-based Geiger-Muller (GM) detector and plastic scintillator detector (PSD). Delayed neutrons from the activated samples have been monitored using four ^{3}He detector banks. The description of the ^{3}He detector bank and data acquisition system has already been provided in earlier sections.

3.4.2.3 Sample arrangement

Four^{3}He gas-filled proportional counter-based detector banks have been used to monitor delayed neutrons produced from induced fission of natural uranium contained in the samples (shown in Fig. 3.10c). Each detector bank consists of six numbers of 40 mm diameters × one-meter-long detectors, those connected in sum mode. The front and rear sides of the bank are covered using 20 mm thick perspex moderators and a 20 mm thick reflector for better efficiency of detection. The samples were placed outside the PF cabin as shown in Fig.3.10c. We have placed samples vertically along the length of detector banks. This arrangement provided maximum irradiation to sample with higher efficiency for the detection of delayed neutrons. Due to the large diameter of the sample, the source neutrons got thermalized in the sample itself, hence no source neutron moderator has been used.

CHAPTER 4

CHARACTERISATION OF SLOW CURRENT BASED X-PINCHES AND THEIR APPLICATION IN RADIOGRAPHY

This chapter presents the studies carried out on the development of X-pinches on a slow current driver. As described in section 2.1 of chapter 2, the X-pinch plasma undergoes a sequence of processes before a short burst of x-rays is emitted. Initially, when the current is driven through the wires, it explodes, and plasma starts to expand due to thermal pressure till the magnetic pressure due to current starts to overcome it. The current required to pinch the plasma depends upon the mass of the X-pinch. So for a given current driver having a certain peak current and rise time, the load parameters of the X-pinch are needed to be optimized. The point projection radiography application of X-pinch requires good quality x-rays in terms of yield, source size, and energy and the same can be obtained with an optimized load.

A study has been carried out to observe the effect of driver parameters such as current rate, the pinch current, and load parameters i.e. material, its thickness, etc. on the emitted x-ray properties. The analytical formulations discussed in chapter 2 have also been validated through the present study on slow current-driven X-pinch systems. After characterization and validation of analytical estimates, the X-pinch system has been utilized for the pulsed radiography of the exploding wire plasma. All these experimental studies are discussed in this chapter.

4.1 Evolution of X-pinch

The details of the current driver and configuration of the X-pinches have already been discussed in chapter 3. The characterization of the X-pinch system w.r.t various parameters is described in subsequent sections.

The evolution of X-pinch plasma, in general, is investigated using radiography and shadowgraphy methods [115, 116]. For example, the dynamics is studied in radiography methods by imaging an X-pinch at different instances using multiple x-pinches mounted parallelly [115]. Similarly, in shadowgraphy, the shadowgraph of the x-pinch at different instances is obtained by using pulsed laser beams [116]. However, in the present work, we have tried to understand the processes involved in X-pinches in light of the electric and optical signals obtained in the experiments before the characterization of the x-ray source. Various processes involved in the X-pinch discharge are marked in Fig. 4.1.

A typical waveform of current and PIN diode signals of the X-pinch is shown in Fig.4.1. In this shot, an X-pinch of 2×7.5 μm W wires has been studied in the charging voltage of 38 kV. As can be seen in the time profile of resistive voltage (Fig. 4.1b) and resistance (Fig. 4.1c) the initial phase of the X-pinch comprises wire-explosion, the formation of plasma followed by expansion of the plasma for a few hundred ns. The resistive voltage at wire explosion is peaked and decreases thereafter. Similarly, the resistance at the explosion is peaked, thereafter it is decreasing due to the formation and expansion of the plasma column as the magnetic pressure is insufficient to compress the mass. Once the magnetic field due to rising current becomes sufficient to compress (pinching phase) the plasma, the resistance of the plasma starts to increase (Fig. 4.1c) and shows a sudden rise at the time of x-rays emission. The sudden rise in the resistance shows the formation of instability (sausage) in the plasma column. Depending upon the seed of instability formed in this neck region (described in section 4.2.1), the plasma bifurcates or cascades in the column and leads to the formation of multiple hot spots. The instability formation corresponding to multiple hotspots can be seen in the voltage signals as multiple peaks depending upon the resolution. As the expansion velocity of the plasma column is different for different materials (Section 4.1.2), the number of hotspots and duration is different for different materials. After the emission of x-rays, the pinch plasma column disintegrates, and the voltage and resistance start to diminish. The pinch phase of the plasma is observed to be shorter (few tens of ns) and the current at the time of pinch and x-ray emission is practically more or less similar, so we have considered the current at the time of x-ray emission as the current required to pinch (I_P) the plasma column of given mass density. Since the x-ray parameters depend upon the pinch current, which itself depends upon the type of material (as discussed in chapter 2) and the size of the wire, therefore, it is worth to examine the behavior of the pinch current for X-pinches as a function of material type and sizes. The same has been discussed in the subsequent section.

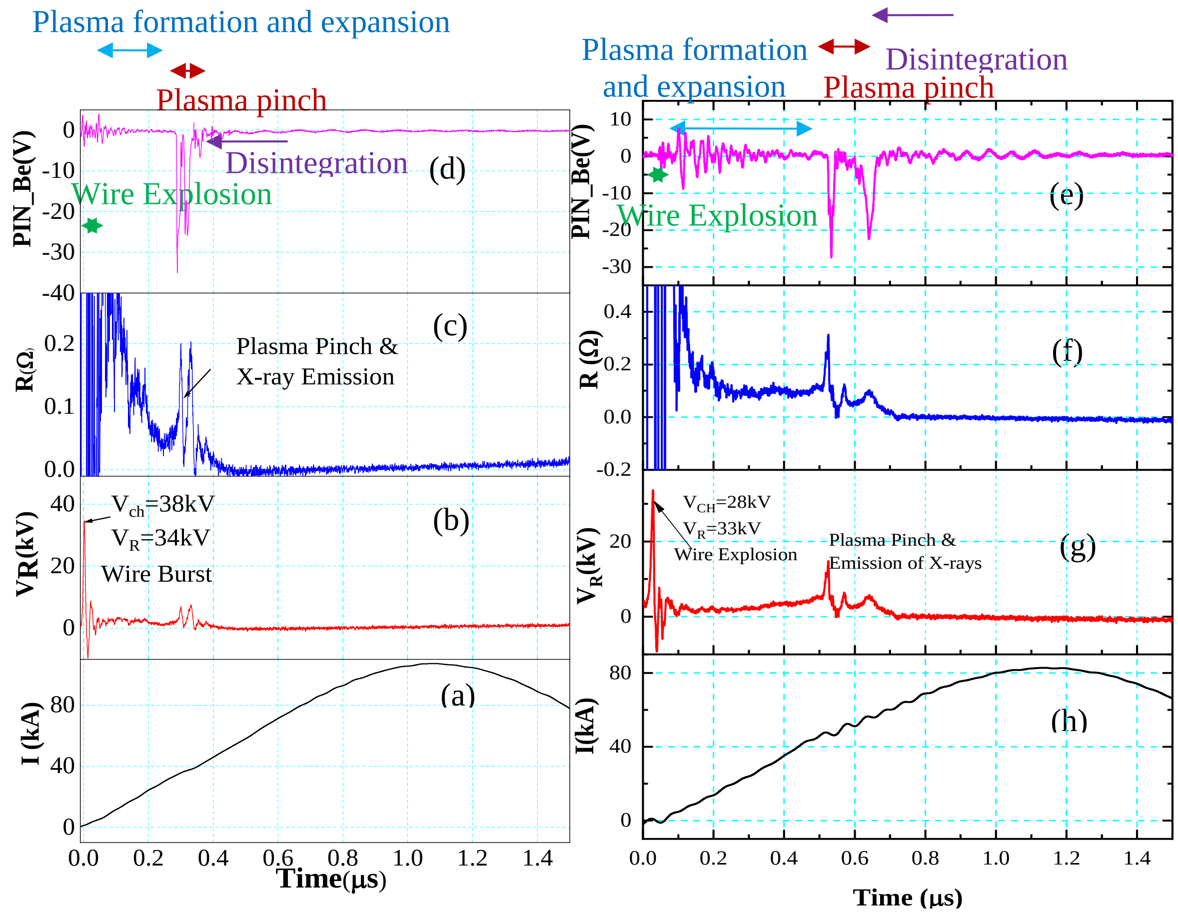

Fig. 4.1 (a, b, c, d) shows typical signals of current, resistive voltage, resistance and x-ray signals in 2×7.5 μm W X-pinch (e, f, g, h) signals in 2×15 μm Cu (coated with 2.5 μm polyamide) X-pinch.

4.1.1 X-pinches of two groups of metal wires

In the later years of 1950[117], the electrical explosion of wires (EEW) was classified into two groups namely, non-refractory (Cu, Al, Ag, and Au) and refractory (W, Mo, Fe, Pt, and Ni) according to their electrical explosions properties. The non-refractory metals are the ones having relatively low boiling temperatures and low heat of evaporation. During the electrical explosion, these metals exhibit a clear current pause, and the voltage across the discharge gap reaches to several-fold higher than the initial charging voltage[118]. During the initial phase of the explosion, these metals show high electrical conductivity. The refractory metals, however, have comparatively high boiling temperatures and high heat of evaporation. The current during the process of EEW of these metals never seizes to zero therefore, no clear current pause is observed. The voltage across the discharge gap in these metals never becomes higher than the initial voltage. The two groups mentioned above show different behavior due to differences in their thermo-physical properties upon electrical explosions. For example, the difference in plasma expansion velocity and resistivity may affect the x-ray parameters of the X-pinches. In addition to this, the atomic number 'Z' of the wire material may also influence the x-ray parameters. Apart from these two groups, one more group exhibiting properties intermediate to these such as follows like non-refractory in air and refractory in a vacuum, have also been studied by Romanova et al.[99] in past. However, as the X-pinches studied here are operated in vacuum conditions, we have restricted ourselves to only two groups.

The current and voltage signals of the one representative metal of each group (Cu for non-refractory and W from refractory) are shown in Fig. 4.1 (a,b,g and h). It may be noticed that in the case of non-refractory metal (Cu) the peak resistive voltage developed across the gap at the time of wire explosion (Fig. 4.1g) is higher than the charging voltage whereas, the same is lower than the charging voltage (Fig. 4.1 b) in the case of refractory metal (W). The distinct electrical and x-ray parameters of these two groups are discussed in detail in the subsequent sections.

4.1.2 Estimation of pinch current for two groups of wires

The pinch current for both the type of wires (refractory and non-refractory metals) is depicted in Fig.4.2. Although the experiments have been performed for various current rates ranging from 0.04 kA/ns to 0.11 kA/ns in refractory metals and ranging from 0.06kA/ns to 0.11kA/ns in non-refractory metals, the pinch current in the figure is plotted only for the case dI/dt~0.1kA/ns. In order to obtain higher mass density, we have studied the four-wire configuration of refractory metals in addition to two-wire configurations. It can be observed from Fig.4.2 that for refractory materials, the pinch current (I_P) varies linearly with the linear mass density of the X-pinch load as formulated in section 2.2 of chapter 2:

$$I_P{}^2 \propto m^2 \qquad (4.1)$$

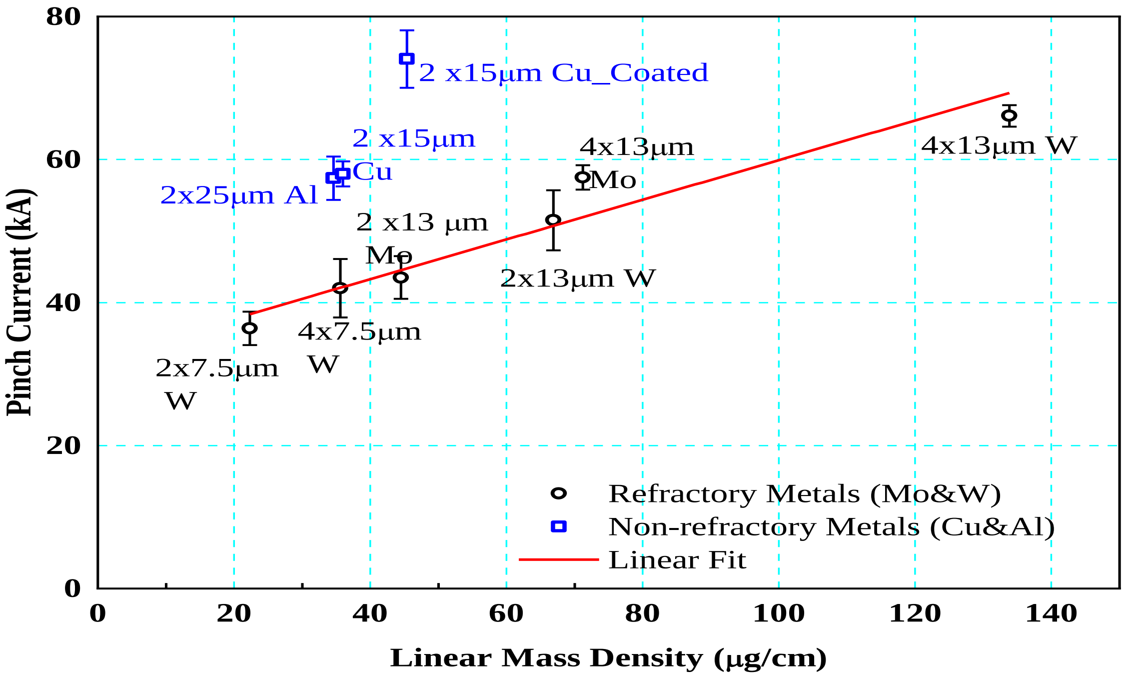

Fig. 4.2 The pinch current for various X-pinch loads of refractory and non-refractory metals.

The error bars in the pinch current are large in some cases, which could be due to some fluctuations in dI/dt during the experiment. The linear regression for the pinch current of refractory metals is estimated (linear fitting the data) to be I_p=31.4+0.26m. The R^2 for the linear fit is 0.98 and the error in both the parameters is <10%. The intercept of the line with the pinch current axis shows that the minimum current required for the compression of the X-pinch for the current driver having dI/dt of ~ 0.1 kA/ns is ~ 31.4kA. However, for the non-refractory metals Cu and Al, as the average pinch current is close to ~60kA even for much lower linear mass density of ~40µg/cm, so, we could not generate data as a function of linear mass density in these metals for the present range of current rates. Also due to similar reasons, we could not take up the four-wire configurations for study in these metals.

As can be seen in Fig. 4.2, though the linear mass density of the X-pinch made of 2×15 µm Cu, 2×25 µm Al, and 2 ×13 µm Mo is nearly the same, the pinch current for the Mo (refractory metal) differs significantly from those for first two metals i.e. non-refractory ones. Also, the scaling parameter (as expressed by Eq. 2.9) is significantly different for these two groups of metals. The difference in the pinch current observed in these two groups of wires could be due to the difference in their plasma expansion velocity. The average plasma radial expansion velocity at the neck can be approximated as $v = r(t_p)/t_p$ with r and t_p is the radius and the pinching time. The radial expansion velocity of the plasma jet at the neck was obtained by Jaar et.al.[119] in a microsecond current generator and they have observed that the average diameter of the plasma jet and its average radial expansion rate follows the inverse behavior with the atomic number (Z) of the X-pinch load. Further, the magnetic force in the plasma column of radius ‘r’ can be given by:

$$F_{mag} = -\frac{B^2}{2\mu} = \frac{\mu I^2}{8\pi^2 r^2(t_p)}, \qquad (4.2)$$

with I= I(t_p) is the pinch current. This equation in conjunction with the observations of Jaar et al. [3] suggests that relatively smaller magnetic force in Al X-pinch (due to low Z) as compared to Mo X-pinch of similar linear mass density delays the pinch process. This leads to a higher pinch current in the former configuration. However, for Cu-X-pinch, the Z-value is somewhat higher than that for Al but it is much smaller than that for Mo making the pinch current fall near the Al. It may be noted that apart from the expansion velocity, the inertial component (thermal pressure) of the X-pinch load also influences the plasma compression.

4.1.3 Effect of dI/dt on pinch current

The effect of rate of rise of current (dI/dt) on pinch current has been studied for the dI/dt ranging from 0.06-0.11 kA/ns for non-refractory and 0.04-0.11 kA/ns for the refractory metals.

The dependence of the pinch current on dI/dt is shown in Fig. 4.3. For non-refractory

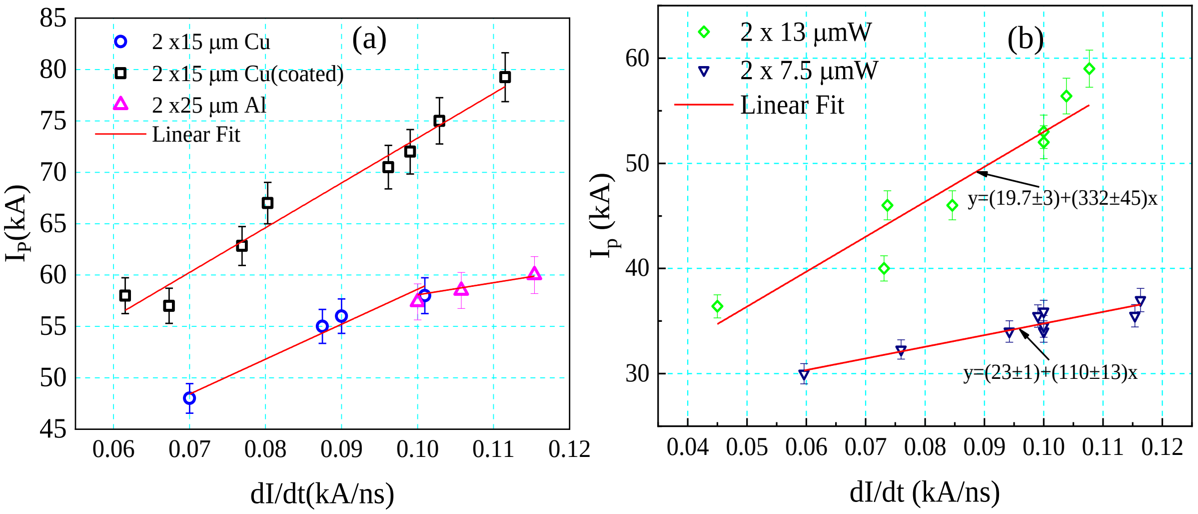

Fig. 4.3 Dependence of Pinch current on dI/dt for (a) non refractory and (b) refractory metal wire X-pinches

metal Cu and Al (Fig.4.3a), as the dI/dt of the driver increases the pinch current through the X-pinch load also increases and this increase is linear as a function of dI/dt. The linear increase in the pinch current with the current rate of the driver could be attributed to the shunting of current at higher dI/dt. Faster is the current flown through the wires lesser is the energy deposited into it as most of the current is shunted through the corona formed surrounding the wire. This low energy deposition into the core delays the plasma compression. The low energy deposition in the wire core can be prevented by the use of dielectric coating as described in the subsequent section. In Fig. 4.3(b) the variation of the same with dI/dt (ranging from 0.04 kA/ns -0.12 kA/ns) is shown for refractory metals. We have not shown results of Mo as most of the shots in that metal were taken near 0.1kA.ns. Like that for non-refractory metals, the pinch current with increasing dI/dt in W metal, in general, also shows an increasing behavior for this range of dI/dt. Additionally as discussed in section 4.1.2, being proportional to the mass density of the load, pinch current of X-pinch of 7.5 µm diameter W is observed to be lower than higher mass configuration i.e. 2×13 µm W for all dI/dt.

4.1.4 The effect of dielectric coating

To look into the effect of the dielectric coating of wires on x-ray properties, we have compared the results of X-pinches of bare wire and wires with 2.5 µm thick dielectric coating on 15µm Cu wires. It is apparent from Fig. 4.3, the pinch current of the bare Cu wire X-pinch is comparatively lower than that of the coated Cu wires with equivalent driver parameters, i.e. dI/dt. The lower current in the bare wire is due to the creation of coronal plasma around the wire. The resistance of this plasma is relatively smaller than the resistance of the heated core, with much of the current being driven through the plasma and less current available for further heating of the core. A few micron thick dielectric coating delays this current change and prolongs the resistive heating process, which leads to the development of higher resistive voltages across the gap and more energy deposition in the wire. Relatively higher energy deposition in the coated wires leads to a higher expansion rate of the plasma. According to Eq. 4.2, the higher expansion rate of plasma would lead to the requirement of more pinch current to have sufficient magnetic force to cause the compression of the plasma, hence delaying the compression of the plasma column in the neck area. The higher pinch current results in the emission of a comparatively higher yield of x-rays. Due to higher x-ray yield, we have considered Cu wires with insulating coating for further applications.

4.1.5 Dependence of soft x-ray yield on pinch current

The dependence of soft x-ray yield on the current available at the time of pinch (I_P) is displayed in Fig. 4.4. Fig. 4.4(a) displays the yield as a function of pinch current for non-refractory metal Cu and Fig. 4.4(b) represents the same for refractory metals. We have not shown here the x-ray yield from the four-wire configuration due to the limited number of shots, which were taken at dI/dt of ~0.1 kA/ns. As can be inferred from these figures, in general, the x-ray yield increases with increasing pinch current for all metals and the increase is approximate as $\sim I^{34/9}$ with the pinch current which is consistent with the expression described in section 2.4. The fitting parameters for pinch current with dI/dt and x-ray yield to the pinch current in 2 ×15 µm Cu (for both coated and bare wire) are listed in Table 4.1. Moreover, the pinch current for the metal Cu is higher than that for the refractory metal W, corresponding to the same yield of x-rays.

As far as the value of x-ray yield is concerned it is highest for the 2×13 µm W among refractory metals and for 2×15 µm Cu among non-refractory metals (for the present range of dI/dt considered in the study). However, Cu X-pinch with dielectric coating resulted into a higher x-ray yield than the bare wire Cu. It indicates that the mass density of 2×13 µm W and 2×15 µm Cu coated are the optimum masses for the current driver with similar parameters. Furthermore, it was also be noticed that the x-ray yield for these two configurations is nearly the same. Among three configurations of refractory ones shown in Fig. 4.4b, the low x-ray yield in the 2×13 µm Mo is attributed to its low Z as compared to W.

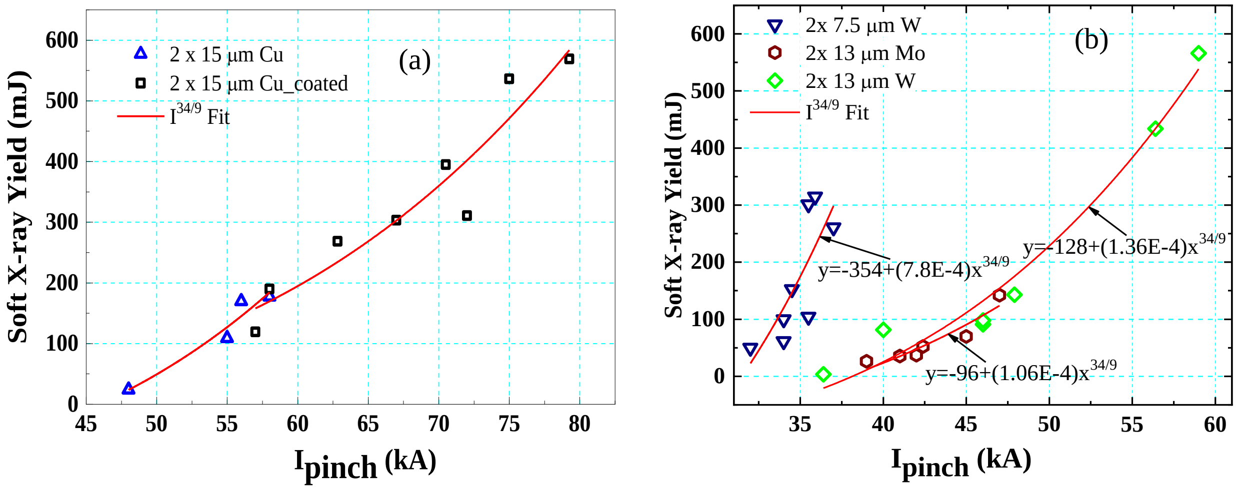

Fig. 4.4 Dependence of soft x-ray yield (>1.5 keV) on pinch current of (a) 2×15µm Cu (coated and bare), and (b) same for refractory metals with their pinch current.

Table 4.1. Fitting parameters of dI/dt vs I_p and I_p vs SXR in 2×15 µmCu X-pinches (Fig. 4.4).

dI/dt-Ip relation (y=a+bx)			Ip-SXR relation $y=a+b*x^{34/9}$	
2x15µm Cu		2x15µm Cu_Coated	2x15µm Cu	2x15µm Cu_Coated
a	24.6±3	29.75±3	-130±48	-14±10
b	340±42	435±35	6.85E-05	4E-05
R	0.95	0.95	0.90	0.88

4.2 Characterization of X-pinch sources

4.2.1 Time profile of x-rays

The typical time profile of x-rays from the X-pinch (4×7.5 µm W) is shown in Fig. 4.5. For dI/dt of ~0.1 kA/ns, the average time of emission of the first burst of x-rays for various X-pinch configurations is listed in Table 4.2. It is in the range of 266 ns to 575 ns with maximum jitter of 40 ns, which is small as compared to those (few hundreds of ns)reported for slow current-driven systems[74, 76].

As can be seen in Fig. 4.5, the x-rays are observed to be emitted in multiple (typically 2-5) x-ray bursts. In general, these x-ray bursts are emitted in two bunches (marked as I and II) separated by few tens of ns. The first bunch (marked as I) of x-rays has small pulse width (~3-10 ns) while the second one is of relatively larger width. The emission of the first bunch of the x-rays could be due to the hotspot formed at the neck of the X-pinch. As the current through the Z-pinch channel continues to flow with more or less the same or slightly increasing level, the column is expected to result in secondary pinches. This possibly explains the emission of multiple x-ray bursts. The emission time for these x-ray bursts is of the order of ns or subnanosecond, but due to the slow response of PIN diodes, the pulse width has been observed in nanoseconds. The pulse width of the second set of bursts (marked as II) is observed to be a few tens of ns. The origin of these bursts could be due to the movement of hot electrons or ion beam towards respective electrodes, it has been confirmed from the time resolved imaging studies of the x-ray source carried out in the past[120, 121].

Table 4.2 The average time of emission of the first burst of the x-rays in various X-pinch configurations for dI/dt of ~0.1kA/ns.

XP configuration	Time of first burst (ns)	Error (ns)
2 x 15 Cu (coated)	561.0	14
2 x 25 Al	442.0	28
2x 15 Cu	509.0	25
2x 7.5 W	280	14
2 x 13 Mo	386.0	41
4x 7.5 W	309.0	20
2 x 13 W	418.0	40
4 x 13 Mo	433.0	10
4 x13 µm W	451.0	9

The number of x-ray bursts in X-pinches is also an important parameter for its application in point projection radiography. Though, as depicted in Fig. 4.4 for the same current rate of ~ 0.1kA/ns, the x-ray yield in 2×13µm W and 2×15µm Cu (coated) is nearly the same but the number of bursts in the former configuration is comparatively less than that for later one. A frequency spectrum of the number of x-ray bursts for these two configurations is shown in Fig. 4.6.

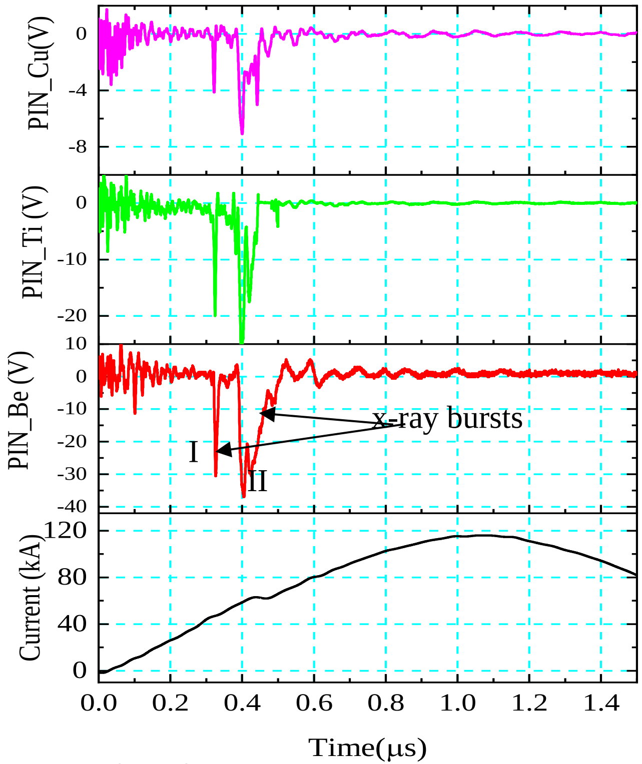

Fig. 4.5 Typical time profile of x-rays observed in X-pinch shot (4×7.5 µm W) in PIN diodes coupled with different filters (50 µm Be, 12.5 µm Ti and 25 µm Cu).

Furthermore, the reason for the x-ray hotspot formation in the central region of the X-pinch is due to sausage instabilities, which itself is highly sensitive to experimental perturbations (such as defects, current distribution in plasma, etc), thus leading to large shot to shot variation in the number of x-ray bursts and the x-ray yield. These variations can be minimized by reducing load nonuniformities (such as wire thickness or coating variations) and current variations. However, as theoretically formulated by Chittenden et. Al[97], the cascading in the neck region depends upon its length, which is directly proportional to the expansion velocity of the plasma. In the case of Cu X-pinch, owing to a greater expansion velocity, the length of the neck is comparatively higher than that for the W wires, which leads to a more number of x-ray bursts due to a much larger length of the neck. The frequency spectrum of the number of bursts for other configurations (two-wire configurations of 15 μm Cu, 13 μm Mo and 7.5 μm W) is also shown in Fig 4.6. The effect of mass density, Z, and the pinch current described for the case of 2×13μm W and 2×15μm Cu (coated) seems to decide the number of bursts in these configurations.

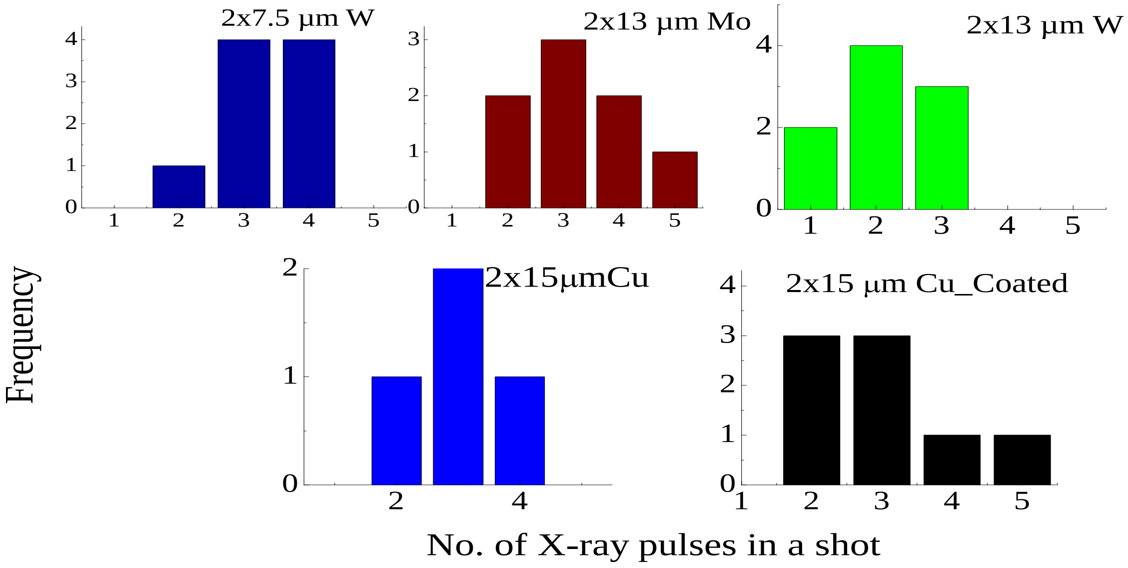

Fig. 4.6 Number of x-ray busts in a shot for two wire configurations of X-pinches.

4.2.2 Measurement of x-ray energy and yield

The energy of the x-rays has been measured using thin foil filters of different metals as described in chapter 3. These foils cover the energy range from 1.5 keV to 10keV. The x-ray yield in the two-wire configuration of non-refractory metal (Al and Cu) X-pinches (for whole the range of dI/dt) with different x-ray filters is shown in Fig 4.7. It shows that the x-ray is emitted in the softer energy region (<5keV). Since the pinch current is one of the deciding factors for the x-ray yield depending on the driver dI/dt, there is a major shot-to-shot variation in yield that has been observed. The higher energy (>6keV) yield is observed to be quite small as a very small yield has been observed in PIN diodes filtered with Cu. As described in section 4.1.5, a few micron thick coating of polyamide is observed to enhance the soft x-ray yield. The x-ray yield in Al X-pinches is observed to be smaller than that for the Cu (Fig. 4.7c). Further, no appreciable x-rays have been detected in the Cu filtered PIN diodes for the Al X-pinches indicating that the emitted x-rays energy ranges only up to 5 keV. The low yield and low energy x-rays in the case of Al are attributed to low Z.

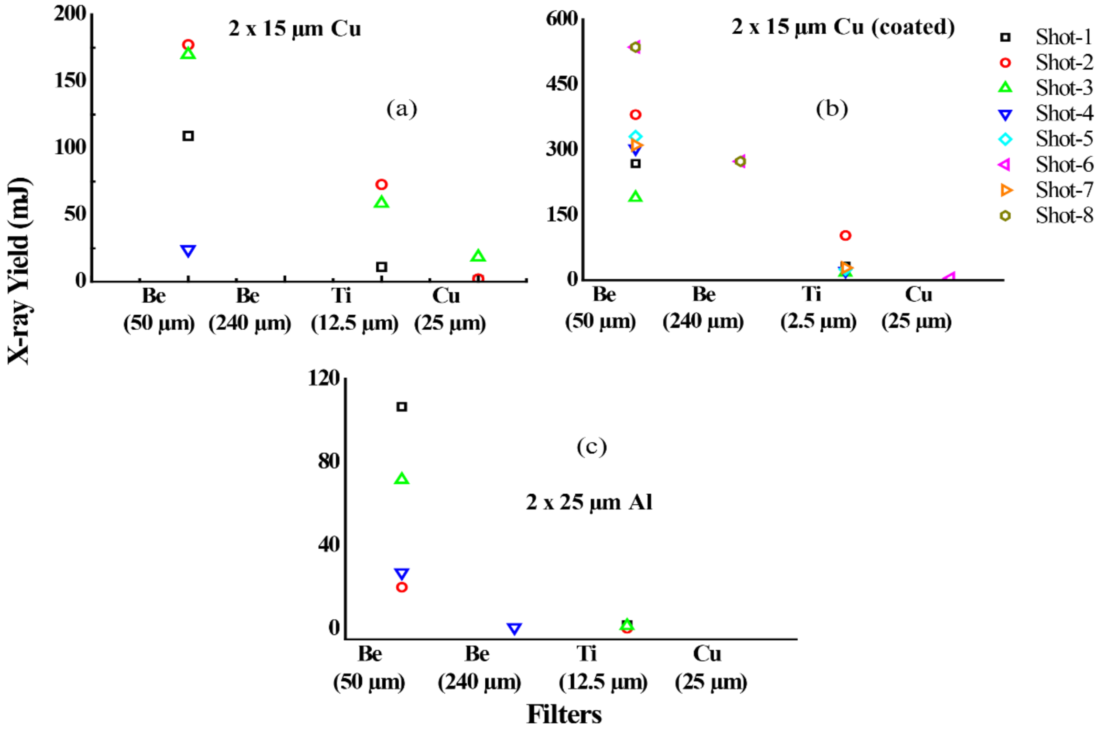

Fig. 4.7 The x-ray yield through different filters in two wire configuration of X-pinches of Non-refractory metals Cu and Al. The shot to shot variation in x-ray yield for a given energy is due todifference in dI/dt for different shots.

The yield observed through different filters in X-pinches of refractory metals (Mo and W) of two and four-wire configurations are shown in Fig.4.8. The x-ray yield observed in refractory metals is comparatively higher as compared to that for non-refractory metals Cu and Al, despite a lower pinch current. A quantitative study for the dependence of x-ray yield on pinch current and the Z is discussed later in this section. Further, it may be noted that the yield for 2×13µmW (Fig. 4.8c) is comparable to that for 2 ×15µm coated Cu (Fig. 4.7b). The higher energy component (>6 keV) in these metals is also observed to be similar. Despite being of the lower mass density and pinch current the higher x-ray yield for the 2×7.5 µm W as compared to that for the 2×13µm Mo is attributed to higher Z of W. In 4 × 7.5 µm W, the x-ray yield is observed to be higher than its two-wire configuration due to higher mass density and higher pinch current.

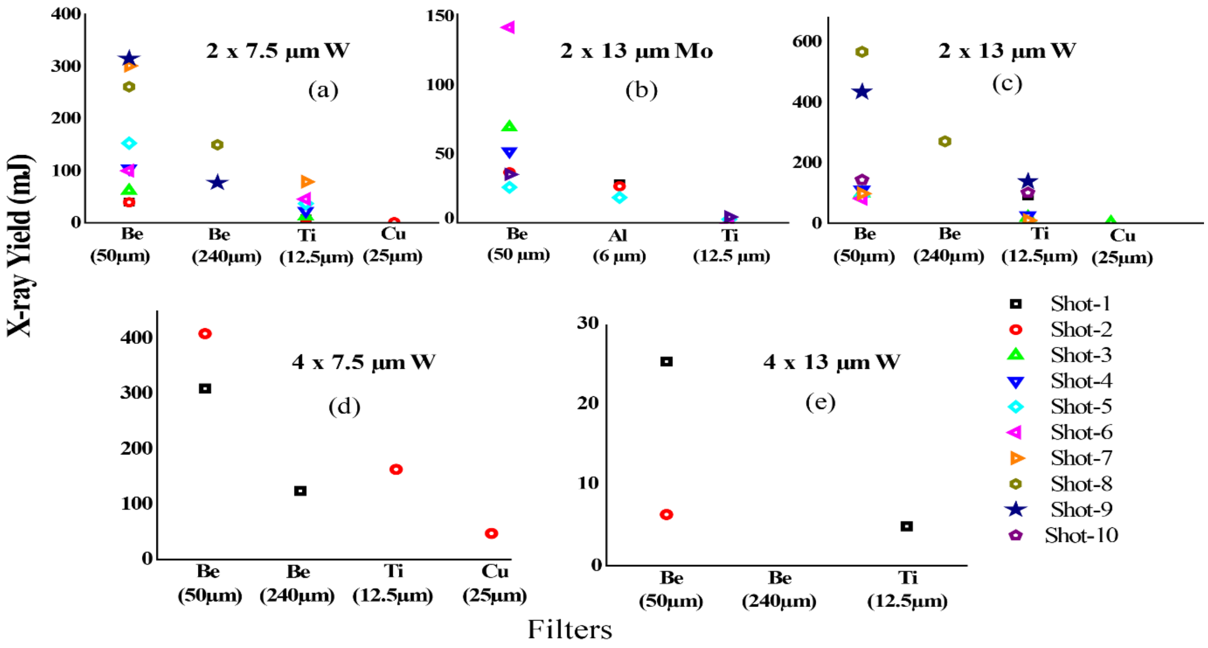

Fig. 4.8The x-ray yield in X-pinches made of refractory metals. The shot to shot variation in x-ray yield for a given energy is due to difference in dI/dt for different shots.

Table 4.3Scaling of soft x-ray yield for different X-pinch configurations.

Linear Mass density(μg/cm)	X-pinch config.	Average I_p (kA)	Product $I_p^{34/9}Z^{14/9}$	Ratio w.r.t Cu	Estimated yield w.r.t. Cu (mJ)	Experimentally observed Max. Yield (mJ)
45.4	2 × 15 Cu (coated)	69.3	1.7E+09	1.00	570	570
34.6	2 × 25 μm Al	57.4	2.4E+08	0.14	80	106
36.6	2×15 μm Cu	56.3	7.7E+08	0.45	257	177
22.3	2× 7.5 μm W	36.4	6.4E+08	0.38	213	314
35.6	2 × 13 μm Mo	42.0	4.5E+08	0.27	152	142
44.5	4 × 7.5 μm W	43.5	1.3E+09	0.74	418	409
66.9	2 × 13 μm W	46.6	1.6E+09	0.96	543	566
133.8	4 × 13 μm W	66.1	6.1E+09	3.59	2033	25

According to the expression for the x-ray power provided in section 2.2 of chapter 2, it has a stronger dependence on pinch current through the X-pinch load as compared to that on Z of the material. Using the relation of Eq.2.20 and experimentally obtained pinch current, a ratio of x-ray power obtained for various configurations with respect to the configuration of maximum x-ray yield has been calculated. In the ratio, the common dependence of other factors of the driver such as dI/dt cancels out. The yield so obtained for various configurations with respect to 2×15 μm coated Cu X-pinch (maximum x-ray yield configuration) has been compared with the experimental yield (Table 4.3). For most of the configuration, the x-ray yield (scaled w.r.t. Cu) estimated as per Eq. 2.20 agrees with the maximum yield observed in the experiments within ~31%, however, for one case i.e. for 2× 7.5 μm W, the difference is ~47%.In the 4×13 μm W configuration, the experimentally observed x-ray yield is not consistent with the scaled value (Table 4.3) as the pinch current is not sufficient to efficiently compress the higher linear mass density of the plasma column, hence a low yield of x-rays as compared to scaled values, has been observed. Further, it is evident from Table 4.3 that the mass corresponding to the maximum yield is the optimum mass for the current driver under study (~0.1kA/ns).

4.2.3 Comparison of yield from two and four-wire configuration

The x-ray yield observed in the four-wire configuration of W wires is shown in Fig. 4.8d and 4.8e. In 4×7.5 µm W, the x-ray yield is observed to be higher than its two-wire configuration. This enhanced yield could be due to efficient magnetic compression of a higher mass density (four-wire configuration) plasma, which is close to the optimum mass. Furthermore, in 4 ×13µm W, the yield is observed to be very small as compared to its two-wire configuration which may be due to the mass density much higher than the optimum mass for this configuration leading to inefficient compression of plasma column at pinch current of 66kA at the current rate of 0.1kA.

To compare the x-ray yield of two-wire and four-wire X-pinches of similar mass density, we have taken few trials of 2 ×25 µm Mo (m=132 µg/cm)X-pinches at maximum dI/dt. Although the mass density of this configuration is similar to 4 ×13 µm W, the former didn’t result in the emission of x-rays. As the current through the individual wire of four-wire configuration is lower in comparison to two-wire configuration, which leads to comparatively lower plasma expansion velocity. The smaller diameter plasma column due to a lower expansion rate provides a comparatively higher magnetic force that resulted in the emission of x-rays in the four-wire configuration as compared to two wires.

4.2.4 Measurement of x-ray source size

The time-integrated source size of the X-pinches has been measured using time-integrated pinholes, multi-pinhole, slit wire, and radiography methods.

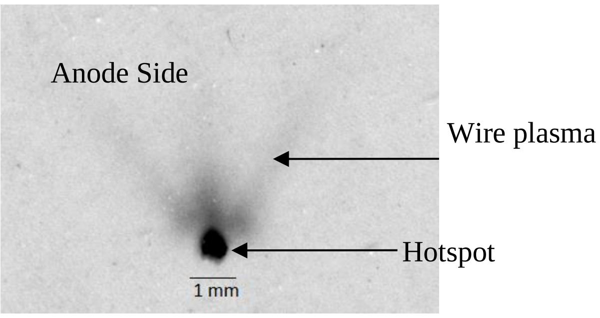

Fig. 4.9 (a) Image of hotspot from W X-pinch with 300 µm pinhole and 6 µm Al filter. The cut off energy of filter is 1 keV.

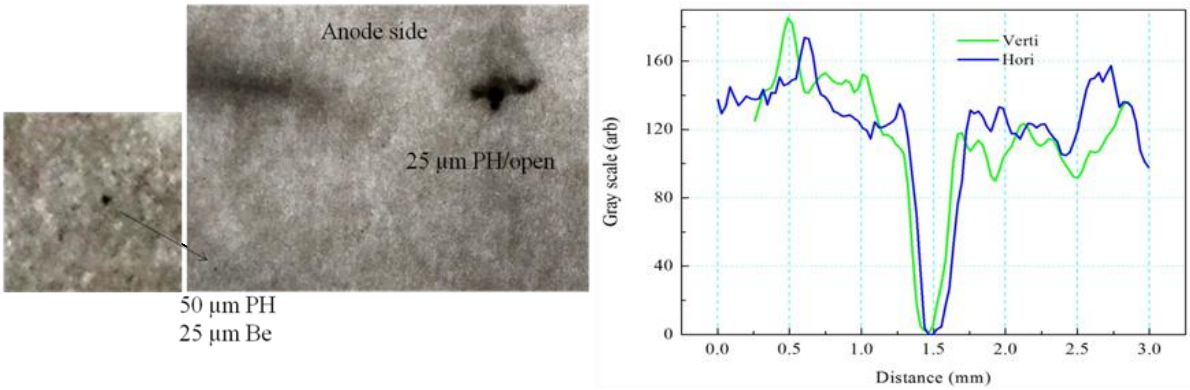

Fig. 4.9 (b) Multi-pinhole image and line profile of 2 ×7.5 µm W X-pinch, the source size is estimated to be 40 µm.

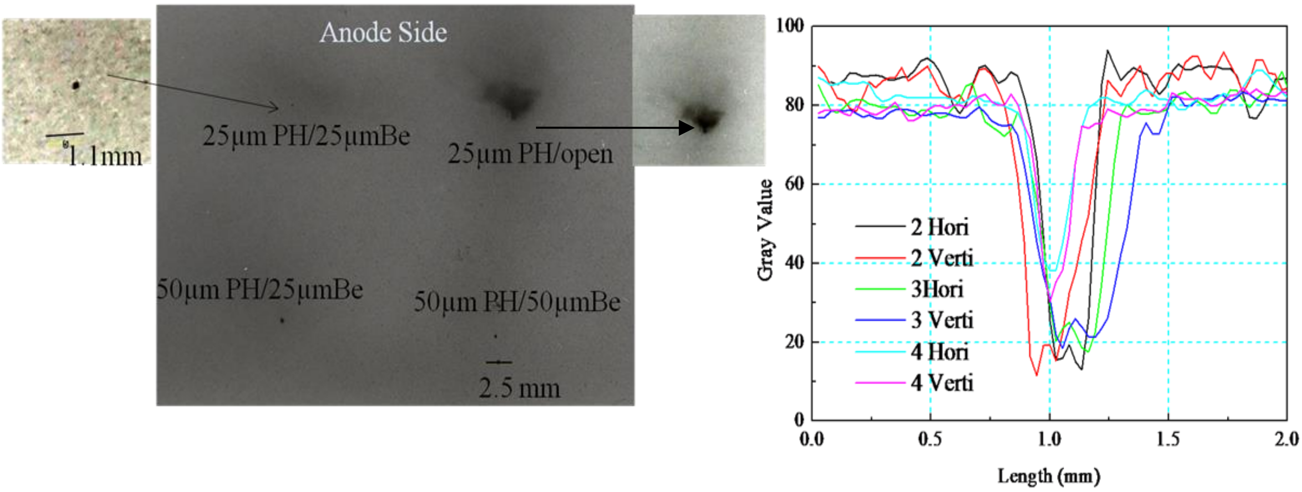

Fig. 4.9(c) Multi-pinhole images and line profile of 4 ×7.5 µm W X-pinch, the length and width of the hotspot found through smallest pinhole is estimated to be 15 and 23 µm.

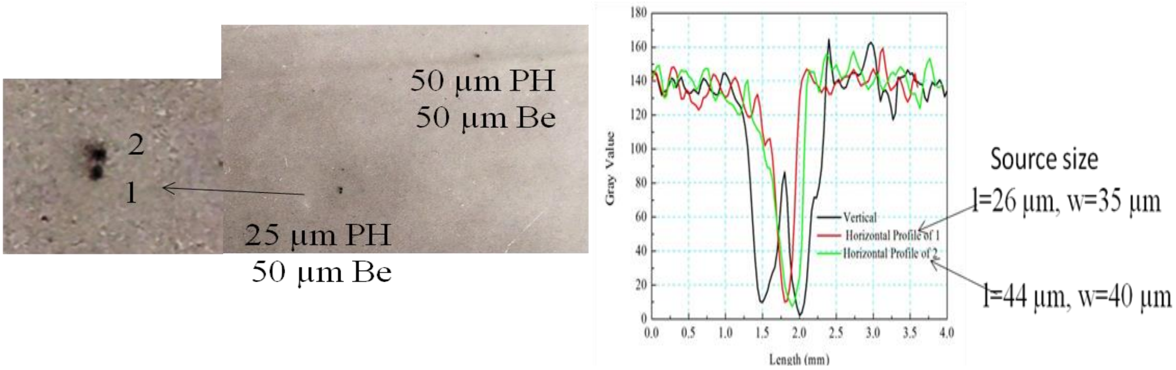

Fig. 4.9 (d) Multi-pinhole image and line profile of 2 ×15 μm Cu X-pinch

The pinhole images of the various X-pinches are shown in Fig. 4.9. A time-integrated image of the hot spot formed in 2 ×13 μm W X-pinch obtained with 300 μm pinhole and Al (6μm) foil filters is shown in Fig.4.9a. A weaker limb of x-rays has been observed towards the anode side while no emission is seen towards the cathode. The x-ray from the wire plasma can also be seen in the image. As the pinhole size was much larger than the radiation source, the penumbra of the source can provide an estimate of the source size, however, in the cases of the formation of multiple sources, the penumbral image provides an overlapped image of these sources. As the Si-PIN diode signals show multiple pulses, so the pinhole image (of hotspot shown in Fig. 4.9a) of the source could be an overlapped image of multiple hotspots and x-rays from hot electrons.

To investigate the number of hot spots and their sizes, we have utilized a time-integrated multi-pinhole camera coupled with different filters. The location and size of the multi-pinholes are provided in section 3.1.5 of chapter 3. To look into the soft x-rays emitted from wire plasma and the hot spots, one of the pinholes of a multi-pinhole was taken without the filter. The diffraction limit allows the pinhole to transmit the x-rays above ~200eV. The wire limbs towards the anode side were observed in the image(Fig. 4.9b and 4.9c), however, no x-rays have been observed towards the cathode side. The energy information of the hotspots has been observed with filtered pinhole images. In the image of the 2 ×7.5 μm W (Fig. 4.9b), the source size obtained with 50 μm pinhole with 25 μm Be filter is ~40 μm. The x-ray spots of higher energy have not been formed as indicated by the absence of image in pinhole of larger diameter and higher filter thickness (12.5 μm Ti or 25 μm Cu). The geometrical blurring due to pinhole diameter has been seen in one of the shots of 4 ×7.5 μm W. The source size in 4 ×7.5 μm W having 39 kA pinch current is obtained to be 15 μm. The size of this source was also confirmed in the image from the open pinhole. The emission due to wire plasma is also visible in the open pinhole image (Fig. 4.9c). The multiple hotspots were also observed in few trials, an image of hotspots obtained in one of such trials is shown in Fig. 4.9d for 2 ×15 μm Cu(coated) X-pinch. In this image, the separation of the two hotspots is found to be ~60 μm. The first source (marked as 1) could be due to hotspot formation in the neck region and the other (marked as 2) could be due to hot electrons movement across the mini diode. The width and length are estimated to be~ 34 μm and 55 μm for source 1 and 35 μm and 62 μm for source 2. The source size could be even smaller as the geometrical broadening in the pinhole is comparable to the obtained source size.

In the pinhole images, observed x-ray sources are the convolution of multiple hot spots due to geometrical blurring described in section 3.1.5 of chapter 3. In such cases, the upper limit of the spot size decides the blurring in the image of the projection radiography which has been estimated using a slit wire camera. Typical images observed using this camera from a W wire-based X-pinch are shown in Fig. 4.10. The line profile of the individual wire is also plotted and placed above its image. These line profiles have been shown to visualize the diameter of the wire, which can be estimated by using the expression $t=a/m$, with '*a*' being the full width of shadow at 90% intensity.

Two shadows of the slit (marked ‘1’ and ‘2’) have been observed in the image with an intense; ‘1’ in which up to 25 µm wire is visible, and a shallow; ‘2’ in which no explicit image of W wires is seen. The intense shadow ‘1’ of the slit is due to x-rays from the hotspot and it indicates the upper limit on its size to be 25 µm, as wire of this size is visible. It could even be lower than 25 µm as the image of 13 µm W wire in the intense shadow ‘1’ of the slit is partially visible, as its line profile shows a larger peak in conjunction with smaller ones. The noise in this image could be due to the imperfection in the industrial film used and the scanning procedure (which for present purposes did not utilize film digitizer).

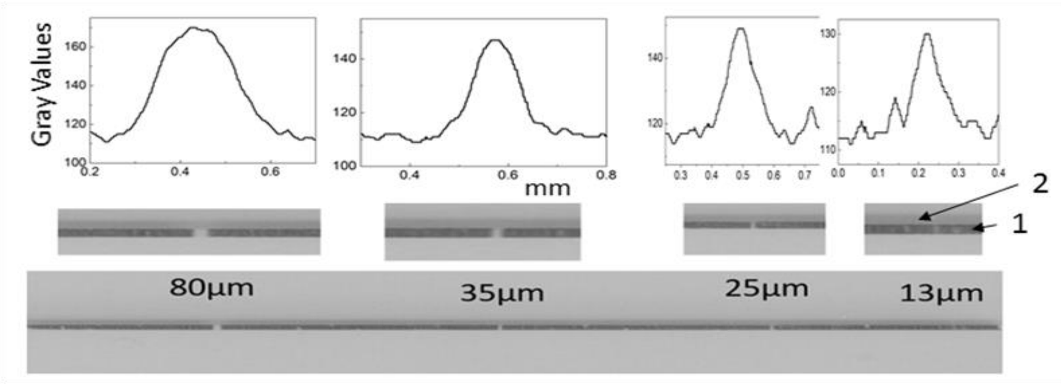

Fig. 4.10. The Slit Wire camera image from W X-pinch(bottom) with enlarged view (middle) of shadow of each wire and corresponding line profile (top).

The second shadow ‘2’ of the slit is shallow and wide, with even the image of the wire of 80 µm diameter not recognizable indicating that a broad source is responsible for this shadow. The origin of this (wider) source could be from the x-ray generated from hot electrons.

The x-ray source size has also been estimated using the radiography method. For this purpose, a wire mesh was placed at 200 mm from the source with the same magnification (m=2.3) as for the slit wire camera. The radiograph so obtained with Mo X-pinch is shown in Fig. 4.11. All the wires in the mesh are visible and shadows of wire suggest the presence of two sources (one intense and one faded marked as ‘1’ and ‘2’ in the figure) that seem to be separated in the vertical direction. To look into wire sizes line profile along the horizontal direction is also plotted and shown below the radiograph (Fig. 4.11c). The penumbra of the radiographic image has been used to estimate the source size. The source size 's' from the line profile of the radiograph has also been estimated to be ~23μm using the relation s~d/m where d is the width of the penumbra. We have considered 10-90% width of the penumbra from the standard definition of the width of the step.

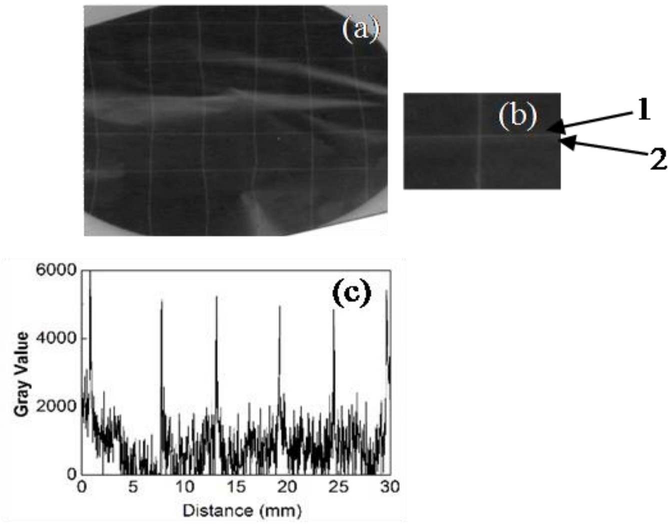

Fig. 4.11(a)Radiograph of 35 μm W wire mesh obtained with Mo X-pinch. (b) Enlarged view of wire mesh (c) The line profile of wire shadows in horizontal directions.

The minimum source sizes obtained with different methods of the X-pinches and their corresponding pinch current are listed in Table 4.4. As described in section 2.4 of chapter 2, the minimum radius achieved in the X-pinches scales as $r \sim I_p^{-14/9} Z^{-10/9}$ i.e. decreases with higher I_p and Z. This scaling suggests that the source size for 2 x 15μm Cu (coated) X-pinch with an average pinch current of 69.3 kA (Fig. 4.9d) would be 1.5 times that for W (I_p=46.6kA). Similarly, for 2 x 13 μm, Mo X-pinches with an average pinch current of 42 kA the spot size would be 2 times that for W in the same configuration.

The source size of apparently similar (in terms of x-ray yield) W and Cu (coated) pinches, has been obtained to be 13µm and 26µm, respectively. The smaller source size and less number of x-ray bursts for 2×13µm W metal suggest that W is a better choice to be used in X-pinches.

Table 4.4 Scaling of source size for different X-pinch configuration

Linear mass density (µg/cm)	X-pinch Config.	I_p (kA)	$I^{-14/9}Z^{-10/9}$	Estimated size w.r.t. 2 × 13 µmW (µm)	Observed size (µm)
22.3	2x 7.5 W	36.4	3.12E-05	19	40
35.6	2 x 13 Mo	44.7	4.26E-05	26	23
44.5	4x 7.5 W	39	2.81E-05	17	15
45.4	2 x 15 Cu (coated)	69.2	3.26E-05	20	26
66.9	2 x 13 W	46.6	2.13E-05	13	13

4.2.5 Estimation of electron temperature of the hot spot

In an X-pinch, the x-rays are first emitted from the hotspot followed by emission through other processes such as electron beam and plasma jets. The energy of x-rays emitted in the first few bursts is in a softer region, as the ratio of the first burst through two filters (Be and Ti) is comparatively smaller. The electron temperature of the hotspot corresponding to the first x-ray burst for different X-pinch configurations for dI/dt of 0.1kA/ns is shown (Fig. 4.12). There error bars shown in the figure correspond to the range of the temperature estimated experimentally. The temperatures in the X-pinch made of Cu, Mo, and W wire have been estimated in the range of ~500 eV to 1 keV, however for Al X-pinches, it is observed below

500 eV, which is nearly half in comparison to the other metal X-pinches studied presently.

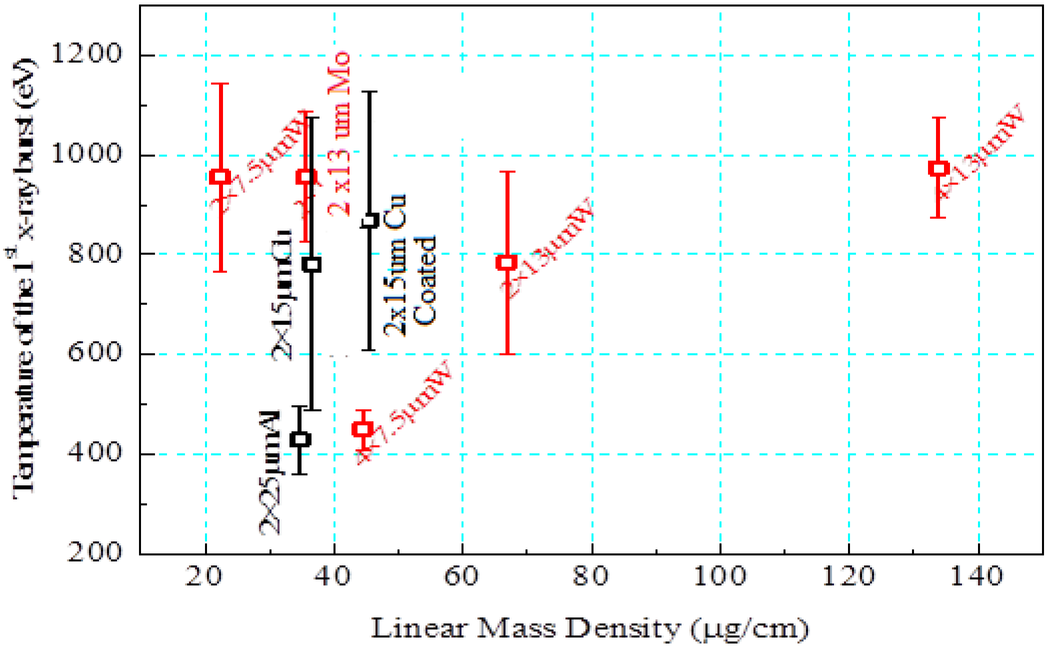

Fig.4.12 Temperature of the hotspot corresponding first burst of x-rays in different X-pinch configurations for dI/dt of ~0.1kA/ns.

The possible reason for the lower temperature of the hotspot in Al X-pinches could be due to the comparatively larger hotspots formed in Al X-pinches. The large range of the temperature is attributed to the sausage instabilities those result in the formation of hotspots. The hotspot temperature in the microsecond drivers is found to be highly variable due to the ns timescale of the sausage instability causing the formation of the hotspot. However, the range of the temperature estimated in this work is found to be similar to that estimated in the X-pinch operated on fast current drivers [122].

4.3 Pulsed radiography of exploding wires using X-pinches

We have characterized the x-ray source formed in the X-pinches driven by a slow current driver. The source size, energy range, pulse width, jitter of the x-ray source in some X-pinch configurations (especially Cu coated, W and Mo) are found to be suitable for point projection radiography of pulsed plasma generated in exploding wires. The dense opaque core of the exploding wire can’t be imaged using conventional techniques such as interferometry or shadowgraphy. We have studied the feasibility of the point projection radiography using X-pinches as a backlighting source by mounting the exploding wires in the return conductors. A 43µm Cu wire has been mounted in one of the return conductors as depicted and described in the schematics presented in section 3.2 of chapter 3. We have obtained the radiographs at various instances to study the dynamics of the exploding wires. The emission timing of the x-rays has been varied using different configurations of the X-pinches.

The radiographs of the exploding wire of 43µm Cu in dI/dt from 0.012 to 0.02 kA/ns at different time instances are shown in Fig. 4.13. As described by Sarkisov et al[123], the wire core expands with constant velocity after the explosion. The average velocity of the expanding core can be estimated by calculating the size of the expanded core at the time of the x-ray burst and the time of expansion after the wire burst. The energy deposited in the exploding wires has been estimated using the methodology described in section 3.1.3. For comparatively faster wire explosions (43 µm Cu wire in Fig. 4.14) it is found to be near the enthalpy of atomization (4 eV/atm). The uniformity in the expansion of the core along the length after the explosion is observed to be comparatively better in the case of a fast explosion (Fig. 4.13a) than slow explosions (Fig. 4.13d). In slow explosions, the wire doesn’t explode throughout the length uniformly but at certain locations. These locations could be the center of nonuniformity due to deformations formed during wire manufacturing. At these locations, the electric and magnetic fields are stronger in comparison to other locations and these are expected to explode at a relatively earlier time. An image of a non-uniform explosion in the wire can be seen in Fig. 4.13d. The expansion velocity along the length in three different lanes (marked in the figure) of the exploding wire radiographs of Fig. 4.13 have been estimated and listed in Table 4.5. At faster explosions, the velocity of the core is estimated to be more than 1.5 km/s as compared to

0.2-0.6 km/s in slow expansions. In one of the images of the radiograph (Fig. 4.13e), the wire corona is also visible and its average velocity till the x-ray exposure is estimated to be 2.1 km/s although due to the low density of the corona region, the estimate of the corona velocity might not be accurate.

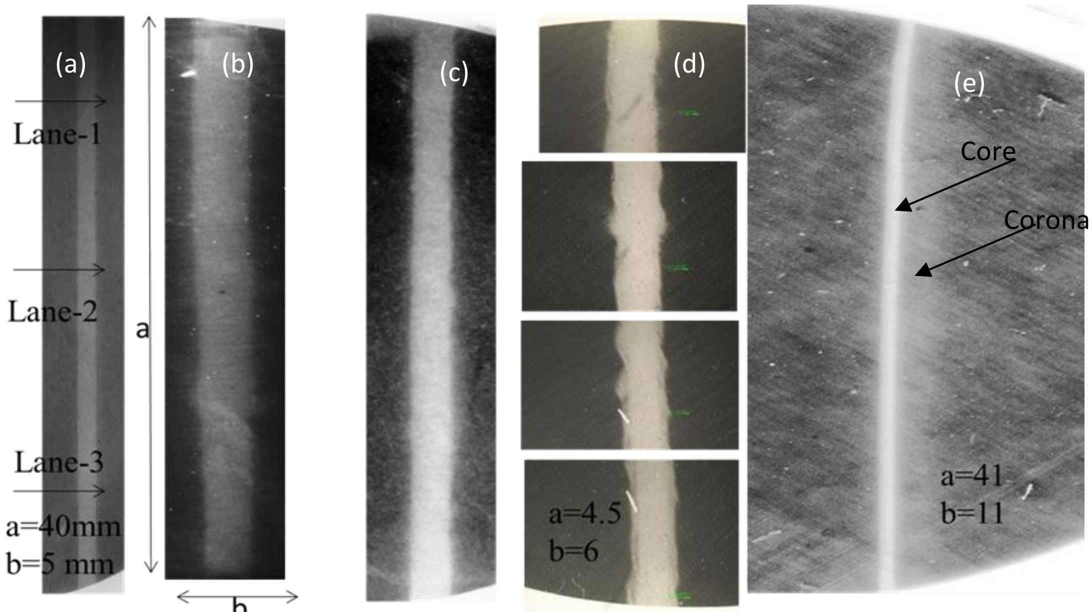

t_{ex}=126 ns t_{Xray}=269 ns

t_{ex}=180 ns t_{Xray}=336 ns

t_{ex}=162 ns t_{Xray}=460 ns

t_{ex}=215ns t_{Xray}=465ns

t_{ex}=231 ns t_{Xray}=429 ns

Fig.4.13 Radiograph of the explosion of 43μm Cu wire in current rate of 0.01 kA/ns to 0.02 kA/ns at different time instances

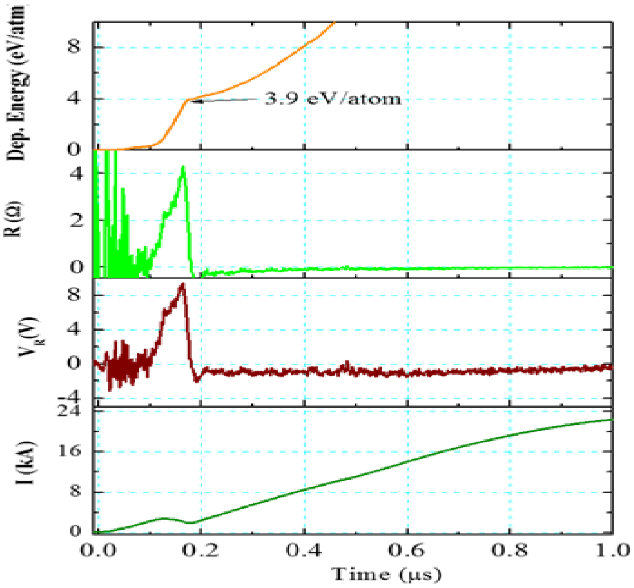

Fig.4.14 The typical signals of current, resistive voltage, and deposited energy EEW of 43 μm Cu wire.

Table 4.5The expansion velocity of the core of an exploding wire of 43 μm Cu wire.

No.	X-pinch	Exploding wire		Expansion Time (ns)	Core dia (μm)	Average exp (μm)	Av. ExpVel (km/s)
		Burst Time (ns)	Peak current				
a	2x7.5 μm W	137	20.8	136	266.7	223.7	1.64
					242.7	199.7	1.47
					253.0	210.0	1.54
b	2x7.5μm W	180	18	156	249.0	206.0	1.32
					254.7	211.7	1.36
					222.9	179.9	1.15
c	2x 13μm Mo	162	17.2	298	222.1	179.1	0.60
					225.7	182.7	0.61
					244.5	201.5	0.68
d	4x13μm W	215	15.5	250	153.4	110.4	0.44
					145.8	102.8	0.41
e	2x13μm W	231	12.8	198	93	50	0.25
					67	24	0.12
					78	35	0.17
					Corona	421	2.13

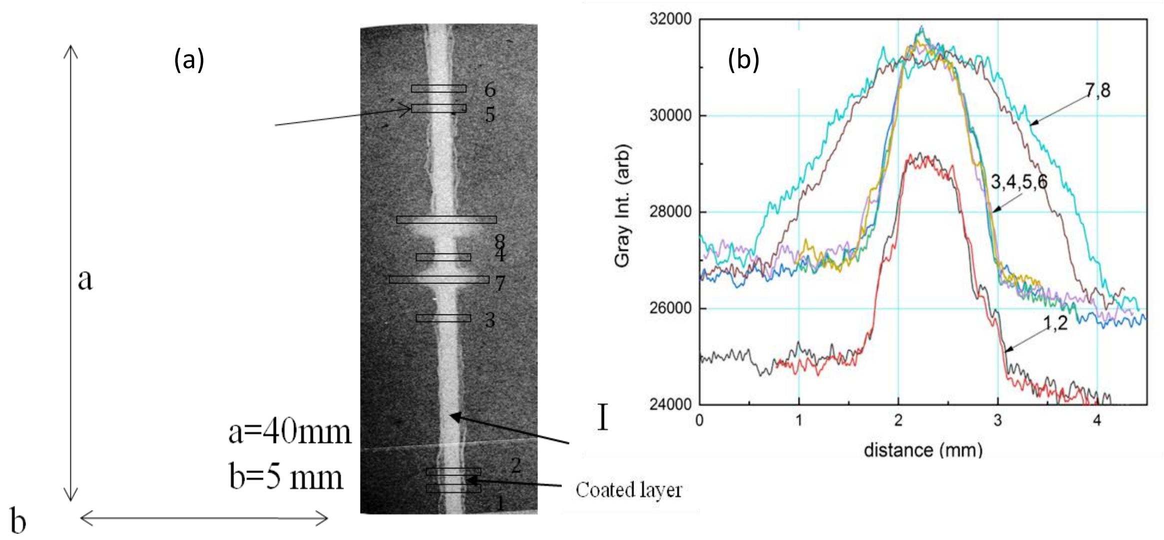

Fig.4.15 A radiograph of 60 μm thick Cu wire exploded in the slow current of 0.01kA/ns. (b) The line profile along different lanes showing the expansion along the length.

In a very slow explosion where the current density in the wire is too small to explode the wire throughout the length, the wire explodes at few locations and forms a droplet structure which is known as unduloid. For example, an image of a wire explosion of 60µm thick copper wire at a slow current of <0.01kA/ns as shown in Fig.4.15, displays the formation of different unduloids along the length. At these unduloids, the expansion velocity is estimated to be 0.7km/s whereas at other locations the core is observed to be barely moving with a very small velocity of <0.1km/s. In addition to the core, the outer layer of the polyamide coating is also visible along the length.

Summary

In this chapter, the detailed work on the development and characterization of X-pinches of different metal wires belonging to the refractory and non-refractory groups is presented. Due to the emission of soft energy x-rays with a short pulse width, the X-pinch device can be used as the radiography source for the imaging of other pulse power plasma. As the X-pinch is a low energy source, it can not be utilized for imaging higher density objects, we have utilized an already developed plasma focus device for the radiography of thicker objects and other material characterization applications which will be discussed in subsequent chapters.

CHAPTER 5

CHARACTERISATION OF PLASMA FOCUS BASED Z-PINCH FOR RADIOGRAPHY

The X-pinch system described in the previous chapter is ideal for the radiography of pulsed plasma and small biological samples. To radiograph denser objects, an x-ray source having higher x-ray energy flux is required. A Plasma focus-based Z-pinch, due to the emission of intense high-energy x-rays can be utilized for the radiography of the denser objects. The neutron fluence of the PF device can also be utilized for investigating the internal structures containing low Z materials. Moreover, the neutrons generated in PF devices are pulsed and practically mono-energetic (2.45 MeV for DD and 14.06MeV for DT fusion). The neutron yield from these devices can be estimated using proportional counters filled with ^{3}He or BF_3 gas, foil activation detectors, and scintillation detectors, etc. For low yield devices, proportional counter detectors appear to be a superior option owing to their significantly higher sensitivity. To quantify the yield, such detectors need to be generally calibrated with fission/radio-isotopic sources such as ^{252}Cf, Pu-Be, and Am-Be which in turn are calibrated for their absolute strength in various ways, i.e., manganese bath system (MBS)[124]and energy independent long counters[125].

Furthermore, in radiography, the thermal neutrons are utilized due to higher attenuation in materials and higher cross-section for detection in imaging devices i.e. image plates. The fraction of thermal neutrons in the spectrum of sources whether fission or fusion, even after moderation is quite small (up to a few percent)[126]. The performance of thermal neutron detectors can be maximized by the selection of appropriate moderating material and optimizing their thickness. However, irrespective of the actual detector, the fraction of thermal neutrons after moderation would not be the same for fusion (to be monitored) and fission (used for calibration) sources. In addition to the thermal region, the other regions of the neutron spectra would also contribute to the overall signal. Therefore, evaluation of the effect of moderator and its thickness with respect to the signal and efficiency of detection in fusion or fission sources is necessary.

In this chapter, we have investigated the capability of a plasma focus device for application in neutron and x-ray radiography. Before utilization of neutrons for radiography, the optimization of moderators for efficient detection using different calibrated detectors (^{3}He and BF_3) has been carried out. A calibration methodology of detectors for mono-energetic neutron sources is also discussed in this chapter.

5.1 Optimization of neutron moderator for yield measurement and neutron radiography

The response of three different sources, *i.e.* Pu-Be, D-D, and ^{252}Cf in single as well as in the form of banks of ^{3}He and BF_3 detectors has been numerically simulated for varying thickness of moderator. The simulation geometry of the detection system is shown in Fig.5.1. The output of the RESINUCLEi card at the optimum thickness of perspex and polyethylene in single detectors is shown in Fig.5.2. The residual nuclei (^{3}H and ^{1}H in ^{3}He detector; and ^{7}Li and ^{4}He in BF_3 detector) formed due to neutron interactions indicate the absolute efficiency (reactions per source-neutron) for the given detector configuration. It can be seen (Fig. 5.2) that polyethylene provides better moderation with smaller thickness as compared to perspex. The absolute efficiency of a single ^{3}He and BF_3 detectors with varying perspex and polyethylene thickness for each of the three types of sources is shown in Fig. 5.3. It is clear from the figure that the detection efficiency first increases with the increasing moderator thickness and reaches an optimum value and thereafter decreases. The increase in efficiency is quite expected due to the enhanced thermalization of source neutrons by the moderator. Further increase in moderator thickness beyond a certain value causes absorption of the thermalized neutrons by the hydrogenous media due to its finite absorption cross-section in hydrogen [127], thereby leading to a lowering in the efficiency of detection.

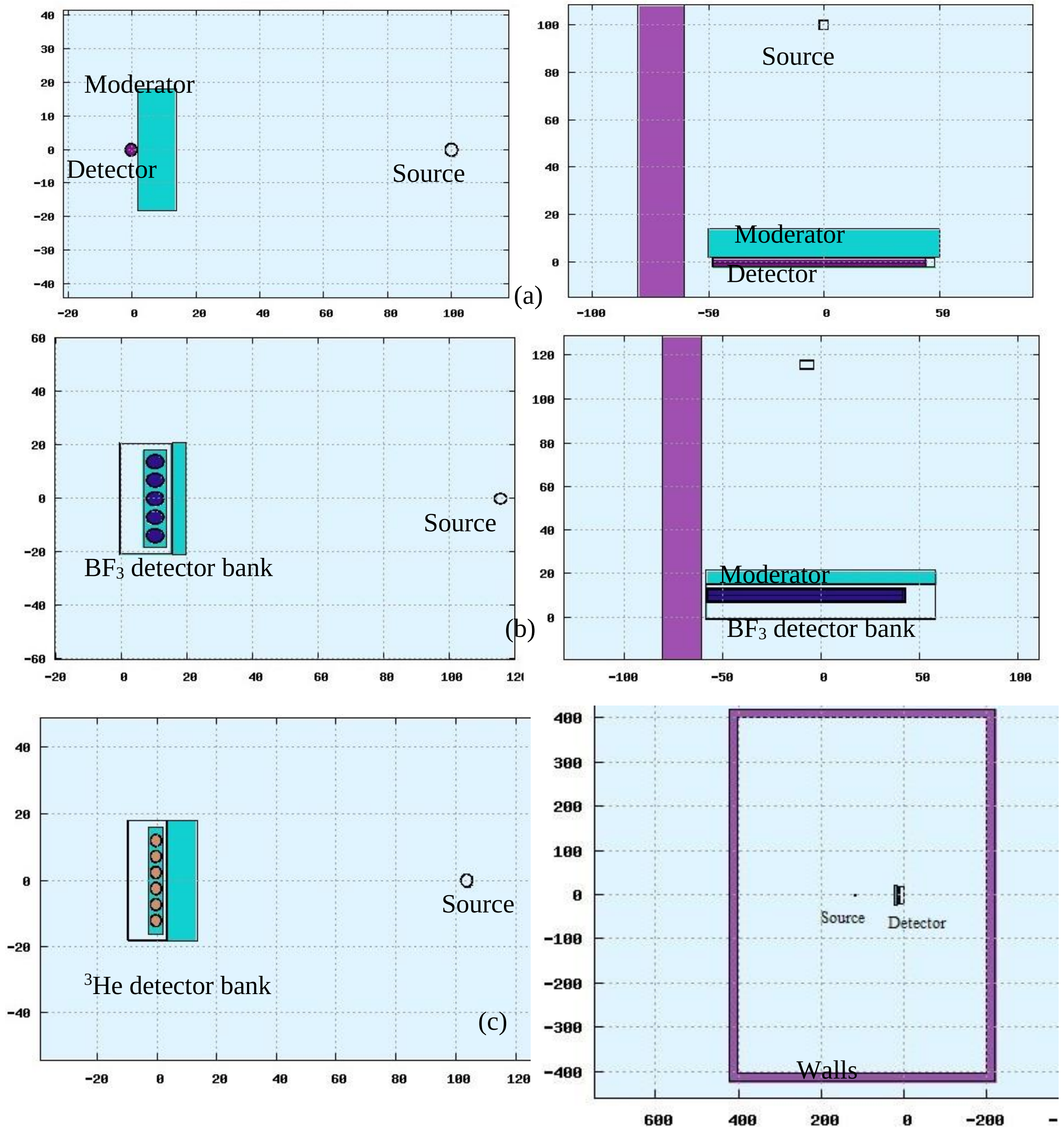

Fig. 5.1 Simulation Geometries for the moderation thickness calculation (a) ^{3}He Single detector tube (b) BF_3 Detector bank (c) ^{3}He Detector bank with concrete wall around the set up.

Simulations of the single ^{3}He detector with a perspex moderator have been carried out for the two cases (i) for setup located in open-space and (ii) for setup placed in a closed-room of 6m×8m×6m with 20 cm thick concrete walls. The maximum detection efficiency of a single detector is determined to be $1.20\times10^{-4}$for neutrons from the Pu-Be source placed in open space, whereas the same is estimated to be $2.94\text{x}10^{-4}$ when the source is kept in a closed room. This significant enhancement of about 2.4 times in the detector efficiency observed for the closed-room configuration compared to that in open space is essentially due to the reflection of neutrons from the concrete walls. Simulations have also been carried out to investigate the effect of individual walls of closed-room on the detector efficiency for a single ^{3}He detector with a Pu-Be neutron source. The floor and ceiling provide an enhancement in the efficiency by 33% and 4%, respectively, as compared to that for the open-space case. The reason for larger enhancement from the floor as compared to that from the ceiling is due to more closeness of the floor to the source. We have also evaluated the effect of walls surrounding the arrangement. In comparison to the case of the geometry consisting of a detector, floor, and ceiling, the geometry with the wall behind the detector and that behind the source enhances the efficiency to 32% and 5% respectively; however, both the side walls provide an enhancement of only 2%. The combined effect of all surfaces provides 2.4 times enhancement in detector efficiency as compared to set-up in the open space.

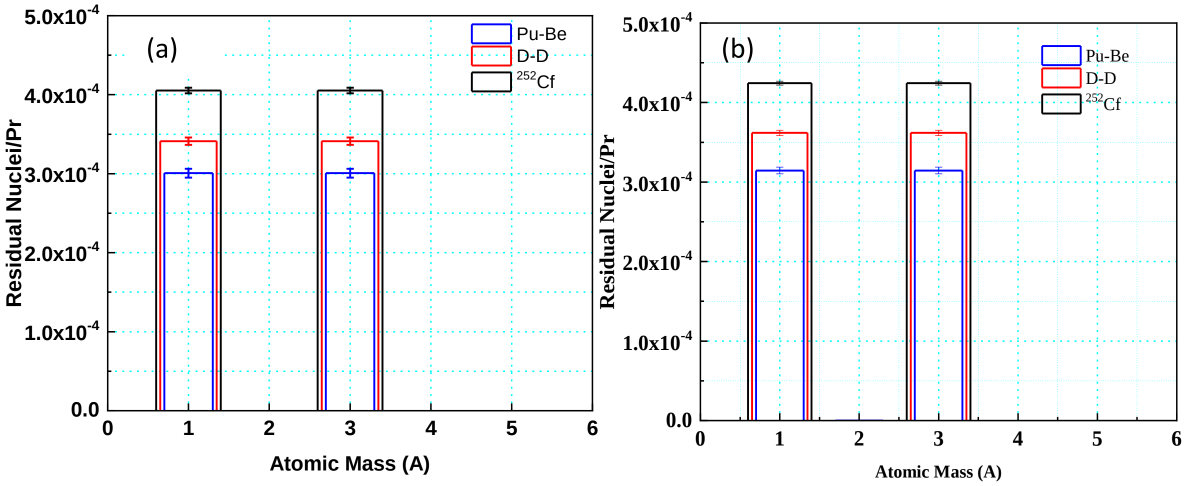

Fig.5.2 Output of RESINUCLEi card (Residual Nuclei) at optimum thickness of (a) perspex (100,100,80 mm) and (b) polyethylene (80,80,60 mm) moderator in ^{3}He single for three sources Pu-Be, D-D and ^{252}Cf.

The effect of moderation material on the efficiency of the detectors of both types has been studied for two moderating materials namely perspex and polyethylene. The optimum moderator thickness in the case of perspex has been determined to be 100mm for Pu-Be and D-D neutron sources, and 80 mm for ^{252}Cf sources. Whereas the same in the case of polyethylene moderator is estimated to be 80mm for Pu-Be and D-D sources and, 60 mm for ^{252}Cf source. As is clear from Fig. 5.3(b) and Fig. 5.3(c), the efficiency as a function moderator thickness for both kinds of the detectors is smaller in the case of perspex than that for polyethylene which could be due to the difference in hydrogen content in moderators; however, it may be noted that the efficiency at optimum moderator thickness is more or less same for both the moderators.

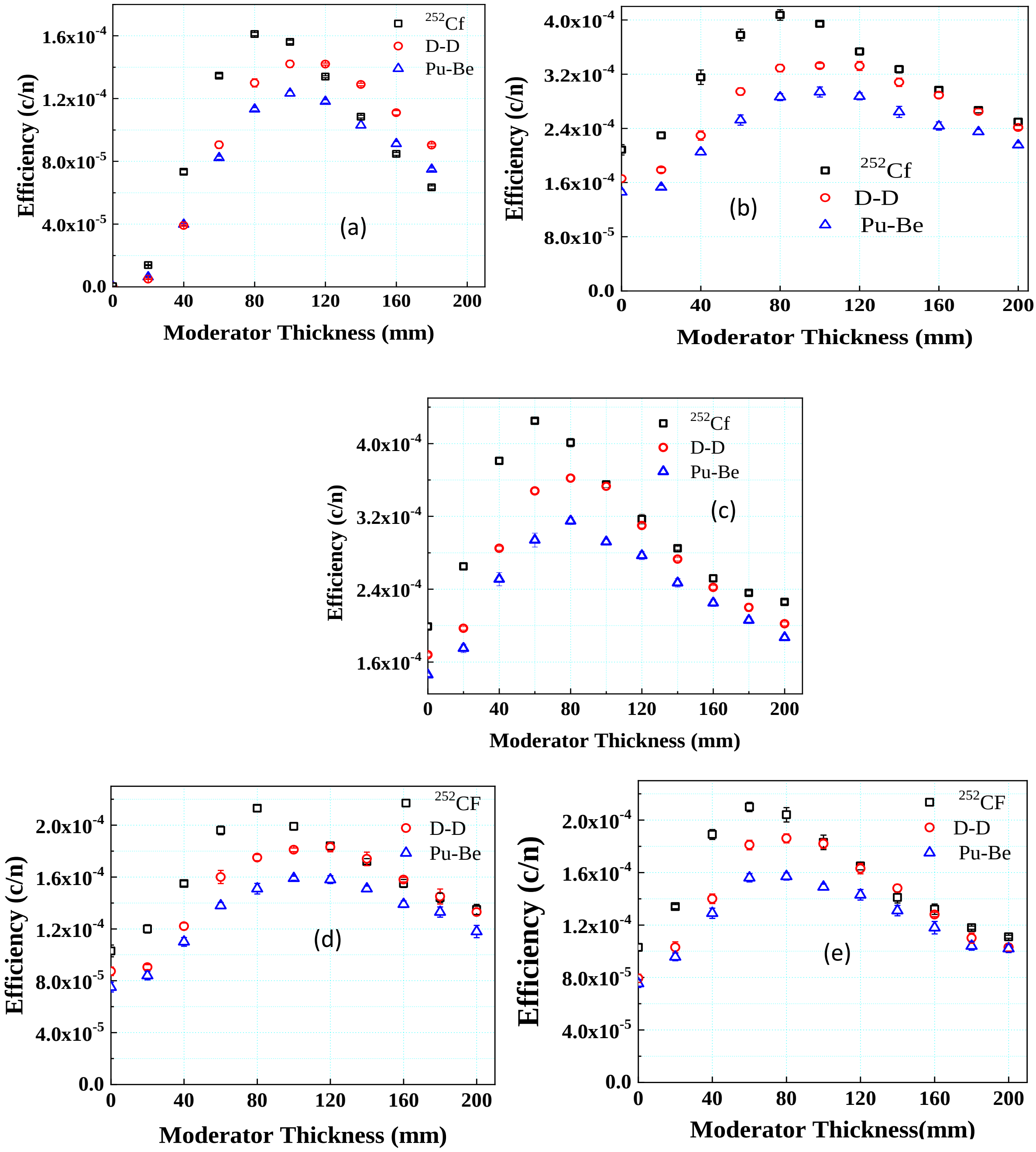

Fig. 5.3 Simulation results for absolute detection efficiency for single detectors (counts/source neutron) Pu-Be, D-D fusion neutron and ^{252}Cf sources with varying moderator thicknesses (a) ^{3}He in open-space with perspex as moderator, (b) ^{3}He detector in a closed-room with perspex moderator, (c)^{3}He detector with polyethylene moderator in closed-room(d) BF$_3$with perspex moderator (e) BF$_3$ with polyethylene moderator.

The efficiency of the^{3}He detector in open space for the three sources Pu-Be, D-D, and ^{252}Cf with respect to the efficiency obtained with Pu-Be source has been determined as

1:1.15:1.31 at the optimum thickness of perspex moderator, while the same for the detector configured within the walls, has been obtained to be 1:1.13:1.35. The slight difference in the ratios for the two cases could be due to statistical error (±1-2%) in the simulations. For a realistic approach, all other simulations were carried out within the walls. For BF_3 detectors the efficiency ratio at optimum moderator thickness for Pu-Be, D-D, and ^{252}Cf source again with respect to that for Pu-Be has been obtained as 1:1.14:1.34 in perspex moderator, while with polyethylene moderator it is 1:1.19:1.34.

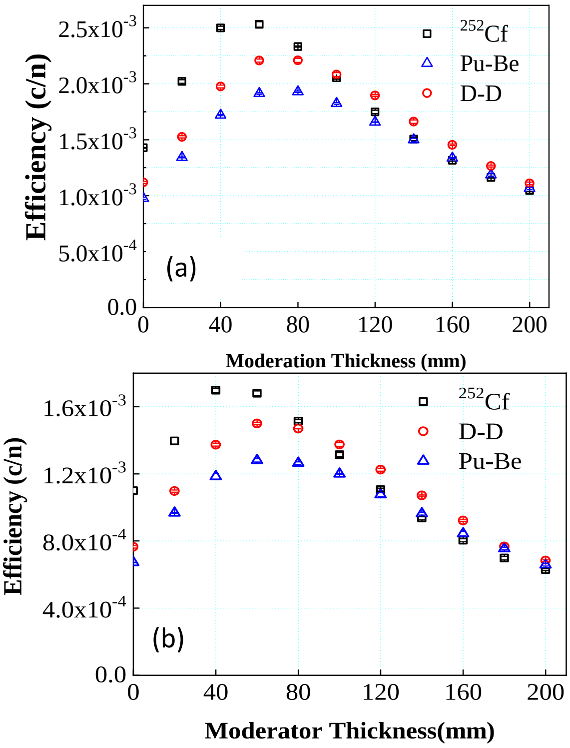

Fig. 5.4 Comparison of efficiencies with variation in perspex thickness for detector banks (a) ^{3}He Detector bank (b) BF_3 detector bank with three neutron sources.

Comparative data of the detection efficiency for all the three sources at optimum moderator thickness is listed in Table 5.1. As both the ^{3}He and BF_3 detectors are sensitive to thermal neutrons, a small difference seen in the ratio (Table 5.1) in these detectors could arise due to statistical fluctuations. The average efficiency ratio w.r.t. Pu-Be for three sources for a single detector (^{3}He of BF_3) is estimated to be 1:1.13±0.006:1.35±0.007 and

1:1.16±0.02:1.34±0.008 for perspex and polyethylene, respectively. Fig.5.4 illustrates the variation of absolute detection efficiency as a function of moderator thickness for detector banks. The details of both the detector banks are provided in section 3.2.6 of chapter 3. The trend in efficiency with a thickness of the moderator for detector banks is seen to be similar to that for a single detector.

Table5.1. Optimum moderator thickness with corresponding efficiency ratios (w.r.t. Pu-Be source) of ^{3}He and BF$_3$ single detectors and detector banks for Pu-Be, D-D fusion, and ^{252}Cf sources

Detector	perspex Moderator		Polyethylene Moderator	
	Thickness(Pu-Be,D-D,CF) mm	Efficiency	Thickness(Pu-Be,D-D,CF) mm	Efficiency
^{3}He single Detector (open Air)	100,100,80	1 : 1.15 : 1.31		
^{3}He single Detector	100,100,80	1:1.13:1.35	80,80,60	1: 1.15: 1.35
BF$_3$single detector	100,100,80	1 : 1.14 : 1.34	80,80,60	1: 1.19 : 1.34
^{3}He Detector Bank	80,80,60	1 : 1.14 : 1.31		
BF$_3$detector Bank	60,60,40	1 : 1.17 : 1.32		

In general, the moderator is inbuilt with the detector i.e. the thickness of the moderator becomes fixed; hence, it is worth estimating the relative efficiency of the detectors for different sources while the moderator thickness is kept fixed. The relative efficiency of the detectors determined for all the three sources with a fixed thickness of perspex and polyethylene moderator optimized for ^{252}Cf source is shown in Table 5.2. For thermal neutron detectors, the ratio of relative efficiency can be obtained by averaging the ratio of these two types of detectors. For perspex and polyethylene, the ratio of detection efficiency for these sources can be taken as1:1.15±0.03:1.41±0.02 and 1:1.17±0.02:1.4±0.03, respectively, for both kinds of detectors.

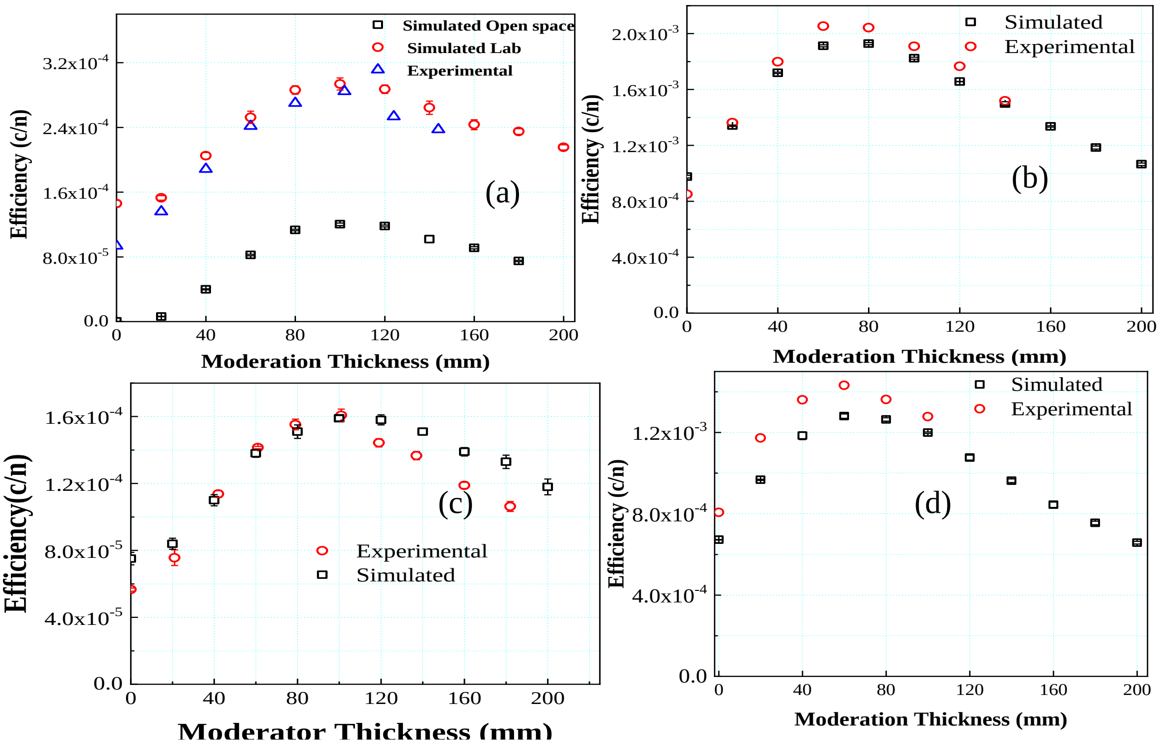

Fig. 5.5 Comparison of Monte-Carlo simulation results with experimental measurements on efficiency of detectors as a function of perspex moderator thickness with Pu-Be neutron source for (a)^{3}He single detector (b) ^{3}He detector bank (c)BF$_3$ single detector (d)BF$_3$ detector bank.

Table 5.2 Ratio of efficiencies for three sources with the moderator thickness fixed at the value optimized for ^{252}Cf

Configuration	perspex		Polyethylene	
	Thickness mm	Efficiency(Pu-Be:D-D:^{252}Cf)	Thickness mm	Efficiency(Pu-Be:D-D:^{252}Cf)
^{3}He detector (Open air)	80	1 : 1.15 : 1.42		
^{3}He Single Detector	80	1 : 1.15 : 1.42	60	1:1.18:1.44
BF$_3$SingleDetector	80	1 : 1.16 : 1.41	60	1:1.16:1.34
^{3}HeDetector Bank	60	1 : 1.15 : 1.32		
BF$_3$Detector Bank	40	1 : 1.16 : 1.43		

Due to the unavailability of calibrated DD neutron and ^{252}CF source, we have validated the simulated results with a calibrated Pu-Be neutron source of 1×10^5 n/s. The results of the simulation of the aforementioned detectors for the Pu-Be source are compared with experimental measurements as shown in Fig. 5.5. In the case of a single detector, the experimental values are generally found to be less than that of simulated ones, which may be associated with the electronic processing, as the low height neutron pulses could be lost in pulse discrimination, thereby reducing the registered count rate. However, for the detector bank, the experimental values of efficiency are higher than that of the simulated ones (Fig. 5.5 (b) and Fig. 5.5 (d)). This may be attributed to the reflection of neutrons from various other materials present in the laboratory, but in the case of single detectors, the effect of reflection from the surrounding laboratory material has not been observed due to the small surface area of the detector. In BF_3 detectors, the pulse discrimination is better owing to its higher full-energy peak (764 keV for ^{3}He against 2.3 MeV for BF_3), hence the effect of reflection appears to be higher in the BF_3 as compared to ^{3}He detector banks. The trend of variation in efficiency with moderator thickness obtained from simulation displays a reasonably good agreement with the experiment.

Further, the optimum moderation thickness for a single detector and the bank is also found to be different. This can be attributed to additional moderation provided by the grooved perspex sheets inside detector banks. To assess the difference in counts due to grooved perspex, we have simulated the detection efficiency of both the detector banks without grooved perspex also. It is seen that embedding by perspex sheets provides additional moderation to the source neutrons that result in up to a 25% enhancement in the detection efficiency in the ^{3}He detector bank. In the BF_3 detector bank, the enhancement in detection efficiency is more than by a factor of two as compared to that for the ^{3}He detector bank. The enhancement is maximum for ^{252}Cf

(23% in ^{3}He and 150% in BF$_3$) source compared to that for the other two sources, e.g. it is ~5% and 8% in ^{3}He detector bank and 106% and 109% in BF$_3$ detector bank for Pu-Be and D-D source, respectively. The ratios of efficiencies for the three sources have been estimated to be 1:1.12:1.25 and 1:1.15:1.35 for the ^{3}He and BF$_3$ detector banks respectively. The relatively high efficiency in the case of BF$_3$ detector bank could be due to the large width (70mm) of the grooved moderator placed inside as compared to 45 mm that in ^{3}He bank.

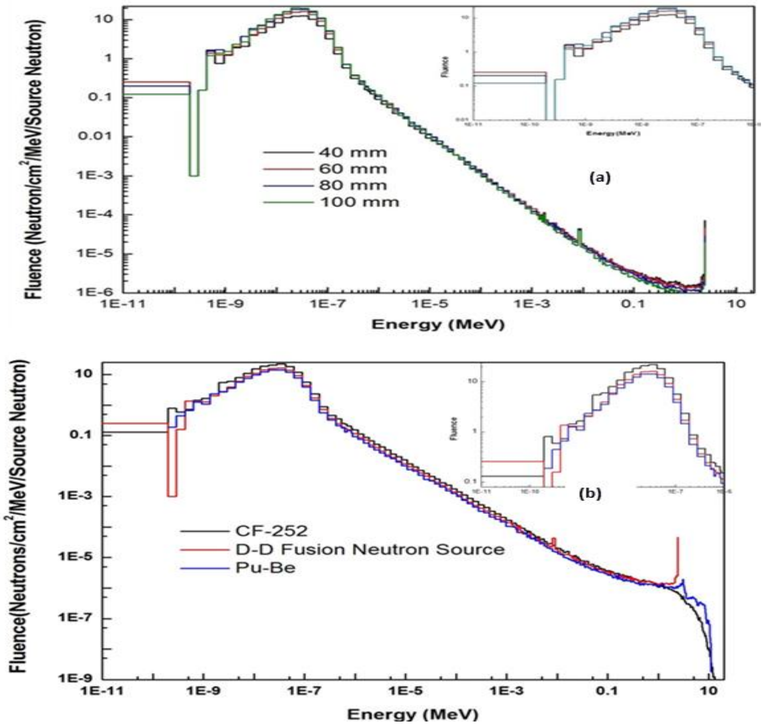

Fig. 5.6 Fluence of neutron after the perspex moderator while source is at 100 cm from the surface of detector (a) Fluence after moderator with varying thickness with D-D source (b) The neutron fluence after 60 mm moderator thickness. (Inset: fluence of thermal neutrons).

The average neutron fluence without moderator at the detector location is determined to be $1.3\pm0.06\times10^{-5}$ n/cm^2 for the D-D source placed at 100 cm from the surface of the detector. However, the same with the moderator for various thicknesses are plotted in Fig. 5.6(a). The same quantity is plotted in Fig. 5.6 (b) for different neutron sources for a near-optimum thickness of the moderator. The fluence has been plotted in /cm^2/energy-bin/source-neutron, which is always less than 1. The energy bins in the FLUKA library are non-uniform, so the fluence has been plotted here in /cm^2/MeV/source-neutron, which is higher than 1 for the lower energy range. For all the moderator thicknesses, the neutron fluence increases as a function of neutron energy and acquires a maximum value at a certain energy, thereafter it decreases monotonically for still higher energies. As far as the fluence for different neutron sources for a fixed thickness of moderator (60 mm) is concerned, it is highest for ^{252}Cf source for the entire energy range among all the three sources, thus, imparting the highest sensitivity for this source.

These simulations suggest that the efficiency of a detector with optimized moderator thickness using a calibrating source is not necessarily the same when used with interrogating source. The difference should be taken into account and accordingly, calibration factors should be modified for applications such as yield measurement, neutron activation studies, or neutron radiography.

5.2 Characterization of PF device for x-ray radiography

The PF device is an excellent source of x-rays of a wide energy range from soft to hard regime, neutrons, and ions. An 11.5 KJ PF device has been characterized for the x-ray imaging parameters using image plates(IP). The method involves exposing different samples to be radiographed to x-rays coming out from a 5 mm thick perspex window and recording the image on BAS-MS, and Durr NDT make HD-IP. The x-ray emission profile from the PF device, the spatial resolution of the detection system, and the energy range by step wedge method are discussed in the following sections.

5.2.1 Timing of x-ray and neutrons

The time profile of the x-ray and neutrons from the PF device has been measured using a 2” thick plasma scintillation detector. It is placed at a fixed distance from the PF device. A typical time profile of the neutron and x-rays is shown in Fig. 5.7. The x-ray and neutron pulses are separated by the time of flight of the neutrons, for this particular shot the plastic scintillator was placed at 3 m from the center of the PF device. The pulse width of the x-ray and neutrons in the 11kJ PF device is determined to be 35±10 ns and 46 ±5 ns respectively, which indicates that a fast-moving object having a time scale of the order up to μs can be radiographed with exposure of neutrons or x-rays. The neutron energy can be estimated from the separation of the x-ray and neutron pulse using the time of flight method. The energy of the neutrons so obtained is 2.58±0.5 MeV.

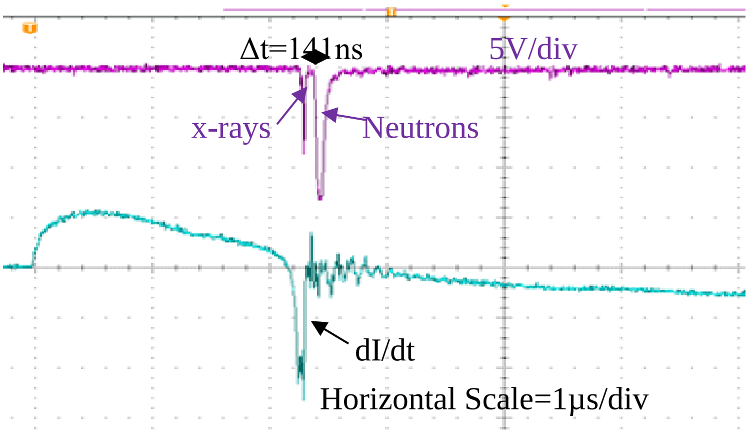

Fig.5.7 The time profile of neutron and x-rays from plasma focus device.

5.2.2 Energy profile of x-rays from PF device

The energy range of x-rays emitted from the PF device is from hundreds of eV to several hundred keV. The flange towards the radiography port is made of 6 mm SS which could attenuate the x-rays, so we have fixed a 5 mm thick perspex window on a hole made in the SS flange to lower the attenuation of x-rays for better image contrast. This window can transmit more than 8 keV x-rays with 5% transmission. To get a better field of view and lower spatial resolution the image plates were kept at 40 cm from the surface of the window, which is almost 50 cm from the x-ray source. To get a suitable sample size, we have carried out the energy estimation using step wedges of Al and Cu. The energy from the image has been derived from the following relationship:

$$I = I_0 e^{-\mu(E)x} \tag{5.1}$$

Here I_0 and I are the incidents and transmitted intensities on the wedge, μ is the energy-dependent attenuation coefficient and *x* is the thickness of the wedge. We have used Al and Cu step wedges with step sizes of 2 mm and 0.17 mm having a maximum thickness of 14 mm and 1.2 mm, respectively (radiograph shown in Fig.5.8a). The line profile in different lanes of these step wedges is shown in Fig. 5.8b. The gray values in the inner lanes (3,6) of the radiograph were observed to be more compared to outer (2,7) ones, which indicates that in the axial direction, the intensity of the x-rays is comparatively more. The energy transmission windows of these two wedges are 8 keV to 34 keV and 8 keV to 50 keV, respectively. The lower limit of 8 keV arises from the 5 mm perspex window used in the setup.

We have plotted line profiles along different lanes in the image and estimated an average energy profile of the x-rays. A typical energy profile of the x-rays is shown in Fig. 5.9. It is clear from Fig. 5.9 that there is a significant contribution of x-rays in the lower energy region and the intensity of the x-rays decreasing with the increasing energy. In the x-ray spectrum of the PF device, the contribution of hard x-rays is observed to be very small as compared to soft x-rays. The higher energy spectrum of the x-rays from the PF device can be utilized by placing metallic filter plates in front of the detectors[128]. The energy information of the source could help to choose the windows and filters to get better contrasts for samples of variable thickness.

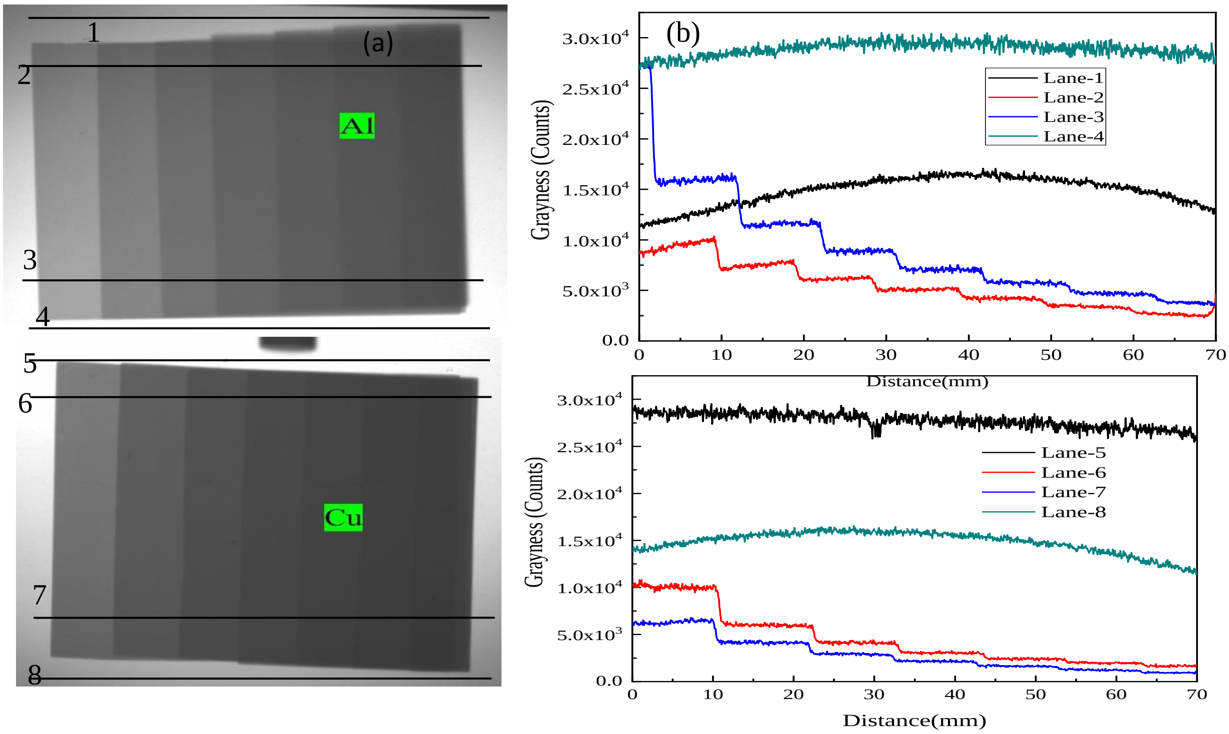

Fig. 5.8 The x-ray energy profile estimation (a) the transmitted greyness through the Al and Cu step wedge. (b) The line profile in Al wedge along the lane 1, 2, 3 and 4 (top), and in copper along the lanes 5, 6, 7 and 8 (bottom).

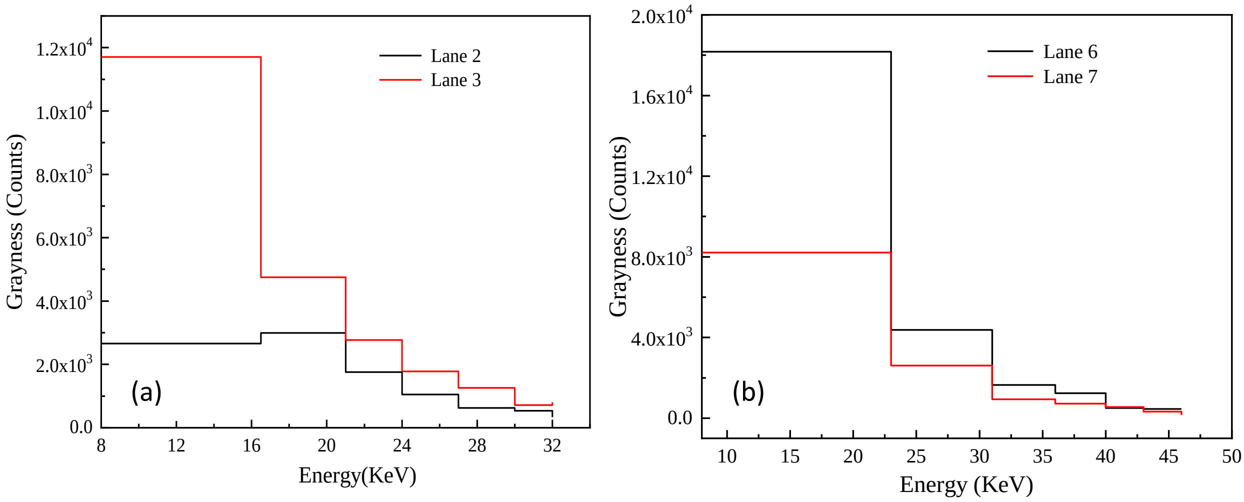

Fig. 5.9 Energy profile of x-rays recorded at the image plate placed at 50 cm from the centre of source (a) x-ray profile along the lane 2 and lane 3 in Al(b) the x-ray profile along the lane 6 and 7 in Cu.

5.2.3 Estimation of source size of x-rays

The neutron and x-ray flux from the PF device is observed to be comparatively higher in the axial direction. The anisotropy in the neutrons and hard x-rays in PF devices of different energy have been studied earlier[129, 130]. In order to utilize the higher flux, we have carried out x-ray radiography in an axial direction. To get the source size, we have obtained a radiograph of a pinhole in an axial direction with unity magnification. A typical image of a pinhole is shown in Fig. 5.10. The size of the source so obtained is 1 mm. Referring to the Eq. 3.15 of chapter 3, the spatial resolution of the object in radiography depends upon the source size and magnification. Even though due to the larger source size the PF device can’t be utilized for point projection radiography, the high flux of the device is well suited for the imaging of small objects through contact radiography. The overall spatial resolution that can be obtained through optimization of various parameters is discussed in the subsequent section.

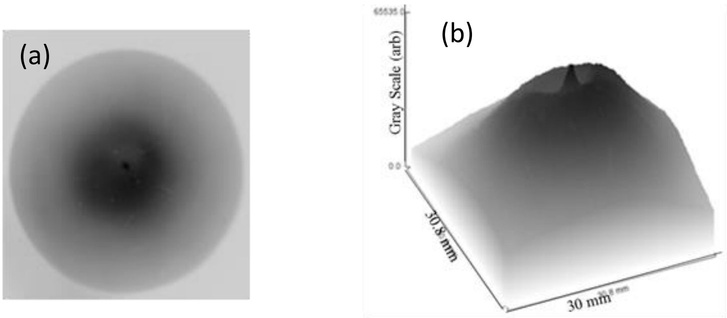

Fig.5.10(a)The Pinhole (placed in axial direction) image of the source (b) the surface profile.

5.2.4 The spatial resolution in radiography

The spatial resolution of the radiography system utilizing PF device as a source and image plate as a recording media has been estimated using the resolution strip and edge spread function method. The resolution depends on the thickness of the sample, sample to detector distance, track size and the range of the particles in the detector material, and in-homogeneities in neutron beam and detector screen. The spatial resolution is quoted in terms of the parameter "total unsharpness, U_T" which is experimentally measured by scanning the grey level intensity of a radiograph of a sharp-edged object. In the present work, a 25 µm thick lead foil was used as a sharp-edged object. It was mounted on the image plate and exposed to x-rays from the PF device. A radiograph of the lead foil is shown in Fig 5.11a. The grey level photo-stimulated intensity (PSL) in the region at the interface between the direct beam and the Pb foil edge was noted. The line profile was fitted to the following edge spread function, ESF [6]

$$ESF = P_1 + P_2.ArcTan(P_3.(x - P_4) \qquad (5.2)$$

Here x is the position coordinate and P_1, P_2, P_3, and P_4 are the fitting parameters in the line profile of the edge. The unsharpness or spatial resolution (U_T) of the image is determined using the expression $U_T = 2/P_3$. The average value of $U_T = 147\pm10$ µm has been obtained by averaging the unsharpness values measured for various interface regions in the image. One of the line profiles is shown in Fig.5.11b.

A similar result of the spatial resolution has been obtained from the radiograph of the resolution strip (typical radiograph is shown in Fig. 5.11 c, d). It is made of fine lines on a stainless steel strip in which fine lead lines having spacing from few tens of microns to mm are engraved. The smallest line spacing resolvable in the radiograph of the strip provides the minimum spatial resolution that can be obtained in the image. In the line profile (Fig. 5.11e) of the strip, the line pattern of 150µm is resolvable. The FWHM of this line is estimated to be 145 µm against 150µm, which is due to geometrical blurring. It indicates that a feature of >150µm can be visualized in the radiographic image taken by image plates as a recording media and PF device as a source.

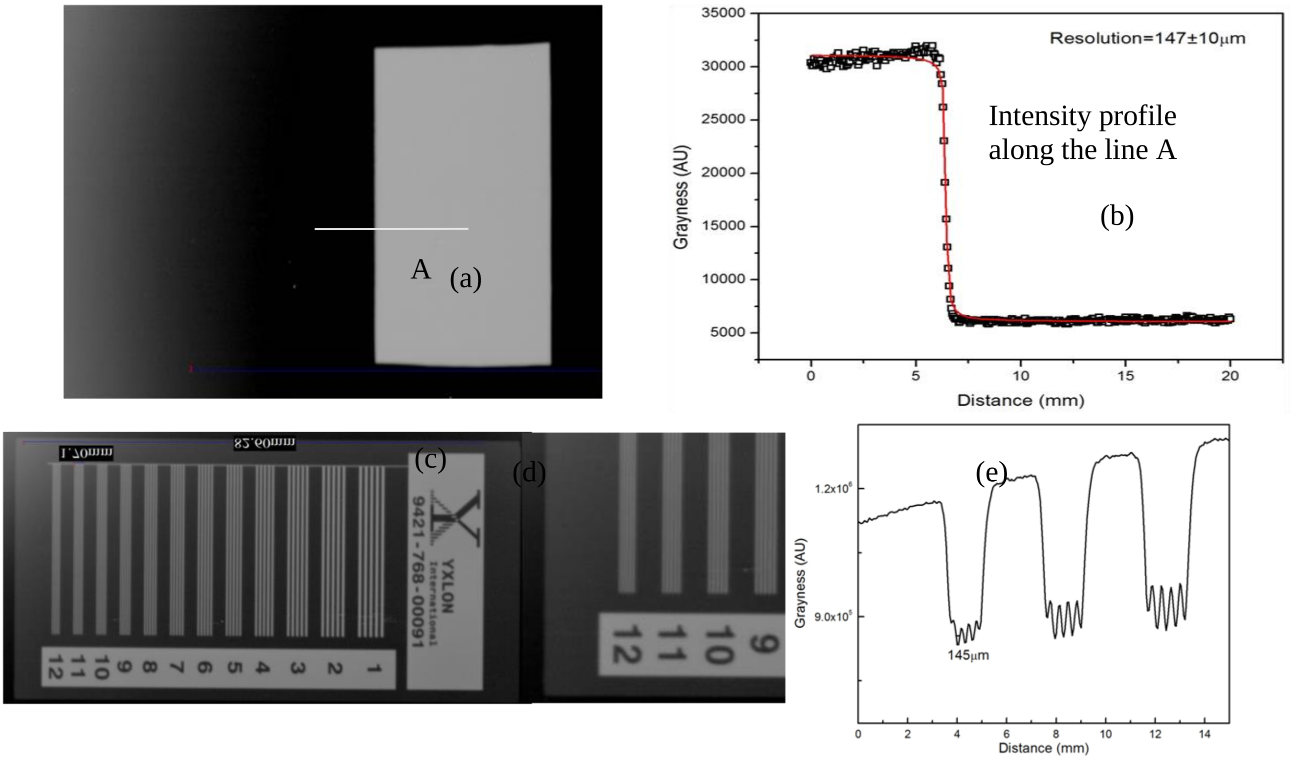

Fig. 5.11 The radiographs of resolution strip and the Pb foil for measurement of spatial resolution. (a) The intensity distribution of the x-ray radiograph of Pb foil on the image plate and (b) the ESF fitting, (c, d) The x-ray radiographic image of resolution strip (e) the minimum distinguishable line profiles on resolution strip.

5.2.5 Estimation of neutron and x-ray contribution in the radiographic image

Radiation from the PF device contains neutrons as well as x-rays and the neutron image plates are sensitive to both x-rays and neutrons. In neutron radiography, the low z elements attenuate the thermal neutrons and produce the contrast, however, in the case of x-ray radiography the higher z elements attenuate the x-rays and produce contrast in the image. To evaluate the feasibility of neutron radiography using the PF device, the contribution of both x-rays and neutrons in the radiograph needs to be evaluated. The neutrons from the PF device are of 2.45 MeV energy, which needs to be moderated before interacting with the object. A 70 mm thick perspex sheet has been placed in between the image plate and the objects for neutron moderation. The estimation was done by covering the neutron-sensitive image plate with Cd and Pb partially and keeping some portion open for thermal neutrons. The radiograph of this arrangement is shown in Fig. 5.12. The Cd sheet blocks the thermal neutrons (below 0.4 eV) and the lead sheet only allows to transmission of the x-rays of a few hundred keV. The ratio of filtered intensities with respect to direct intensity has been used to evaluate the thermal neutron content in the beam. It was found that the beam contained nearly 4.2±2% thermal neutrons and 2% x-rays of energy greater than a few hundred KeV.

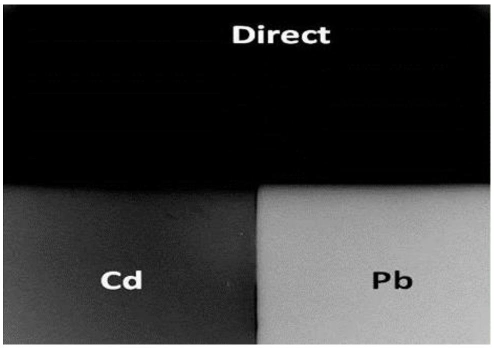

Fig. 5.12 A typical radiographic image of cadmium (1 mm) and lead (2 mm) filters on neutron sensitive image plate (NIP).

5.3 X-ray radiography

Different objects were radiographed using x-ray sensitive image plates. The effect of appropriate window selection discussed in section 5.2.2 of this chapter has been visualized in the radiograph of BNC's placed inside a 2mm thick aluminum box as shown in Fig. 5.13. The images of different BNC's are quite clear. The reason could be the less contributing lower energy x-rays are attenuated by the front wall of the aluminum box, the higher energy x-rays are the only ones contributing to the image.

Some of the radiographs obtained using the x-ray sensitive image plate are shown in Fig. 5.14. The internal structures of these objects can be seen in these images; for example, in Fig. 5.14a, graphite in the copper tube can be visualized. Connections in a solid-state relay switch (Fig. 5.14 d), the connections of a computer ram (Fig. 5.14e), mouse (Fig. 5.14f), and the internal structure of a pen drive (Fig. 5.14g) are shown in the images. As the pulse width of the x-rays in the PF device is few tens of ns, to assess its capability to radiograph the fast-moving object, we have taken a rotating computer fan with4000 rpm as an example and the image of the same is displayed in Fig 5.15. As can be seen in the image, the blades and winding of the motor can be visualized in the radiographic image (Fig.5.15).

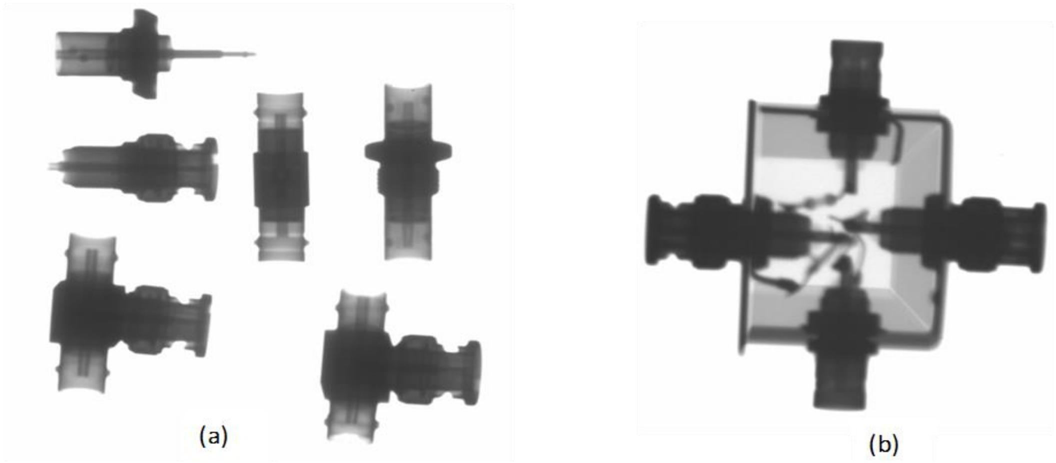

Fig. 5.13 The x-ray radiographs (a) of BNC connectors kept inside a 2 mm thick Al metallic box. (b) Radiograph of a distribution box.

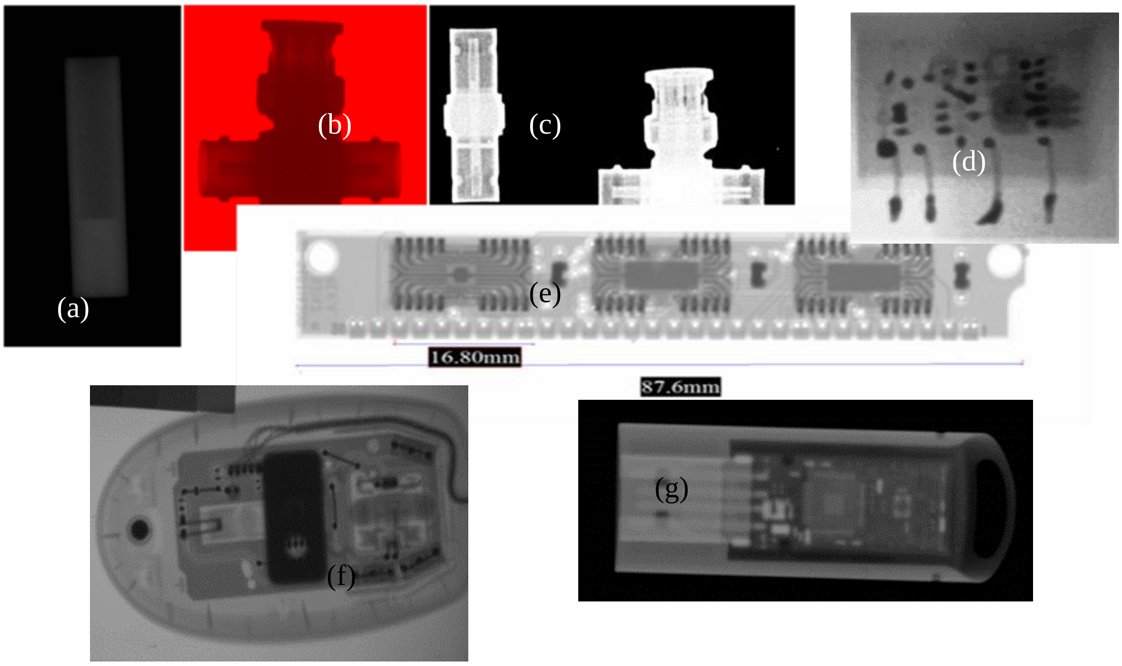

Fig. 5.14 The x-ray Radiographs of various objects (a) Copper filled tube with graphite (b, c) BNC connectors (d) SSR switch (e) Computer RAM (f) The computer mouse and (g) Pendrive.

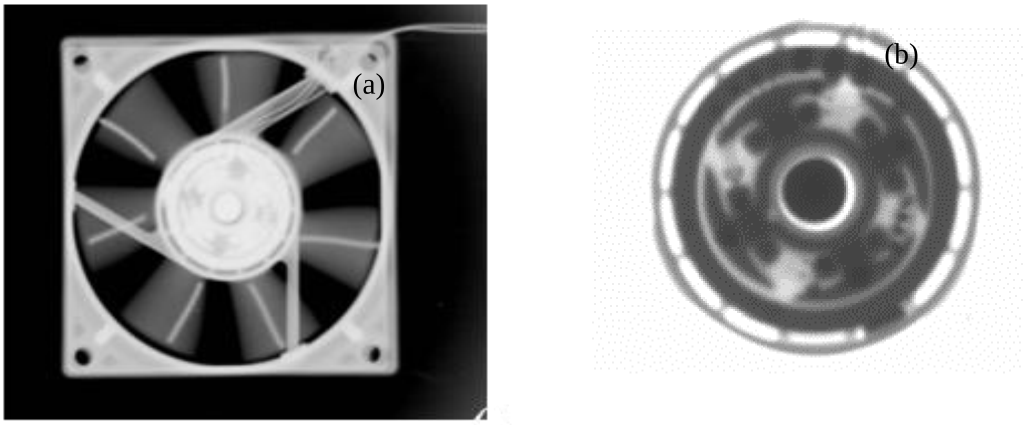

Fig. 5.15 Radiographic image of (a) a fast moving computer fan (b) motor of the fan.

5.4 Neutron radiography

Different objects were radiographed using a Fujifilm make neutron sensitive image plate (BAS-ND) with varying moderator thickness. A neutron radiograph of the tungsten turbo-jet blade sample of 10mm thickness is shown in Fig. 5.16. As can be inferred from the image, this blade consists of tubing of different diameters in the 10 mm thick tungsten plate; which is filled with wax which is a neutron absorbing material. It is to be noted that towards the bottom there are small holes inside the tube which are not visible in the image due to the low fluence of thermal neutrons. It suggests that due to the low intensity of thermal neutrons, smaller size features are not visible in the radiograph.

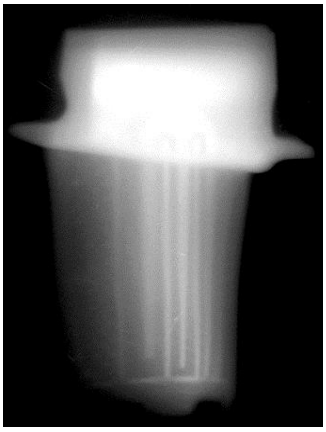

Fig. 5.16 Radiograph of the turbo jet blade recorded on BAS-ND 2025 IP with source yield 10^9 fast neutrons with 70 mm perspex moderator.

Summary

In this chapter, Monte Carlo simulation studies have been reported on the optimization of the moderator thickness required for the utilization of the gas-based pulsed neutron source for various applications. A series of simulations have been conducted for the selection of moderators viz. perspex and polyethylene and the optimization of their thickness to maximize the yield. A calibration methodology for the yield estimation of pulsed and mono-energetic neutron sources using radio-isotopic and spontaneous fission neutron sources has been established. The experimental validation of the simulation has been carried out only for the Pu-Be neutron source as the PF device being pulsed neutron source has large shot to shot variation in the yield. The results obtained in these simulations suggest that using a radio-isotopic and spontaneous fission source for calibration of detectors for yield estimation from pulsed fusion neutron sources such as PF device could result in an error of ~40%. It has been calculated that a correction factor needs to be accounted for in such situations.

The chapter also presents the characterization of PF devices carried out for applications related to radiography. Also, neutron and x-ray radiographic studies have been carried out on various objects employing PF devices. The characterization of PF devices for radiography applications includes the estimation of energy profile, spatial resolution, source size, and time profile. Although due to the smaller fluence of neutrons, further studies are required for its utilization in neutron radiography, the x-ray imaging results suggest that the PF device can be utilized for imaging a few cm thick objects.

CHAPTER 6

ASSAY OF FISSILE MATERIAL EMPLOYING PLASMA FOCUS BASED Z-PINCH

The plasma focus devices are an intense source of neutrons when employed with the deuterium (D_2) gas or a mixture of deuterium and tritium (DT) mixture. These can be utilized for the characterization of material by neutron activation methods. Being a single-shot device, plasma focus has an advantage over other conventional sources as it has a low source background, which is beneficial to attain lower minimum detection limits. Further, the activity of the source neutron lasts up to a few ms in the sample which makes this device useful for detecting the neutron-induced activity of comparatively shorter half-life. This chapter presents the characterization of fissile material in various sample matrices using plasma focus devices having neutron yield in the range of 10^8- 10^9 per pulse. Experimental results on the assay of enriched uranium in small oxide samples and compressible waste packets in addition to natural uranium in industrial radioactive waste are presented. Monte Carlo simulations for designing the detection assemblies are also discussed in this chapter.

6.1 Assay of enriched uranium in compressible laboratory waste

Material accounting and safeguards is an important issue in the fuel fabrication sites where the fissile material is handled. A novel and rapid technique is developed for the assay of uranium in the waste utilizing the pulsed character of fusion neutrons of the PF device. The methodology of the technique is described in Chapter 1 and the details of the presently developed system are provided in section 3.4.1 of chapter 3. A well-type detection system having a sample cavity surrounded by ten^{3}He detectors has been developed for delayed neutron counting. We have used a low-intensity ^{252}CF source for testing the cavity for uniformity in the efficiency inside the entire volume. It shows that there is only a <5% efficiency variation along the diameter of the well and up to 200 mm height from the bottom the variation of efficiency is <9 % which indicates that once the delayed neutron is generated, it has uniform efficiency in the well of volume 6 liters.

We have used a medium energy plasma focus device as an interrogating neutron source for the assay. The maximum neutron yield observed in this device is (4.5 ± 0.6) $\times 10^8$ n/pulse. We have used enriched uranium (14.8%) oxide (U_3O_8) samples with a mass range from 50mg to 50g to obtain the calibration curve for the delayed neutrons versus fissile content. In addition to the oxide samples, two metal samples have also been assayed. To assess the feasibility of the technique for the assay of compressible waste and to check the effect of the matrix, we have prepared a simulated waste packet consisting of a few grams of uranium distributed in the compressible material such as lab coats, gloves, and absorbent paper. The samples, as well as the waste packet, were placed in the cavity of the well detector, which is placed over the PF chamber as shown in Fig. 3.7 of chapter3. The delayed neutron activity is recorded in MCS mode with a 50 ms delay and 50 ms dwell time.

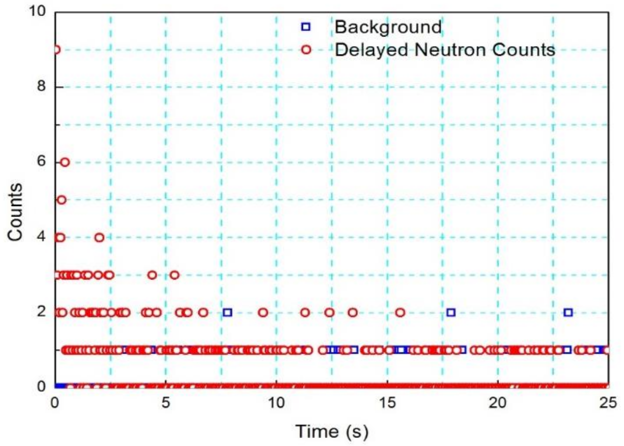

Fig. 6.1 A typical profile of delayed neutrons in the simulated waste packet.

The temporal profile of delayed neutron counts is shown in Fig. 6.1. It is seen to follow exponential behavior. In the induced fission of ^{235}U, the delayed neutron yield is maximum from the precursors corresponding to the half-life of 2s and the neutron background in the monitoring area was comparatively high (~4cps). So, to enhance the signal to background ratio, the delayed neutron (DN) activity from induced fission of ^{235}U present in oxide samples was accumulated for 10s. In this time, nearly 70% of the delayed neutron activity is over. The time-integrated DN counts (for 10s) were corrected over the background, and further normalized with average neutron yield.

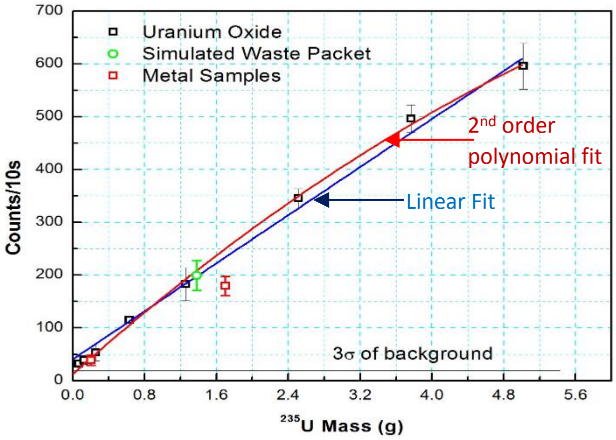

Fig. 6.2 the variation of delayed neutron counts (in 10s) with the fissile material in the samples.

The integrated counts with fissile quantity in uranium oxide and metal samples are shown in Fig.6.2. The integrated neutron counts appear to follow a linear profile with the fissile (^{235}U) mass in the sample. Rigorous observations, however, show that the profile is somewhat nonlinear similar to that in our earlier reported work[84]. The curves are fitted both with linear as well second-order polynomial regression. The fitting parameters are listed in Table 6.1. The low value of the intercept infers a better sensitivity of the technique. Furthermore, the non-linearity in the DN counts could be due to self-shielding by the sample; it is more prominent in the thick higher mass samples, which leads to insufficient irradiation of fissile material and low

DN counts. The nonlinearity might be reduced in the waste packets where the fissile material is likely to be more uniformly distributed as also by enhancing the neutron yield from the source. The delayed neutron counts from the laboratory waste packet are also shown in Fig. 6.2. It follows the same trend as obtained from the assay of oxide samples. This infers that there is a negligible effect of compressible waste on the delayed neutrons. The detection limit of the system is estimated within the 3σ limit of the background. For the present system, it is estimated to be ~40mg of ^{235}U. As the neutron background in the monitoring area is comparatively higher, the detection limit can further be reduced by using neutron shielding for detectors and enhancing the source neutron yield.

Table 6.1 The parameters for the linear and polynomial fitting of mass vs counts calibration graph

Parameters	Linear Regression $Y=a+b*x$	Polynomial $Y=a+bx+cx^2$
a	40.8±13	12.6±9
b	113±4	15±9
c		-6.9±1
R	0.992	0.998

6.2 Assay of natural uranium in industrial radioactive waste

The Active Interrogation by Delayed Neutron Counting (AIDNEC)technique described in the previous section has been extended for the assay of natural uranium in the waste generated in the fuel fabrication facilities. As for a given enrichment and composition of the sample matrix, the induced fission neutron or gamma flux is proportional to the mass of fissile material present in the sample. To look into the effect of enrichment and the sample matrix, we have performed the feasibility experiments using a medium energy plasma focus (MEPF-17) device for the assay of natural uranium in industrial waste generated in the fuel fabrication facility.

The objective of the demonstration is to evaluate the deployment perspective of the system for active assay of natural uranium in the civil and metallic waste produced in the fuel fabrication or other such handling facilities. Different sample matrices could give a source of uncertainty due to the self-shielding of interrogating neutrons and self-absorption of the delayed neutrons. In this context, we have performed experiments on three samples in the form of soil and civil debris containing natural uranium using a deuterium gas-operated plasma focus device (2.45 MeV neutron source). Prior to conduct, the experiment, Monte Carlo simulations have been carried out for the optimization of the moderator for the detector as well as sample. Simulations have also been carried out to evaluate the future perspective of using a D-T (deuterium-tritium) operated PF device for such applications. These studies are discussed in detail in the subsequent subsections.

6.2.1 Monte Carlo simulations for optimization of moderator thickness

The waste samples being studied here are in form of civil debris containing neutron attenuating material such as concrete chunks, brick pieces, and sand. So the standard moderator thickness estimated in section 5.1 of chapter 5 cannot be employed here. Moreover, the optimization of moderator thickness is difficult using a plasma focus device due to its inherent variation in the shot-to-shot yield. Monte Carlo simulations using FLUKA have been carried out for optimization of sample moderator and the moderator for thermalization of the delayed neutrons. The simulation geometry consisting of PF neutron source, sample (waste packets), and ^{3}He neutron detectors is the same as that presented in Fig. 3.10 of chapter 3.

To evaluate the effect of the placement of detector (neutron reflection from perspex placed in front of detectors) on induced fission in the sample, we have simulated the fission reactions with varying thickness of interrogating source neutron moderator (polyethylene) for two cases. In the first case, the sample is placed in front of the source without the placement of detectors. In the second case, the sample is placed in front of the source and all four detectors (with 20 mm perspex) were placed around the sample (Fig. 3.10). Due to the comparatively lower energy of delayed neutrons, we have taken 20 mm thick perspex as a moderator for delayed neutrons, the effect of which is also described later in this section. The number of fission reactions for these two cases with varying thickness of sample moderator (polyethylene) is shown in Fig. 6.3. In the former case of sample irradiation, the number of fission reactions increases with polyethylene thickness up to an optimum value and a further increase in this thickness leads to a reduction in fission. This reduction is attributed to the absorption of thermalized neutrons in the sample.

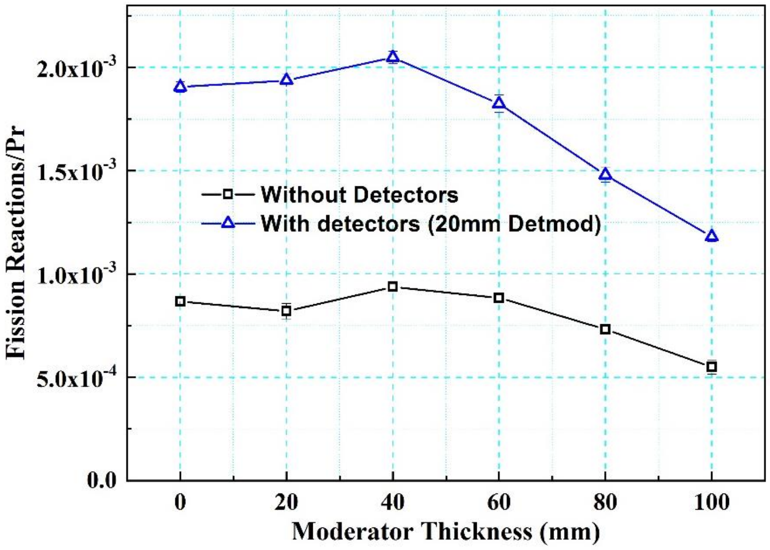

Fig. 6.3 Effect of source neutron moderator for interrogating neutron without and with all the detectors with 20 mm perspex moderator (detmod) placed around the sample.

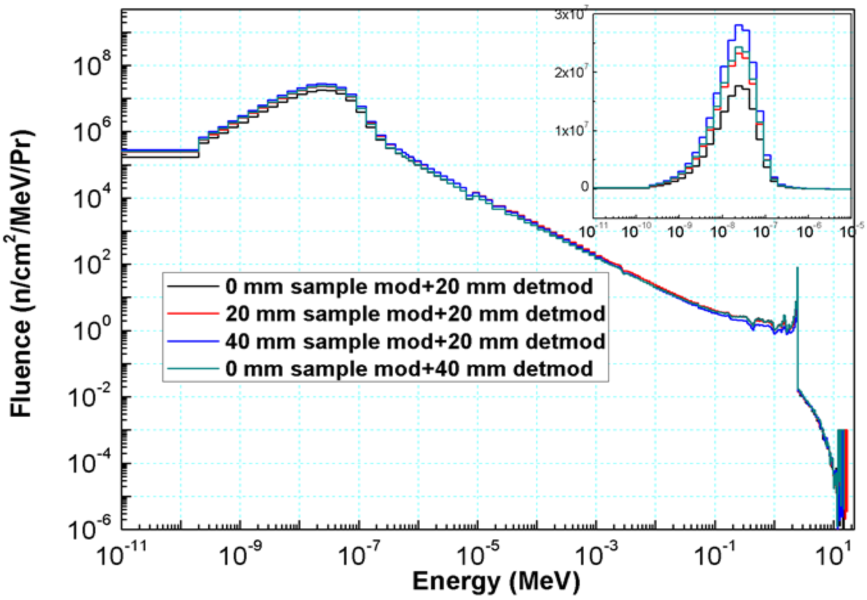

Fig.6.4 Neutron fluence per source neutrons in the sample-1 with combinations of source neutron moderator (sample mod) and detector moderator (detmod) with D-D neutron source.

In the second case, there has been a significant enhancement (2 times) in the number of fission reactions as compared to the first case. The delayed neutron moderator (perspex) placed in front of the detector enhances fission probability due to interrogating source neutron reflection. Also, the fission reactions (Fig. 6.3) for the case with a 20 mm polyethylene placed in front of the sample were found to be lower as compared to a case without a moderator. It can be attributed to the dominance of increased source to sample distance over the advantage of neutron moderation. The difference in fission reactions observed in the sample without a moderator to that corresponding to 40 mm polyethylene is <5%, which could be due to the moderation of neutrons in the sample. So, we have conducted further simulations and experiments without a source neutron moderator.

The simulated results presented above can also be explained in terms of fluence in the sample. The fluence at the sample for three different thicknesses (0, 20mm, and 40mm) of source neutron moderator with a fixed detector moderator thickness of 20mm is shown in Fig.6.4. The fluence is also plotted for without sample moderator case but with a 40mm thick detector moderator. As is clear from Fig.6.4, the neutron population in the lower energy regime (<1eV) increases (the fluence in this regime is shown in the inset) with increasing the sample moderator thickness while the detector moderator thickness is kept fixed. Further, for without source neutron moderator and 40mm thick detector moderator case, the fluence is higher than that for the case with no sample moderator but 20mm thick detector moderator. These results are as per expectation as the larger thickness of detector moderator or sample moderator or their combination will have more slowing down effects and reflections of neutrons. To investigate the neutron penetration in the sample the fluence profile has been simulated and shown in Fig.6.5. The neutron fluence (per source neutron) along the diameter or the length of the sample is not uniform. The fluence in the sample varies from ~10^{-3} n/cm^2 to ~10^{-4} n/cm^2 along the diameter and the same profile has been obtained along the length. Although we have considered the isotropic interrogating source but the radial non-uniformity (Fig.6.5a) is seen in the fluence in the sample. This can be attributed to the material density variation from anode to sample as the reflected neutrons from the anode and the perspex placed in front of the detector could also give rise to higher fluence in the lateral direction. The variation in the fluence along the diameter and the length suggest that to average out the effect of the non-uniform distribution of fissile material in the samples, multiple trials of irradiation must be performed with different sample orientations, and the delayed neutron activity of these trials should be averaged.

The number of fission reactions (*f*) in a fissile material *i* of mass m_i can be estimated by the following expression:

$$f = \sum_i \varepsilon k m_i \phi(E) T \sigma_i(E) \tag{6.1}$$

Here σ_i is the fission cross-section of fissile material i, $\varphi(E)T$ is the source yield, ε is fluence per source neutron and k is the proportionality constant. The delayed neutron counts at the time (t) can be given by

$$A(t) = \nu f \varepsilon_d \sum_{i=1}^{6} a_i \lambda_i e^{-\lambda_i t} \tag{6.2}$$

Here ν is the delayed neutron fraction (0.0158 for ^{235}U) per fission[131], ε_d is absolute detector efficiency for delayed neutrons, and a_i is the fraction of delayed neutrons in the i^{th} group of decay constant λ_i. As we have accumulated the experimental delayed neutron activity for 10 seconds to enhance the signal to background ratio and kept the 50 ms delay time to avoid the interrogating source activity. To accumulate the delayed neutrons for counting time, activity A(t) is integrated from 50 ms to 10s. In this time window, the integration of the terms inside summation of Eq. 6.2 is found to be 0.71 for ^{235}U.

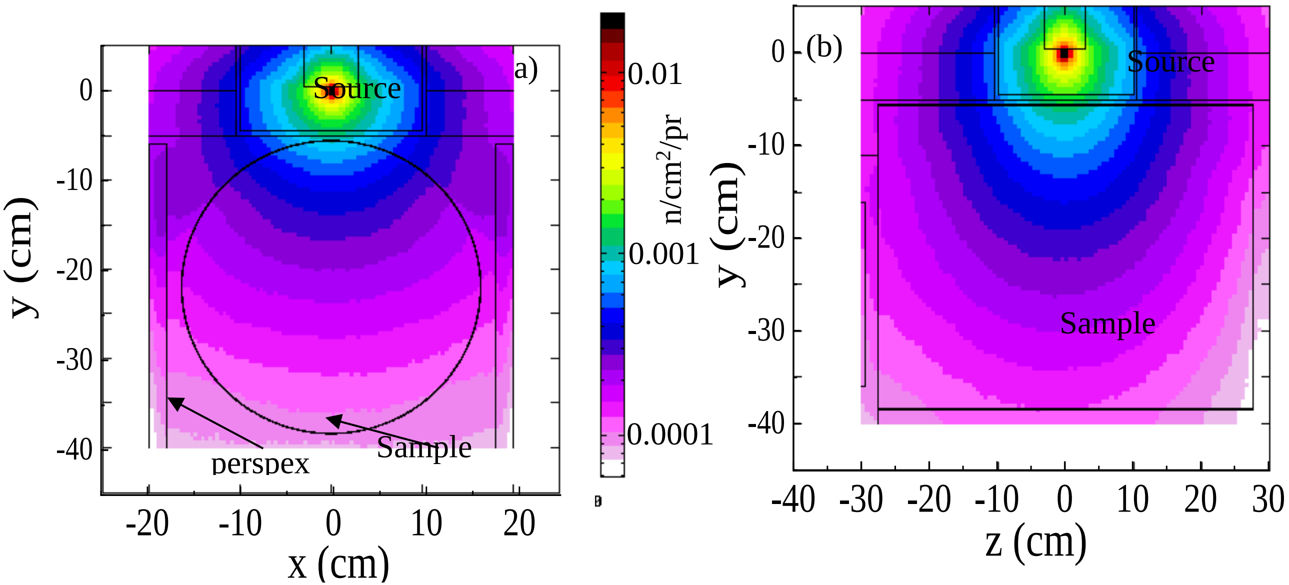

Fig. 6.5 Neutron fluence profile in the sample-1with 20 mm detector moderator configuration (a) x-y plane at the centre of sample (z=0) (b) in z-y plane at x=0

The detection efficiency for delayed neutrons for the above-mentioned cases is listed in Table 6.1 for three samples without source neutron moderator but with perspex moderator for the detector. The efficiency of the detection system has been found higher in the case when a

20mm thick perspex moderator is placed in front of detector banks instead of a 40mm thick moderator (as shown for sample-1 in Table 6.1). It may be noted from Table 6.1 that although the number of fission reactions is higher in presence of the 40 mm perspex (due to relatively high reflection of source neutron as compared to that for 20mm thick perspex), the delayed neutron counts are less as compared to that for 20 mm thick perspex.

Table 6.2 Delayed neutron counts (simulated) in the three samples with DD neutron source

Sample (interrogating Source)	perspex Thickness	Number of fission reactions in a sample (f)	Detection Efficiency for delayed neutrons (ε_d)	Total DN (in 10 s) per interrogating neutron ($f\varepsilon_d \nu t_d$)
Sample-1 (D-D)	20 mm	$(1.91\pm0.02)\times10^{-3}$	$(1.11\pm0.002)\times10^{-1}$	$(2.38\pm0.03)\times10^{-6}$
	40 mm	$(2.25\pm0.02)\times10^{-3}$	$(8.66\pm0.02)\times10^{-2}$	$(2.20\pm0.03)\times10^{-6}$
Sample-2 (D-D)	20 mm	$(1.70\pm0.02)\times10^{-3}$	$(9.80\pm0.1)\times10^{-2}$	$(1.88\pm0.04)\times10^{-6}$
Sample-3 (D-D)	20 mm	$(4.59\pm0.05)\times10^{-5}$	$(1.10\pm0.01)\times10^{-1}$	$(5.69\pm0.13)\times10^{-8}$

For the moderator(perspex) thickness larger than a certain value, the efficiency is found to be decreasing due to the over-moderation of delayed neutrons. Given the above results, the combination of the sample without a moderator for source neutrons and 20mm perspex in front of the detector banks is found to be a suitable configuration for sample irradiation and delayed neutron detection. This inference is in accordance with the results of fluence for varying moderator thickness presented above (Fig. 6.4). The delayed neutron per source neutrons counts in 10 s for all three samples are also listed in Table 6.3. These counts are proportional to the fissile content in the sample.

6.2.2 Experimental results for the assay of natural uranium

The three samples prepared from the waste containing natural uranium were irradiated in the geometry of detectors displayed in Fig. 3.10 in chapter 3. To avoid the interference of interrogating source and the prompt neutrons a delay in the counting is required which should be greater than the timing of the PF neutron source detected in the detection assembly. The time profile of the PF neutron source is shown in Fig. 6.6(a). Although the PF neutron source emits the neutrons in a single (or multiple) burst within 50 ns and the thermalization time in the moderator is few hundreds of μs (max. 1-2 ms) but the source activity in the detector lasts for ~25ms in the present case. This is not much different from results reported in the literature [3, 4] for similar systems. This could be due to the reflection of neutrons (thermal as well as fast) from the surroundings (absorbent materials and walls), which can be reduced by using suitable shielding for applications in the study of short-lived isotopes. To avoid the interference of interrogating source neutrons (from PF) in delayed neutron counting we have counted the activity after a delay of 50 ms.

The delayed neutron activity of the samples (shown in Fig. 6.6(b)) has been acquired for 100s. It has been observed to follow an exponential decay profile as expected from the decay of precursors formed as a result of induced fission of ^{235}U. To estimate the delayed neutron fraction corresponding to different half-lives of respective precursors, the time profile of the DN activity has been fitted with a multi-exponential equation of the following type

$$C(t) = \nu_0 + \sum_{i=1}^{6} \nu_i e^{-\lambda_i t} \tag{6.3}$$

Here C is the DN counts at time t, λ_i's are the decay constants of different DN half-lives. As the data set of a single shot of PF device is insufficient to estimate seven (ν_i's) parameters using multi-exponential fit, we have summed the time-resolved delayed neutron activity of four shots to reduce the fitting error in the exponential parameters. As listed in Table 6.2, the delayed neutron fractions with corresponding half-lives estimated in this work are in good agreement with that reported in the literature[132]. The high error seen in the estimated

DN yield of long-lived half-lives and the slight difference in the DN fraction of one-half lives to their reported values could be due to the insufficient number of data points.

The half-life of the precursor with maximum DN yield (40%) is 2.2 s and the DN counts decrease with time (Fig. 6.6b). Considering this monotonous decrease in DN count and constancy of background with time, we have accumulated the activity only for 10s, up to which the delayed neutron count to background ratio remains high enough and ~71% of total delayed neutrons are registered in the detector during this time.

The Delayed neutron activity measured in all three samples is listed in Table 6.3. The maximum neutron activity has been observed in sample-1, i.e., in uranyl cake, whereas the same was lowest and within the background in sample-3, i.e., in contaminated civil debris. In sample 2, however, it is smaller than that in sample-1 and more than that in sample-3. Based on the measured activity of the two samples, i.e. sample-1 and sample-2, the DN counts per 10s per gram of ^{235}U averaged over various sample orientations and the interrogating source yield has been determined to be 24.14±5.6. The large value of relative error can be attributed to the inherent shot to shot variation [25] in the yield of the interrogating source and the non-uniform distribution of fissile material in the sample. As the interrogating source background is zero in the counting gate, the zero mass count rate is only due to the sample and cosmic background. This background is almost uniform with time, so we have used a conservative approach to estimate the limit of detection using the following expression:

$$D = B + 3\sigma \tag{6.4}$$

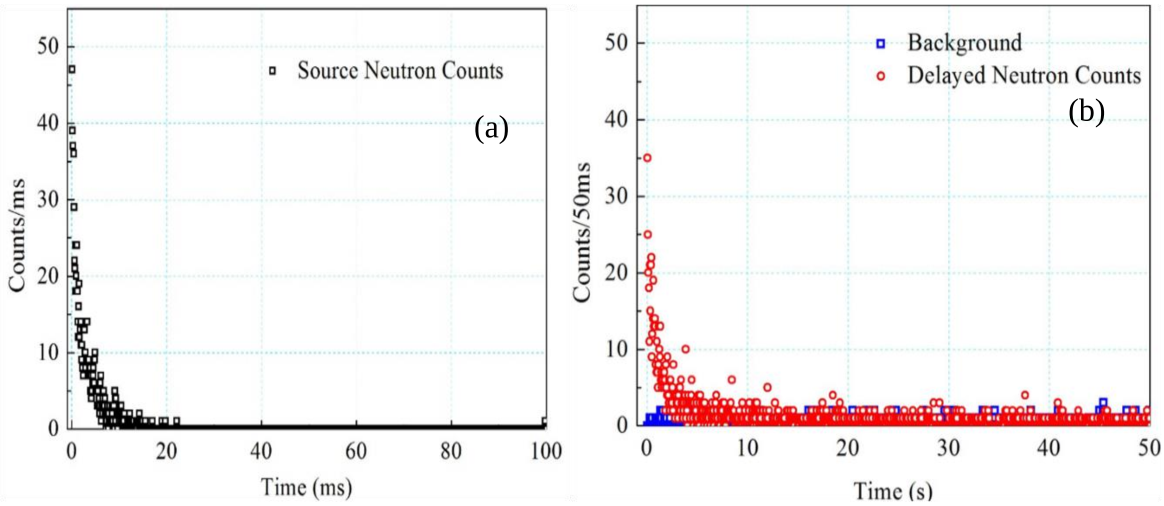

Fig. 6.6 The typical time profile of source and delayed neutron activity with PF neutron source. (a) The source neutron activity. (b) Delayed neutron activity observed in sample-1 (processed uranyl cake) with source yield of 3.5 $\times 10^8$ n per pulse.

Here B and σ are backgrounds and standard deviation in background activity, respectively. The detection limit of the system in a similar type of matrix for the PF device yield of $(2.1\pm0.8)\times10^8$ neutrons/shot is determined to be 170 g of natural uranium (~1.2g of ^{235}U) in ~40 kg of industrial waste.

Table 6.3Yield corresponding to six groups of delayed neutrons in the fission of ^{235}U

Half-Life (s)	DN yield (This work)	DN Yield (Keepin et. al.)
0.179	0.022±0.01	0.026±0.003
0.49	0.24±0.02	0.128±0.008
2.23	0.39±0.05	0.407±0.007
6.0	0.10±0.13	0.188±0.016
21.84	0.195±0.5	0.213±0.005
54.51	0.043±1	0.038±0.003

6.2.3 Comparison of simulations and experimental results

The delayed neutron counts estimated from simulations for all three samples along with experimental results are listed in Table-6.4. It may be noted that the simulated results have been obtained for the average plasma focus yield of 2.1×10^8n/shot with a normalization of 33%

enhanced yield due to axial anisotropy[109]. The simulated delayed neutron counts per 10s for sample-1 without considering axial anisotropy of PF device has been estimated to be 500±8.3, the inclusion of PF yield anisotropy of 33% results in 664±11delayed neutron counts. As in the simulations, we are estimating the number of n-p reactions per source neutrons in the detector volume due to induced fission of fissile material but in experiments, the counts are due to the charge collected as a result of energy deposited from n-p reactions. The electronic pulses produced due to the charge collection are further amplified and discriminated against the electronic noise as well as the pulses due to gamma background. Thus some neutron counts may be lost in the discriminator window, thereby lowering the counts in the experimental results. The counts lost in the discrimination window could have caused a difference between experimental and simulated results. The precision relative error in the simulation is ~1%.

Table 6.4Comparison of experimental and Simulation results (with D-D source neutron yield of 2.1×10^8 neutron per shot with axial yield normalization)

Samples	Fissile Content (g)	Delayed Neutron Counts/10s (Experimental)	Delayed Neutron Counts/10s (Simulations)
1	29.6 ±3.0	613±100	664±11
2	17.3 ±1.3	477±64	524±11
3	0.52±0.04	14±12	16±0.3

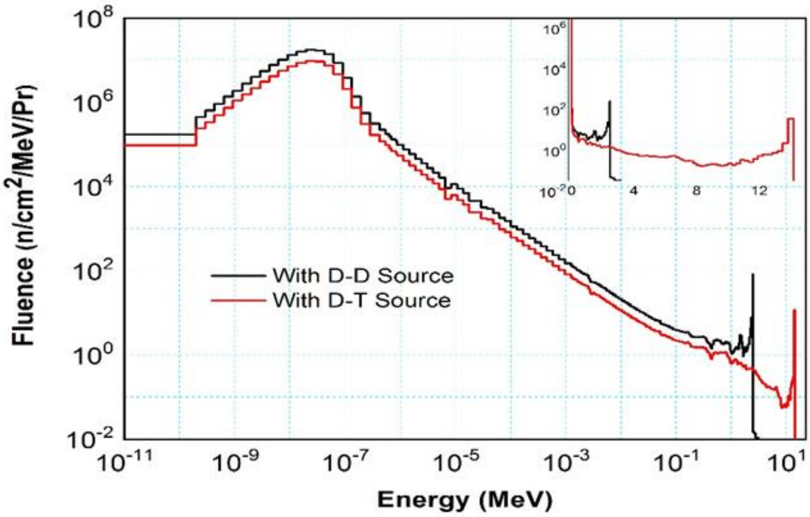

Fig. 6.7 Neutron fluence in sample-1 with D-D and D-T neutron source for geometry used in experiments. Inset: linear scale of energy depicting low energy fluence.

6.3 MC simulations for DT neutron source in the active assay of natural uranium

To assess the suitability and advantage of using a plasma focus device operated with D-T gas over a presently developed D-D operated device, Monte Carlo simulations have been carried out. It is observed (as shown in Fig.6.7) that the thermal neutron fluence in the sample is lower with the D-T source compared to that with the D-D neutron source. However, as noted in Table 6.1 and Table-6.4 the delayed neutron per interrogating neutron with D-T source is found to be more or less comparable to that for the D-D neutron source. To look into the induced fission of both the isotopes, *i.e.* ^{235}U and ^{238}U, for D-D and D-T sources, we have also carried out two sets of simulations considering 100% ^{235}U and 100% ^{238}U in sample-1 keeping other material compositions similar. The ratio of the fission for both the interrogating sources (D-D and D-T) is estimated to be:

$$\left(\frac{f_{235U(100\%)}}{f_{238U(100\%)}}\right)_{DD} = 52.9 \pm 2.4, \text{ and } \left(\frac{f_{235U(100\%)}}{f_{238U(100\%)}}\right)_{DT} = 15.4 \pm .4 \qquad (6.5)$$

It suggests that the fast fission of ^{238}U is not negligible when irradiated with a D-T source as there is substantial fast neutron fluence (Fig.6.7) which contributes to the fission of

^{238}U in addition to the fissile component (^{235}U). The higher contribution of fast neutron fission compensates the relatively less contribution from thermal neutrons for the D-T source as compared to that with the D-D source, thereby providing a comparable contribution for both the interrogating sources. With the D-D source, the ratio of fission ^{235}U/^{238}U in sample-1 (nat. U) is ~0.4 and with the D-T source, it is ~0.1. From Eq.6.5 it can also be inferred that even though the fission cross-section in ^{238}U is small, but due to higher fast fluence and low ^{235}U enrichment, the fission of^{238}U produces more delayed neutrons than that by ^{235}U.

Table 6.5Simulated delayed neutron counts (per source neutron) in three samples with D-T neutron source.

Sample	Number of fission reactions in sample per interrogating neutron (f)	Detection Efficiency for delayed neutrons counts/DN(ε_d)	Total DN (in 10 s) per interrogating neutron ($f\varepsilon_d \nu t_d$)	DN yield with same PF device
Sample-1	$(2.13\pm0.02)\times10^{-3}$	$(1.11\pm0.01)\times10^{-1}$	$(2.64\pm0.03)\times10^{-6}$	$(3.68\pm0.05)\times10^{4}$
Sample-2	$(1.73\pm0.02)\times10^{-3}$	$(9.80\pm0.01)\times10^{-2}$	$(1.92\pm0.04)\times10^{-6}$	$(2.67\pm0.06)\times10^{4}$
Sample-3	$(4.4\pm0.4)\times10^{-5}$	$(1.10\pm0.01)\times10^{-1}$	$(5.17\pm0.6)\times10^{-6}$	$(7.61\pm0.9)\times10^{2}$

The number of neutrons emitted as a result of the fusion is given by

$$N = \tau \int \frac{n^2}{4} < \sigma v > dV \qquad (6.5)$$

Here n is the number density of the gas in the plasma focus device, <σv> is the temperature dependant reaction rate for fusion and τ is the confinement time. For the range of plasma temperature generated in the PF device[85], the D-T fusion is nearly two orders more probable than the D-D fusion[133]. It suggests that by changing the gas of the PF device from D_2 to a mixture of D_2 and tritium, the yield can be enhanced up to two orders with the same device; however, the enhancement will depend upon the percentage of tritium in the DT mixture. This enhanced yield produces more fission in the sample; hence, a higher number of delayed neutrons can be produced using the same device. A nominal estimate of the delayed neutrons assuming ~50 times enhanced yield is provided in Table 6.5. Considering this DN activity with the same neutron background, the detection limit of the system operated with D-T gas is estimated to be 3.3 g of natural uranium. The delayed neutrons estimated in this case (D-T source) are as a result of induced fission of both the components ^{235}U and ^{238}U; hence the detection limit of natural uranium instead of ^{235}U has been quoted. The higher energy neutrons in the D-T source presents greater penetration length in the samples, so this scheme can be utilized for assay of natural uranium in industrial waste stored in commonly used drums of capacity ~200 L in the relevant facilities. As the sample is also used for moderating the neutrons, the elemental composition of the sample matrix also plays an important role in the assay, which needs to be taken into consideration. In the case of samples containing other than the industrial waste e.g. hydrogenous material, the matrix could moderate the interrogating as well as delayed neutrons up to a certain thickness then starts absorbing, which increases the minimum limit of detection for large sample volume.

Summary

This chapter presents the utilization of PF-based Z-pinch devices for fissile material characterization. We have carried out experiments for the assay of enriched as well as natural uranium in various sample matrices. A series of experiments have been carried out for the development of the characterization system for nuclear waste generated in the fuel fabrication facilities. The nuclear waste produced in the laboratories is of irregular geometries, which can’t be assayed using chemical techniques, this methodology provides a platform towards the management of nuclear waste of compressible or non-compressible type. The methodology developed for the quantification of fissile material in the natural uranium containing industrial nuclear waste provides insight for its deployment perspectives. The results of the simulations are found to be in good agreement with the experimental data. With the neutron source yield of 2.1×10^8per shot from the D-D operated plasma focus device, the detection limit of the system determined from the experiments is170g of natural uranium. It can be further improved by enhancing the interrogating neutron yield. Additional simulations infer that the detection limits will go further down to 3.3g of natural uranium upon using the same PF device with the D-T mixture.

CHAPTER 7

SUMMARY, CONCLUSIONS, AND FUTURE SCOPES

The present thesis reports on the development and characterization of two Z-pinch configurations (X-pinch and Plasma focus devices) for radiography of low-density plasma to thick objects. A study has been carried out on material characterization especially for fissile materials in various sample matrices using a PF-based Z-pinch device. During this thesis, we were able to provide answers or at least provide additional data on many problems posed at the onset of this report. A brief review of the work is as follows.

7.1 Development of an X-pinch for radiography of pulsed plasma

In the quest of the study of pulsed plasma, we have developed an X-pinch system on a slow current generator of current rate < 0.1kA/ns having a maximum peak current of 110 kA. In this system, we were able to estimate the minimum current required for pinching the plasma of the given mass in the range from 22 µg/cm to 134 µg/cm. The pinch current was found to increase with the linear mass density of the load. The x-ray properties of the X-pinches made of refractory and non-refractory metals have been studied in view of analytical formulations available in the literature. The pinch current is observed to linearly increase with the rate of rise of the current (dI/dt) of the driver. The effect of the coating in the non-refractory metal Cu has been studied for dI/dt from 0.06-0.11 kA/ns. Although Shelovenko et.al[73], in light of available experimental evidence[35, 134-137], have postulated in 2006 that a hot spot of extreme parameters (>1keV and <1µm size) in X-pinch can be achieved with a current rate of >1kA/ns. Employing a small capacitive current driver of <0.1 kA/ns (nearly one-tenth of that postulated by Shelovenko et.al), we have developed an X-pinch having x-ray parameters comparative to that postulated by Shelovenko et.al [73] for a higher current rate driver. The x-ray properties studied for the 2×13 μm W X-pinch in the dI/dt of 0.04kA/ns are the slowest among all reported drivers. A few micron thick dielectric coating is found to enhance the pinch current of a given load and subsequently seems to enhance the x-ray yield.

To examine its suitability for pulsed radiography applications, the source size, pulse width, timing, and jitter in various X-pinch loads have been investigated. The energy of the x-rays is found out to be in the soft energy regime i.e. <5keV, however in few configurations very small yield of >6keV has also been observed. The smallest source size has been observed to be <13 µm. It has also been observed that by varying the thickness and material of the wires, the x-ray pulses can be obtained at different instances ranging from 250 ns to 700 ns. An average time jitter in the X-pinches developed in the present system is observed to be ~20 ns, which is comparatively smaller than the reported slow current-driven X-pinches[74, 76]. The variability in the timing and low jitter of x-rays provides confidence to image the pinch plasma at a predetermined instance for a spatial profile.

Being a basic element of wire array, exploding wires are being studied on a wide range of current rates and magnitude. After the development and characterization of the X-pinches, we have carried out radiography of exploding wire plasma at different time instances. We have studied the exploding wires of Cu having diameters 43 μm and 60µm with a few micron thick coating on the current rate of 10kA -20kA per 1µs. The spatial profile of the exploding wire after the post-explosion phase at 270 ns to 770 ns has been studied. The wire core is observed to expand uniformly at a higher current rate (0.02kA/ns). At lower current rates the expansion in the wire throughout the length becomes non-uniform. In the case of the thicker wire at a slower current rate, the explosion was seen at a few points with the formation of unduloid which is due to the insufficient deposited energy to explode the whole wire. The average velocity of the expanding core is estimated to be 1.5 km/s in the wire explosion at the current rate of 0.02kA/ns and it is found to decrease with lowering the current rate.

7.2 Characterization of plasma focus for x-ray and neutron radiography

We have characterized a plasma focus device for its utilization in x-ray and neutron radiography of denser objects. The neutrons generated in the PF device are mono-energetic (2.45 MeV for DD fusion and 14.06 MeV for DT fusion) and pulsed, which has been utilized for characterization of samples containing low Z (hydrogenous) material by radiography. The neutron attenuation in these materials is maximum in the thermal energy range, so we have optimized the thickness of the commonly used moderators (perspex and polyethylene). Monte Carlo simulations show that the optimum thickness for moderating DD neutron is 80 mm and 100 mm, respectively, for polyethylene and perspex. This infers that polyethylene provides better moderation to neutron than perspex. The efficiency at the optimum moderator thickness is almost the same for both materials.

To utilize the 11.5 kJ PF device for radiography of various samples, the x-ray and neutron content in the image have been estimated using thick neutron and x-ray filters (Cd and Pb). In the radiographic image obtained on the image plate, the contribution of thermal neutrons is determined to be 4.2±2% and there is a significant contribution of x-rays in the lower energy region. The intensity of the x-rays has been observed to decrease with the increasing energy. In the x-ray spectrum of the PF device, the contribution of high energy (>100 keV) x-rays is observed to be very small (<2%). Moreover, the source size of the x-rays is <1 mm and the spatial resolution in the radiograph is estimated to be 147±10µm. Using the PF device, the x-ray and neutron radiographs of the different samples such as BNC’s, moving fans, hydride blisters in zircalloy samples, and the tungsten turbojet blade were obtained.

7.3 The methodology of calibration of detectors for fusion neutrons

In the yield measurement of Z-pinch-based fusion neutron sources, the detectors are often calibrated with the radio-isotopic and spontaneous fission neutron source. Due to differences in the energy spectrum (mono-energetic and continuous), this calibration methodology could result in a significant error in yield estimation. We have simulated the selection and thickness of suitable moderating material for both the mono-energetic (DD) and continuous energy sources (Pu-Be and ^{252}Cf). The optimum perspex moderator thickness for Pu-Be and D-D source is found to be 100 mm while the same for ^{232}Cf source is determined to 80 mm. However, in the case of polyethylene moderator, it is found to be 80 mm for Pu-Be and D-D source and 60mm for ^{252}Cf source. The ratio of absolute efficiency of the detector at optimum thickness is estimated to be 1:1.13±0.006:1.35±0.007 and 1:1.16±0.02:1.34±0.008 for perspex and polyethylene, respectively. It suggests that the thicknesses of moderators play a crucial role in the determination of fusion yield. Moreover, the moderator thickness optimized for a given detector and a given source need not necessarily work for another source if the energy spectrum of two sources differs significantly implying the necessity of a correction factor to be added to the calibration factor for yield measurement in such cases.

7.4 Fissile material characterization using PF based neutron source

We have utilized the plasma focus-based Z-pinch device for the characterization of fissile material in different sample matrices. A delayed neutron detection-based methodology has been developed for the assay of uranium in the small sample to large quantity compressible and non-compressible waste. A well-type detection system was designed for the assay of enriched uranium in compressible waste. The detection limit of this system is estimated to be ~40 mg of ^{235}U with an interrogating neutron source yield of $(2.4 \pm 1) \times 10^8$ n/pulse.

Furthermore, we have assessed the feasibility of active non-destructive assay of natural uranium in the industrial waste generally generated in the fuel fabrication facilities. The civil waste sample tested in the present study were in the form of sand, brick pieces, or chunks of debris. Monte Carlo simulations using an open-source code 'FLUKA' have also been carried out for the optimization of detector geometry around the samples. The results of the simulations are found to be in good agreement with the experimental data. With the neutron source yield of 2.1×10^8per per shot from the D-D operated plasma focus device, the detection limit of the system determined from the experiments to be 170g of natural uranium. Additional simulations infer that the detection limits will further go down to 3.3g of natural uranium upon using the same PF device with the D-T mixture.

7.5 Conclusion

In conclusion, it can be stated that the X-pinch-based Z-pinch system studied here, being a compact system developed on a slow current capacitive generator that could be an excellent device for diagnostics of exploding wire plasma generally studied in small laboratory scale systems. Owing to time variability and low jitter in the x-ray pulses as compared to previously reported systems, these X-pinches can be used for the study of different time-varying processes in pulsed plasmas. Our X-pinch experiments with different wire loads demonstrated the possibility of studying the Z-pinch dynamics in a very slow and small current device. For example, in 2 × 13 W X-pinch, a significant x-ray yield has been observed at a current level of 46 kA (in 1μs). Another interesting phenomenon observed is the effect of coating, the effect of type of metals i.e. refractory or non-refractory, on the yield and source size.

Furthermore, for the study of the internal structure of denser objects through radiography, the applicability of PF-based Z-pinches has been demonstrated. Employing PF devices, we have studied various aspects of neutron and x-ray radiography vis. a. vis. x-ray energy, x-ray and neutron content, optimization of moderators for efficient neutron imaging, etc. The pulsed character of neutrons has been utilized for the characterization of fissile material (uranium) in different sample matrices. The device has been employed the first time for the characterization of natural uranium in the construction and demolition waste of fuel fabrication facilities.

7.6 Future prospects

The results presented in this thesis are a small sampling of applications of numerous configurations of Z-pinches. Many scopes exist to expand the finding and improve our understanding of the physics of X-pinches driven by slow or fast current drivers. More data on X-pinches of different wire materials, wire number, and the enamelled coating are needed to be studied on drivers of the variable current rate. A study on time-dependent imaging of these X-pinches is also required to understand the dynamics of X-pinches. In addition to this, plasma parameters such as temperature, spectra, and density will be studied in the future to understand the physics of radiating plasma.

The pulsed character of the plasma focus device can be truly utilized in the radiographic study of ultrafast events such as measurement of symmetry in macro particle accelerator etc. In near future, a portable Z-pinch system will be employed for the study of projectile symmetry in rail guns. Material characterization application of PF device will be extended to the detection of contraband and study of isomeric states of the material of shorter (ms) half-lives.

It may also be noted that the Z-pinch devices studied here don’t belong to the mainstream of Z-pinches which are used for the energy driver of ICF. Nevertheless, in addition to applications discussed in this work, these two devices (X-pinch and PF device) can also provide insight to basic plasma and fusion research i.e. study of HEDP phenomena such as plasma implosion, hotspots, laboratory fusion, instabilities, and current distribution in plasmas.

REFERENCES

1. Ryutov, D., M.S. Derzon, and M.K. Matzen, The physics of fast Z pinches. Reviews of Modern Physics, 2000. **72**(1): p. 167.
2. Bennett, W.H., Magnetically self-focussing streams. Physical Review, 1934. **45**(12): p. 890.
3. Tonks, L., Theory and phenomena of high current densities in low pressure arcs. Transactions of the Electrochemical Society, 1937. **72**(1): p. 167.
4. Chace, W.G. and H.K. Moore, Exploding wires. Vol. 4. 2014: Springer.
5. Händel, S., B. Stenerhag, and I. Holmström, Hard X-rays from Exploding Wires. Nature, 1966. **209**(5029): p. 1227-1228.
6. Chace, W.G., A bibliography of the electrically exploded wire phenomenon. Vol. 58. 1958: Thermal Radiation Laboratory, Geophysics Research Directorate, Air Force ….
7. Lochte-Holtgreven, W., R. Schall, and F. Wecken, Production and measurement of high temperatures. Reports on Progress in Physics, 1958. **21**(1): p. 312.
8. Butt, E., et al., The design and performance of Zeta. Proceedings of the IEE-Part A: Power Engineering, 1959. **106**(2S): p. 12-29.
9. Rosenbluth, M.N. and C. Longmire, Stability of plasmas confined by magnetic fields. Annals of physics, 1957. **1**(2): p. 120-140.
10. Rosenbluth, M. and N. Rostoker, Theoretical structure of plasma equations. The Physics of Fluids, 1959. **2**(1): p. 23-30.
11. Adlam, J. and L. Holmes, An ultra-fast pinch experiment. Nuclear Fusion, 1963. **3**(2): p. 62.
12. Hammel, J. and D. Rode, Los Alamos Scientific Laboratory Report. LA-6203'MS, 1976.
13. Martin, T., et al. EBFA-Pulsed power for fusion. in 1979 3rd International Topical Conference on High-Power Electron and Ion Beam Research & Technology. 1979. IEEE.
14. Spielman, R., et al., Tungsten wire-array Z-pinch experiments at 200 TW and 2 MJ. Physics of Plasmas, 1998. **5**(5): p. 2105-2111.
15. Nash, T., et al., Comparison of a copper foil to a copper wire-array Z pinch at 18 MA. Physics of plasmas, 2004. **11**(10): p. L65-L68.
16. Giuliani, J.L. and R.J. Commisso, A Review of the Gas-Puff $ Z $-Pinch as an X-Ray and Neutron Source. IEEE Transactions on Plasma Science, 2015. **43**(8): p. 2385-2453.
17. Spielman, R., et al., Z-pinch implosions onto extremely low-density foam cylinders. Applied physics letters, 1985. **47**(3): p. 229-231.
18. Sanford, T., et al., Improved symmetry greatly increases X-ray power from wire-array Z-pinches. Physical review letters, 1996. **77**(25): p. 5063.
19. Liberman, M.A., et al., Physics of high-density Z-pinch plasmas. 2012: Springer Science & Business Media.

20. Niimi, G., et al., Development and characterization of a low current capillary discharge for X-ray laser studies. IEEE transactions on plasma science, 2002. **30**(2): p. 616-621.

21. Rocca, J., et al., Demonstration of a discharge pumped table-top soft-x-ray laser. Physical Review Letters, 1994. **73**(16): p. 2192.

22. Choi, P., et al., Experimental and theoretical investigation of the gas embedded Z-pinch. Nuclear fusion, 1988. **28**(10): p. 1771.

23. Giuliani, J.L. and R.J. Commisso, A Review of the Gas-Puff Z-Pinch as an X-Ray and Neutron Source. IEEE Transactions on Plasma Science, 2015. **43**(8): p. 2385-2453.

24. Coverdale, C., et al., Neutron production and implosion characteristics of a deuterium gas-puff Z pinch. Physics of plasmas, 2007. **14**(2): p. 022706.

25. Lebedev, S., et al., Coronal plasma behavior of the Z pinch produced from carbon and cryogenic deuterium fibers. Physics of Plasmas, 1998. **5**(9): p. 3366-3372.

26. Mosher, D., Interactions of relativistic electron beams with high atomic-number plasmas. The Physics of Fluids, 1975. **18**(7): p. 846-857.

27. Vikhrev, V. and V. Korolev, Neutron generation from Z-pinches. Plasma Physics Reports, 2007. **33**(5): p. 356-380.

28. Stephanakis, S., et al., Neutron production in exploding-wire discharges. Physical Review Letters, 1972. **29**(9): p. 568.

29. Young, F., S. Stephanakis, and D. Mosher, Neutron and energetic ion production in exploded polyethylene fibers. Journal of Applied Physics, 1977. **48**(9): p. 3642-3650.

30. Burdiak, G., et al., Cylindrical liner Z-pinch experiments for fusion research and high-energy-density physics. Journal of Plasma Physics, 2015. **81**(3).

31. Jones, M., et al., X-ray power and yield measurements at the refurbished Z machine. Review of Scientific Instruments, 2014. **85**(8): p. 083501.

32. Deeney, C., et al., Enhancement of X-ray power from a Z pinch using nested-wire arrays. Physical Review Letters, 1998. **81**(22): p. 4883.

33. Mesyats, G.A., et al., X-pinch source of subnanosecond soft X-ray pulses based on small-sized low-inductance current generator. Journal of Experimental and Theoretical Physics, 2010. **111**(3): p. 363-370.

34. Song, B.M., et al., X pinch X-ray radiation above 8 keV for application to high-resolution radiography of biological specimens. IEEE Transactions on Nuclear Science, 2004. **51**(5): p. 2514-2519.

35. Shelkovenko, T.A., et al., Point-projection x-ray radiography using an X pinch as the radiation source. Review of Scientific Instruments, 2001. **72**(1): p. 667-670.

36. Mittal, K., et al., Neutron production in dense x-pinch plasmas produced from deuterated polyethylene fibers. Journal of applied physics, 1991. **70**(11): p. 6712-6717.

37. Anan'ev, S., et al., X-pinch-based neutron source. Plasma physics reports, 2010. **36**(7): p. 601-608.

38. Mather, J.W., Dense plasma focus, in Methods in Experimental Physics. 1971, Elsevier. p. 187-249.

39. Filippov, N.V., et al., Filippov type plasma focus as intense source of hard X-rays (E/sub x//spl sime/50 keV). IEEE transactions on plasma Science, 1996. **24**(4): p. 1215-1223.

40. Lee, S. and A. Serban, Dimensions and lifetime of the plasma focus pinch. IEEE Transactions on Plasma Science, 1996. **24**(3): p. 1101-1105.

41. Ongena, J., et al., Magnetic-confinement fusion. Nature Physics, 2016. **12**(5): p. 398-410.

42. Taylor, T., Physics of advanced tokamaks. Plasma Physics and Controlled Fusion, 1997. **39**(12B): p. B47.

43. Haines, M., A review of the dense Z-pinch. Plasma Physics and Controlled Fusion, 2011. **53**(9): p. 093001.

44. Pereira, N., Whence Z-pinches? A personal view. 2020, China Academy of Engineering Physics.

45. Choi, P., et al., Temporal development of hard and soft x-ray emission from a gas-puff Z pinch. Review of Scientific Instruments, 1986. **57**(8): p. 2162-2164.

46. Bayley, J., et al., Observations of soft x-ray production in the speed 2 plasma focus. Journal of applied Physics, 1991. **69**(2): p. 613-617.

47. Chuvatin, A.S., et al., Heating of on-axis plasma heating for keV X-ray production with Z-pinches. IEEE transactions on plasma science, 2005. **33**(2): p. 739-751.

48. Shelkovenko, T., et al., Evolution of X-pinch loads for pulsed power generators with current from 50 to 5000 kA. Matter and Radiation at Extremes, 2018. **3**(6): p. 267-277.

49. Shelkovenko, T.A., et al., Hybrid X-pinch with conical electrodes. Physics of Plasmas, 2010. **17**(11): p. 112707.

50. Bolkhovitinov, E., et al. Study of Hybrid X-pinch in the XUV and SXR Spectral Ranges. in Journal of Physics: Conference Series. 2018.

51. Hammer, J.H., et al., High yield inertial confinement fusion target design for a z-pinch-driven hohlraum. Physics of Plasmas, 1999. **6**(5): p. 2129-2136.

52. Leeper, R., et al., Z pinch driven inertial confinement fusion target physics research at Sandia National Laboratories. Nuclear Fusion, 1999. **39**(9Y): p. 1283.

53. Klir, D., et al., Ion acceleration and neutron production in hybrid gas-puff z-pinches on the GIT-12 and HAWK generators. Matter and Radiation at Extremes, 2020. **5**(2): p. 026401.

54. Bennett, N., et al., Development of the dense plasma focus for short-pulse applications. Physics of Plasmas, 2017. **24**(1): p. 012702.

55. Kowalewicz, R., et al., Performance of the CERN plasma lens in laboratory and beam tests at the antiproton source. 1991, CM-P00059466.

56. Pompili, R., et al., Focusing of high-brightness electron beams with active-plasma lenses. Physical review letters, 2018. **121**(17): p. 174801.

57. Panofsky, W.K.H. and W.R. Baker, A focusing device for the external 350-MeV proton beam of the 184-inch cyclotron at Berkeley. Review of Scientific Instruments, 1950. **21**(5): p. 445-447.

58. Boggasch, E., et al., z-pinch plasma lens focusing of a heavy-ion beam. Physical review letters, 1991. **66**(13): p. 1705.

59. Antonov, O., et al., Generation of converging strong shock wave formed by microsecond timescale underwater electrical explosion of spherical wire array. Applied Physics Letters, 2013. **102**(12): p. 124104.

60. Olson, R., et al., Inertial confinement fusion ablator physics experiments on Saturn and Nova. Physics of Plasmas, 1997. **4**(5): p. 1818-1824.

61. Benage, J., W. Shanahan, and M. Murillo, Electrical resistivity measurements of hot dense aluminum. Physical review letters, 1999. **83**(15): p. 2953.

62. Branitskii, A., et al., Penetration of azimuthal magnetic flux to the interior of an unstable liner. Plasma Physics Reports, 1996. **22**(4): p. 277-287.

63. Lawson, J.D., Some criteria for a power producing thermonuclear reactor. Proceedings of the physical society. Section B, 1957. **70**(1): p. 6.

64. Lindl, J., Development of the indirect-drive approach to inertial confinement fusion and the target physics basis for ignition and gain. Physics of plasmas, 1995. **2**(11): p. 3933-4024.

65. Slutz, S., et al., Pulsed-power-driven cylindrical liner implosions of laser preheated fuel magnetized with an axial field. Physics of Plasmas, 2010. **17**(5): p. 056303.

66. Matzen, M.K., Z pinches as intense X-ray sources for inertial confinement fusion applications. Fusion engineering and design, 1999. **44**(1-4): p. 287-293.

67. Douglass, J.D. and D.A. Hammer, COBRA-STAR, a five frame point-projection X-ray imaging system for 1 MA scale wire-array Z pinches. Review of Scientific Instruments, 2008. **79**(3): p. 033503.

68. Jones, L., et al., A laser-initiated, gas-embedded Z pinch: Experiment and computation. Applied Physics Letters, 1981. **38**(7): p. 522-524.

69. Degnan, J., et al. Soft and ultrasoft X-Ray Measurements of Air Force Weapons Laboratory Shiva Imploding Plasma Liner. in AIP Conference Proceedings. 1981. American Institute of Physics.

70. Zakharov, S., V. Smirnov, and V.Y. Tsarfin, ANGARA-5 high intensity soft X ray source with imploding liner cascade for inertial confinement fusion, in Plasma physics and controlled nuclear fusion research 1992. V. 3. 1993.

71. Soto, L., et al., Evidence of nuclear fusion neutrons in an extremely small plasma focus device operating at 0.1 Joules. Physics of Plasmas, 2017. **24**(8): p. 082703.

72. Pikuz, S.A., T.A. Shelkovenko, and D.A. Hammer, X-pinch. Part I. Plasma physics reports, 2015. **41**(4): p. 291-342.

73. Shelkovenko, T.A., et al., Multiwire $ X $-pinches at 1-MA current on the COBRA pulsed-power generator. IEEE transactions on plasma science, 2006. **34**(5): p. 2336-2341.

74. Appartaim, R.K., X-rays from a microsecond X-pinch. Journal of Applied Physics, 2013. **114**(8): p. 083304.

75. Aranchuk, L.E., J. Larour, and A.S. Chuvatin, Experimental study of X-pinch in a submicrosecond regime. IEEE transactions on plasma science, 2005. **33**(2): p. 990-996.

76. Christou, C., A.E. Dangor, and D.A. Hammer, Characterization of wire x pinches driven by a microsecond-long capacitive discharge. Journal of Applied Physics, 2000. **87**(12): p. 8295-8303.

77. McBride, R.D., et al., A primer on pulsed power and linear transformer drivers for high energy density physics applications. IEEE transactions on plasma science, 2018. **46**(11): p. 3928-3967.

78. Pavez, C., et al., Energetics X-Ray Burst Observation in the Collapse of an X-Pinch Conducted in a Small Capacitive Generator of Low Impedance. IEEE Transactions on Plasma Science, 2018. **46**(11): p. 3829-3836.

79. Collins IV, G., et al., Study of X-pinch dynamics using a low current (25 kA) and slower current (400 ns) pulse. Physics of Plasmas, 2013. **20**(4): p. 042704.

80. Takasugi, K., S. Hakamatsuka, and V. Shlyaptseva, Formation of hot spots in the divergent gas-puff z pinch and its application to the observation of living tissue. 2018.

81. Knoblauch, P., et al., Hard X-ray dosimetry of a plasma focus suitable for industrial radiography. Radiation Physics and Chemistry, 2018. **145**: p. 39-42.

82. Niranjan, R., et al., Application of medium energy plasma focus device in study of radioisotopes. Physics Letters A, 2018. **382**(46): p. 3365-3368.

83. Andola, S., et al., Use of delayed gamma rays for active non-destructive assay of 235U irradiated by pulsed neutron source (plasma focus). Nuclear Instruments and Methods in Physics Research Section A: Accelerators, Spectrometers, Detectors and Associated Equipment, 2014. **753**: p. 138-142.

84. Tomar, B.S., et al., Non-destructive assay of fissile materials through active neutron interrogation technique using pulsed neutron (plasma focus) device. Nuclear Instruments and Methods in Physics Research Section A: Accelerators, Spectrometers, Detectors and Associated Equipment, 2013. **703**: p. 11-15.

85. Soto, L., New trends and future perspectives on plasma focus research. Plasma Physics and Controlled Fusion, 2005. **47**(5A): p. A361.

86. Wilson, P.D., The nuclear fuel cycle from ore to wastes. Oxford University Press: Oxford, 1996.

87. Reilly, D., et al., Passive nondestructive assay of nuclear materials. 1991, Nuclear Regulatory Commission.

88. Gozani, T., Active nondestructive assay of nuclear materials: principles and applications. 1981, Science Applications, Inc., Palo Alto, CA (USA); Monsanto Research Corp

89. Parker, J.L., The use of calibration standards and the correction for sample self-attenuation in gamma-ray nondestructive assay. 1986, Los Alamos National Lab., NM (USA).

90. Croft, S., et al., Analysis of calibration data for the uranium active neutron coincidence counting collar with attention to errors in the measured neutron coincidence rate.

Nuclear Instruments and Methods in Physics Research Section A: Accelerators, Spectrometers, Detectors and Associated Equipment, 2016. **811**: p. 70-75.

91. Ferrari, F. and P. Peerani, Performance of an active well coincidence counter for HEU samples. Radiation measurements, 2010. **45**(9): p. 1034-1043.

92. Lousteau, A.L., et al., Determining 235U enrichment in bulk uranium items using dual-energy interrogation with delayed neutron measurement. Nuclear Instruments and Methods in Physics Research Section A: Accelerators, Spectrometers, Detectors and Associated Equipment, 2018. **904**: p. 74-80.

93. Israelashvili, I., et al., Fissile mass estimation by pulsed neutron source interrogation. Nuclear Instruments and Methods in Physics Research Section A: Accelerators, Spectrometers, Detectors and Associated Equipment, 2015. **785**: p. 14-20.

94. Wigley, S., et al., Non-Destructive Analysis of Natural Uranium Pellet. Bulletin of the American Physical Society, 2017. **62**.

95. Ohzu, A., et al., Development of non-destructive Assay System using Fast Neutron direct interrogation method for actual uranium waste drums. Nippon Genshiryoku Gakkai Wabun Ronbunshi (Online), 2016. **15**(2): p. 115-127.

96. Bennett, F.D., Cylindrical shock waves from exploding wires. The Physics of Fluids, 1958. **1**(4): p. 347-352.

97. Chittenden, J.P., et al., Structural evolution and formation of high-pressure plasmas in x pinches. Physical review letters, 2007. **98**(2): p. 025003.

98. Chittenden, J.P., et al., One-, two-, and three-dimensional modeling of the different phases of wire array Z-pinch evolution. Physics of Plasmas, 2001. **8**(5): p. 2305-2314.

99. Romanova, V.M., et al., Electric explosion of fine wires: Three groups of materials. Plasma physics reports, 2015. **41**(8): p. 617-636.

100. Braginskii, S., On the behavior of a completely ionized plasma in a strong magnetic field. Zhur. Eksptl'. i Teoret. Fiz., 1957. **33**.

101. Pease, R., Equilibrium characteristics of a pinched gas discharge cooled by bremsstrahlung radiation. Proceedings of the Physical Society. Section B, 1957. **70**(1): p. 11.

102. Spitzer, L., Physics of fully ionized gases. 2006: Courier Corporation.

103. Roth, J.R., Introduction to fusion energy. 1986: Classworks.

104. Wiese, W., R. Huddlestone, and S. Leonard, Plasma Diagnostic Techniques. RH Hudldlestone, SL Leonard, editors, 1965. **21**: p. 201-264.

105. Idzorek, G.C. and R. Bartlett. Silicon photodiode characterization from 1 eV to 10 keV. in EUV, X-Ray, and Gamma-Ray Instrumentation for Astronomy VIII. 1997. International Society for Optics and Photonics.

106. Henke, B.L., E.M. Gullikson, and J.C. Davis, X-ray interactions: photoabsorption, scattering, transmission, and reflection at E= 50-30,000 eV, Z= 1-92. Atomic data and nuclear data tables, 1993. **54**(2): p. 181-342.

107. Rasband, W.S., ImageJ. 1997, Bethesda, MD.

108. Niranjan, R., et al., Preceedings of 25th National Symposium on plasma science and technology(PLASMA-2010), Guwahati, India, 2010.

109. Niranjan, R., et al., A 109 neutrons/pulse transportable pulsed DD neutron source based on flexible head plasma focus unit. Review of Scientific Instruments, 2016. **87**(3): p. 033504.

110. Boutoux, G., et al., Validation of modelled imaging plates sensitivity to 1-100 keV x-rays and spatial resolution characterisation for diagnostics for the "PETawatt Aquitaine Laser". Review of Scientific Instruments, 2016. **87**(4): p. 043108.

111. Ferrari, A., et al., FLUKA: a multi-particle transport code. 2005, Stanford Linear Accelerator Center (SLAC).

112. Everett, C.J. and E.D. Cashwell, A third Monte Carlo sampler. 1983: Los Alamos Report LA-9721-MS.

113. Everett, C. and E. Cashwell, A third Monte Carlo sampler. Los Alamos Report LA-9721-MS, 1983.

114. Cox, S.A., Delayed neutron data: review and evaluation. 1974, Argonne National Lab., Ill.(USA).

115. Sinars, D.B., et al., Bright spots in 1 MA X pinches as a function of wire number and material. Physics of Plasmas, 2008. **15**(9): p. 092703.

116. Cochran, F. and J. Davis, Evolution of an X-pinch plasma. Physics of Fluids B: Plasma Physics, 1990. **2**(6): p. 1238-1246.

117. Webb, F.H., et al., The electrical and optical properties of rapidly exploded wires, in Exploding wires. 1962, Springer. p. 37-75.

118. Batra, J., et al., Experimental investigations on specific energy deposition and burst characteristics in electrically exploded single copper wires. IEEE Transactions on Plasma Science, 2018. **47**(1): p. 596-602.

119. Jaar, G.S. and R.K. Appartaim, Axial plasma jet characterization on a microsecond x-pinch. Journal of Applied Physics, 2018. **123**(21): p. 213301.

120. Shelkovenko, T., et al., Electron-beam-generated x rays from X pinches. Physics of plasmas, 2005. **12**(3): p. 033102.

121. Shelkovenko, T., et al., Accelerated electrons and hard X-ray emission from X-pinches. Plasma physics reports, 2008. **34**(9): p. 754-770.

122. Pikuz, S.A., T.A. Shelkovenko, and D.A. Hammer, X-pinch. Part II. Plasma physics reports, 2015. **41**(6): p. 445-491.

123. Sarkisov, G., S. Rosenthal, and P. Sasorov. Physics of exploding wire in vacuum. in 2009 IEEE International Conference on Plasma Science-Abstracts. 2009. IEEE.

124. Axton, E.J., P. Cross, and J.C. Robertson, Calibration of the NPL standard Ra-Be photoneutron sources by an improved manganese sulphate bath technique. Journal of Nuclear Energy. Parts A/B. Reactor Science and Technology, 1965. **19**(6): p. 409-422.

125. Pereira, J., et al., The neutron long counter NERO for studies of Î²-delayed neutron emission in the r-process. Nuclear Instruments and Methods in Physics Research

Section A: Accelerators, Spectrometers, Detectors and Associated Equipment. **618**(1-3): p. 275-283.

126. East, L.V. and R.B. Walton, Polyethylene moderated 3He neutron detectors. Nuclear Instruments and Methods, 1969. **72**(2): p. 161-166.

127. Hamermesh, B., G.R. Ringo, and S. Wexler, The thermal neutron capture cross section of hydrogen. Physical Review, 1953. **90**(4): p. 603.

128. Zambra, M., et al., Experimental results on hard x-ray energy emitted by a low-energy plasma focus device: a radiographic image analysis. Plasma Physics and Controlled Fusion, 2009. **51**(12): p. 125003.

129. Verma, R., et al., Experimental study of neutron emission characteristics in a compact sub-kilojoule range miniature plasma focus device. Plasma Physics and Controlled Fusion, 2009. **51**(7): p. 075008.

130. Habibi, M., R. Amrollahi, and M. Attaran, Experimental study of current discharge behavior and hard X-ray anisotropy by APF plasma focus device. Journal of fusion energy, 2009. **28**(1): p. 130-134.

131. Rinard, P.M., Shuffler instruments for the nondestructive assay of fissile materials. 1991, Los Alamos National Lab.

132. Keepin, G.R., T.F. Wimett, and R.K. Zeigler, Delayed neutrons from fissionable isotopes of uranium, plutonium and thorium. Journal of Nuclear Energy (1954), 1957. **6**(1-2): p. IN2-21.

133. Zavyalov, N., et al., A source with a 10^13 DT neutron yield on the basis of a spherical plasma focus chamber. Plasma Physics Reports, 2013. **39**(3): p. 243-247.

134. Hammer, D.A., et al., X-pinch soft x-ray source for microlithography. Applied physics letters, 1990. **57**(20): p. 2083-2085.

135. Qi, N., et al., Characterization of X-pinch plasma. Review of Scientific Instruments, 1990. **61**(10): p. 2815-2815.

136. Pikuz, S.A., et al., Spatial, temporal, and spectral characteristics of an X pinch. Journal of Quantitative Spectroscopy and Radiative Transfer, 2001. **71**(2-6): p. 581-594.

137. Shelkovenko, T.A., et al., X pinch plasma development as a function of wire material and current pulse parameters. IEEE transactions on plasma science, 2002. **30**(2): p. 567-576.